

InAs/GaAs quantum-dot saturable absorber for a diode-pumped passively mode-locked Nd:YVO₄ laser at 1342 nm

K. W. Su, H. C. Lai, A. Li, Y. F. Chen, and K. F. Huang

Department of Electrophysics, National Chiao Tung University, Hsinchu, Taiwan

Received January 3, 2005

We report that InAs/GaAs quantum dots were developed to be saturable absorbers as well as output couplers in diode-pumped passively mode-locked Nd:YVO₄ lasers at 1342 nm. With an incident pump power of 12.6 W, an average output power of 0.85 W with a mode-locked pulse width of 26 ps at a repetition rate of 152 MHz was obtained. © 2005 Optical Society of America

OCIS codes: 140.4050, 140.3530, 140.3480.

Semiconductor saturable-absorber mirrors (SESAMs) have been identified as promising saturable absorbers for passively mode-locked all-solid-state lasers.^{1–4} In the past decade, most SESAMs were focused in the 0.8–1.06- μm spectrum region. Applications such as fiber sensing and intracavity Raman conversion to the 1.5- μm eye-safe spectrum region have enabled high-peak-power solid-state lasers at 1.3 μm to be practical light sources.^{5,6} Previously, the two main types of material for SESAMs at a 1.3- μm wavelength were InGaAs/GaAs and InGaAsP/InP quantum wells (QWs).^{7,8} InGaAs-based SESAMs for 1.3- μm lasers usually lead to significant residual nonsaturable losses because the required indium concentrations are beyond the critical strain-thickness limit. InGaAsP-based SESAMs could offer absorber layers with smaller lattice mismatches; however, they have inherent disadvantages such as low thermal conductivity and scarcity of suitable mirror materials.

Recently two new schemes based on the GaAs material system to reach a wavelength near 1.3 μm for applications of short-distance fiber-optic communication were proposed. One technique is the use of GaInNAs QWs with low nitrogen concentrations in an active region⁹; the other approach is the use of the InAs/GaAs quantum-dot (QD) multiple-layer structures.^{10,11} GaInNAs-based SESAMs have lately been applied to mode lock Nd-doped lasers at 1.3 μm .^{12,13} More recently, QD SESAMs have been successfully used as saturable absorbers in passively mode-locked Yb:KY(WO₄)₂ lasers at 1.03 μm .¹⁴ Even so, to our best knowledge, no experiments employing InAs/GaAs QDs to mode lock solid-state lasers near 1.3 μm have been reported. In this Letter we demonstrate a diode-pumped self-starting continuous-mode-locked Nd:YVO₄ 1.34- μm laser with an InAs/GaAs QD SESAM. With an incident pump power of 12.6 W, the mode-locked laser cavity produces an average output power of 0.85 W at 1.34 μm with a pulse width near 26 ps.

The QD SESAM structure, used as an output coupler in the mode-locked 1.34- μm laser, was grown upon an undoped GaAs substrate by metalorganic chemical-vapor deposition. The Bragg mirror struc-

ture was composed of 15 AlAs/GaAs quarter-wavelength layers. The reflectivity of the QD SESAM was 92%. The saturable-absorber part comprised three very thin (3–5-nm) InAs QD layers separated by GaAs half-wavelength layers. The growth temperature of the absorber structure was 500 °C.

Figure 1 depicts the measured results of the room-temperature photoluminescence (PL) spectrum for the QD SESAM. It can be seen that the PL peak wavelength is \sim 1340 nm with a FWHM of 45 nm. Unlike for the saturable absorber based on GaInNAs QWs, there is no need to anneal the QD SESAM to tune the PL wavelength. Postgrowth annealing is an essential process for a GaInNAs SESAM to reduce nonradiative defects and to tune the PL wavelength close to the lasing wavelength.^{15,16} Experimental results indicate that the present QD absorber has a saturation fluence of 20 $\mu\text{J}/\text{cm}^2$, a modulation depth of 3.0%, and nonsaturable losses of 2.0%.

Figure 2 shows the experimental configuration for the continuously mode-locked 1.34- μm Nd:YVO₄ laser with InAs/GaAs QDs used as a saturable absorber and an output coupler. The gain medium was a 0.3% Nd³⁺, 9-mm-long Nd:YVO₄ crystal. Both sides of the laser crystal were coated for antireflection at 1.34 μm ($R < 0.2\%$) with a wedge-cut angle of 0.5°. The pump source was a 16-W-808-nm fiber-coupled

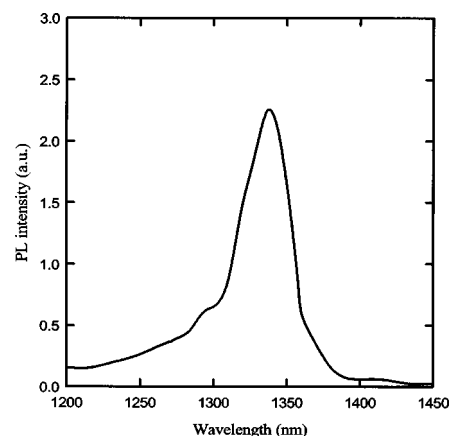


Fig. 1. Measured room-temperature PL spectrum of the InAs/GaAs QD SESAM.

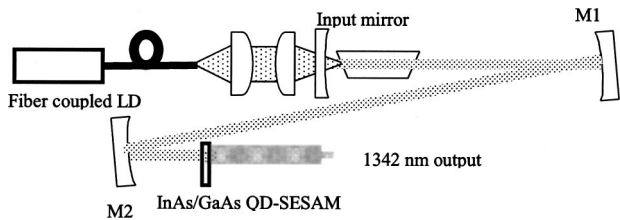


Fig. 2. Schematic of a diode-pumped self-starting continuous-mode-locked Nd:YVO₄ laser at 1342 nm. LD, laser diode.

laser diode with a core diameter of 800 μm and a numerical aperture of 0.2. Focusing lenses with 17.5-mm focal length and 85% coupling efficiency were used to reimage the pump beam into the laser crystal. The pump spot radius was $\sim 350 \mu\text{m}$. The resonator consisted of one input mirror; two high-reflection concave mirrors, M1 and M2, at lasing wavelength ($R > 99.8\%$); and one QD SESAM as an output coupler. The input mirror was a 500-mm radius-of-curvature concave mirror with an antireflection coating at a diode wavelength ($R < 0.2\%$) on the entrance face, a high-reflection coating at the lasing wavelength ($R > 99.8\%$), and a high-transmission coating at the diode wavelength ($T > 90\%$) on the other face. Note that the laser crystal was placed close to the input mirror for spatial overlap of the transverse mode structure and radial pump power distribution. The radii of curvature of mirrors M1 and M2 were 500 and 100 mm, respectively. M1 and M2 were separated by 600 mm; the overall cavity length was ~ 1000 mm. The laser mode radii were 345 μm inside the laser crystal and 42 μm on the QD SESAM. The QD SESAM was simply mounted upon a copper heat sink, but no active cooling was applied.

To provide the baseline for evaluating the mode-locking efficiency, we studied the cw performance of the present laser at 1342 nm first. For this investigation an output coupler with partial reflection at 1342 nm was used instead of the InAs QD SESAM. The optimum reflectivity of the output coupler was $\sim 94\%$. Figure 3 illustrates the average output power at 1342 nm with respect to the incident pump power in cw operation (circles) and in cw mode-locking operation (squares). In the cw regime the laser had a slope efficiency of 15%; the output power reached 1.31 W at an incident pump power of 12.6 W. With a QD SESAM as an output coupler, the laser self-started the cw mode-locking operation at pump powers greater than 3.95 W. In the cw mode-locking operation the laser, as shown in Fig. 3, had a slope efficiency of 9.8%; the output power reached 0.85 W at an incident pump power of 12.6 W.

The cw mode-locking pulse train was recorded by a LeCroy digital oscilloscope (Wavepro 7100; 10 G samples/s, 1 GHz bandwidth) with a fast p-i-n photodiode. Figure 4 shows a typical pulse train of the cw mode-locked laser. It can be seen that the pulse period of 6.6 ns is consistent with the round-trip time of the cavity length. The temporal duration of the mode-locked pulses was ~ 26 ps. The spectral properties of the laser were monitored by an optical

spectrum analyzer (Advantest Q8347) with a resolution of 0.005 nm. The spectral bandwidth (FWHM) was 0.101 nm. This result implied a time-bandwidth product of ~ 0.44 .

It is sensible to make a comparison between the present performance and the previous result for a GaInNAs QW as a saturable absorber.¹³ The present slope efficiency is lower than that for the GaInNAs QW absorber, which is 18%. We attribute the lower slope efficiency mainly to the nonoptimization of the output coupling of the QD SESAM and the nonsaturable losses. Optimizing the output coupler and reducing the nonsaturable losses is expected to improve the conversion efficiency considerably. Even so, the maximum output power of 0.85 W obtained here is higher than the previous result of 0.52 W. The present lasing bandwidth of 0.1 nm, however, is $\sim 25\%$ of the 0.39-nm bandwidth reported in Ref. 12. As a consequence, the pulse width of 26 ps is roughly four times the pulse width obtained in the research reported in Ref. 12. The narrower bandwidth might come from the additional etalon effects introduced by use of a QD SESAM as an output coupler. We suspect that the etalon effects can be effectively avoided by use of a high-quality antireflection coating ($R < 0.2\%$) on the back side of the GaAs wafer. Nevertheless, the use of a SESAM as an output coupler can make practical applications of laser systems easier and more compact.¹⁷

Finally, it is worthwhile to mention that the key issue for producing QD SESAM devices for 1.34- μm lasers consists in the uniformity of characteristics. We found that the PL peak wavelength varied significantly with the position of the wafer in the range 1250–1365 nm. So far, spatially resolved PL is critically important for producing QD SESAM devices for specific lasing wavelengths. A method for improving the uniformity is currently under investigation.

In conclusion, we have demonstrated a diode-pumped self-starting continuous-mode-locked Nd-doped 1.34- μm laser with an InAs/GaAs QD SESAM. With a QD SESAM as an output coupler, an average output power of 0.85 W was obtained at an incident pump power of 12.6 W. Stable pulses of ~ 26 -ps dura-

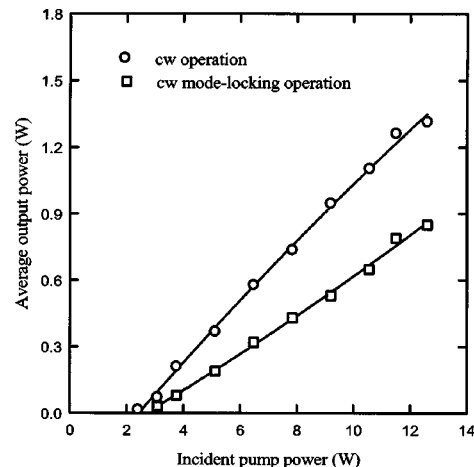


Fig. 3. Average output power at 1342 nm versus incident pump power in cw and mode-locking operation.

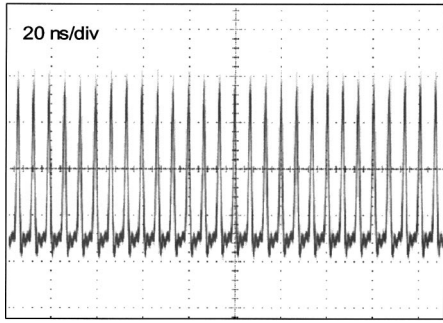


Fig. 4. Typical oscilloscope trace of a train of output pulses.

tion with a repetition rate of 152 MHz could be reached. The present result indicates that InAs/GaAs QD structures are appropriate saturable absorbers for mode-locking Nd-doped lasers at $1.34 \mu\text{m}$.

The authors gratefully acknowledge receipt of various InAs/GaAs QD structures from TrueLight Corporation. The authors also thank the National Science Council for its financial support of this research under contract NSC-93-2112-M-009-034. Y. F. Chen's e-mail address is yfchen@cc.nctu.edu.tw.

References

- O. Okhotnikov, A. Grudinin, and M. Pessa, *New J. Phys.* **6**, 177 (2004).
- U. Keller, D. A. B. Miller, G. D. Boyd, T. H. Chiu, J. F. Ferguson, and M. T. Asom, *Opt. Lett.* **17**, 505 (1992).
- G. J. Spühler, T. Südmeyer, R. Paschotta, M. Moser, K. J. Weingarten, and U. Keller, *Appl. Phys. B* **71**, 19 (2000).
- J. L. He, Y. X. Fan, J. Du, Y. G. Wang, S. Liu, H. T. Wang, L. H. Zhang, and Y. Hang, *Opt. Lett.* **29**, 2803 (2004).
- A. A. Kaminskii, K. Ueda, H. J. Eichler, Y. Kuwano, H. Kouta, S. N. Bagaev, T. H. Chyba, J. C. Barnes, G. M. A. Gad, T. Murai, and J. Lu, *Opt. Commun.* **194**, 201 (2001).
- Y. F. Chen, *Opt. Lett.* **29**, 2172 (2004).
- R. Fluck, B. Braun, E. Gini, H. Melchior, and U. Keller, *Opt. Lett.* **22**, 991 (1997).
- R. Fluck, G. Zhang, U. Keller, K. J. Weingarten, and M. Moser, *Opt. Lett.* **21**, 1378 (1996).
- M. Kondow, K. Uomi, A. Niwa, T. Kitatani, S. Watahiki, and Y. Yazawa, *Jpn. J. Appl. Phys. Part 1* **35**, 1273 (1996).
- D. L. Huffaker, G. Park, Z. Zou, O. B. Shchekin, and D. G. Deppe, *Appl. Phys. Lett.* **73**, 2564 (1998).
- A. R. Kovsh, N. A. Maleev, A. E. Zhukov, S. S. Mikhrin, A. P. Vasil'ev, Yu. M. Shernyakov, M. V. Maximov, D. A. Livshits, V. M. Ustinov, Zh. I. Alferov, N. N. Ledentsov, and D. Bimberg, *Electron. Lett.* **38**, 1104 (2002).
- H. D. Sun, G. J. Valentine, R. Macaluso, S. Calvez, D. Burns, M. D. Dawson, T. Jouhti, and M. Pessa, *Opt. Lett.* **27**, 2124 (2002).
- V. Liverini, S. Schön, R. Grange, M. Haiml, S. C. Zeller, and U. Keller, *Appl. Phys. Lett.* **84**, 4002 (2004).
- E. U. Rafailov, S. J. White, A. A. Lagatsky, A. Miller, W. Sibbett, D. A. Livshits, A. E. Zhukov, and V. M. Ustinov, *IEEE Photonics Technol. Lett.* **16**, 2439 (2004).
- A. Markus, A. Fiore, J. D. Ganière, U. Oesterle, J. X. Chen, B. Deveaud, M. Ilegems, and H. Riechert, *Appl. Phys. Lett.* **80**, 911 (2002).
- A. Passaseo, V. Tasco, M. De Giorgi, M. T. Todaro, M. De Vittorio, and R. Cingolani, *Appl. Phys. Lett.* **84**, 1868 (2004).
- X. Liu, L. Qian, F. Wise, Z. Zhang, T. Itatani, T. Sugaya, T. Nakagawa, and W. Torizuka, *Opt. Lett.* **15**, 129 (1998).

High-power efficient tunable Nd:GdVO₄ laser at 1083 nm

Y. F. Chen, M. L. Ku, and K. W. Su

Department of Electrophysics, National Chiao Tung University, Hsinchu, Taiwan

Received January 31, 2005

An efficient tunable diode-pumped Nd:GdVO₄ laser at 1083 nm has been constructed by suppressing the higher gain transition near 1063 nm. With 12.5 W diode pump power, the free-running output power centered about 1083 nm was up to 3.4 W, corresponding to an optical-to-optical conversion efficiency of 30.1%. When a simple uncoated etalon was used as a wavelength-selective element, the output power at each helium transition was higher than 2.5 W. © 2005 Optical Society of America

OCIS codes: 140.3600, 140.3530.

Laser optical pumping of helium is a critical process in helium magnetometers^{1,2} in a number of applications such as atomic cooling and trapping,³ and in fundamental atomic or nuclear studies.^{4,5} Two types of light source are often utilized for generating 1083 nm lasers: distributed-feedback and distributed Bragg reflector diode lasers,^{6,7} and solid-state lasers based on Nd:LaMgAl₁₁O₁₉ crystals⁸ or Nd:LuAlO₃ crystals.^{9,10}

Diode-pumped solid-state lasers have facilitated considerable advances in various fields of science and technology. Neodymium-doped gadolinium orthovanadate (Nd:GdVO₄) has proved to be an excellent gain medium because of its high pump absorption coefficient and large thermal conductivity.^{11–14} The output wavelengths of the research involving Nd:GdVO₄ crystals were mostly focused at 1063 nm.¹⁵ However, a spectroscopic study with crystal-field analysis¹⁶ has revealed that there are five or six emission bands within the ⁴F_{3/2} → ⁴I_{11/2} transition of a Nd:GdVO₄ crystal. Figure 1 displays the room-temperature fluorescence spectrum for the ⁴F_{3/2} → ⁴I_{11/2} transition of a Nd:GdVO₄ crystal with a spectral resolution of 0.1 nm. It can be seen that one of the Stark components has a central emission wavelength at 1083 nm. As a consequence, the Nd:GdVO₄ crystal could be a favorable candidate for a 1083 nm laser. To the best of our knowledge, there have been no studies of the performance of Nd:GdVO₄ lasers at 1083 nm.

In this Letter, a compact high-power all-solid-state laser at 1083 nm with a Nd:GdVO₄ crystal is demonstrated. With an output coupler of *T*=2.7%, the compact cavity produces the maximum output power of 3.4 W at an incident pump power of 12.5 W. With a simple uncoated etalon in the laser cavity, a tuning range of nearly 1.3 nm was achieved, and the output power at the 2³S₁ → 2³P_{*J*} (*J*=0, 1, 2) transitions of atomic helium was generally higher than 2.5 W. The experimental results indicate that a diode-pumped Nd:GdVO₄ laser is a superior light source for helium optical pumping.

Figure 2 is a schematic of the Nd:GdVO₄ laser on the 1083 nm line. Since the stimulated-emission cross section for the 1083 nm transition is approximately five to six times smaller than that for the 1063 nm line, operation of the Nd:GdVO₄ laser at

1083 nm requires suppression of the competing transition channel at 1063 nm. Here the stronger transition near 1.06 μm was suppressed by use of specifically coated mirrors. The laser active medium was a 10 mm length of GdVO₄ crystal doped with 0.27 at. % Nd. A Nd:GdVO₄ crystal with a low dopant concentration was used to prevent thermally induced fracture.¹⁷ The laser crystal was wrapped with indium foil and mounted in a water-cooled copper block. The water temperature was maintained at 25 °C. Both sides of the laser crystal were coated for antireflection, one at 808 and one at 1083 nm (*R* < 0.2%). The pump source was a 16 W 808 nm fiber-coupled laser diode with a core diameter of 800 μm and a numerical aperture of 0.16. A focusing lens with a 12.5 mm focal length and 85% coupling efficiency was used to reimaged the pump beam into the laser crystal. The pump spot radius was ~250 μm. The cavity length was approximately 35 mm. The input mirror was a 500 mm radius-of-curvature concave mirror with antireflection coating at the pump wavelength (~808 nm) on the entrance face (*R* < 0.2%), high-reflection coating at 1083 nm (*R* > 99.5%), and high-transmission coating at 808 nm (*T* > 90%) and 1063 nm (*T* > 80%) on the other surface. We used several output couplers with different reflectivities at 1083 nm in the experiment to study the output performance. Note that coatings were also

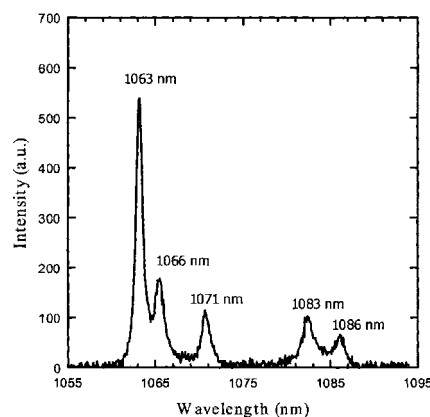


Fig. 1. Room-temperature fluorescence spectrum for the ⁴F_{3/2} → ⁴I_{11/2} transition of a Nd:GdVO₄ crystal.

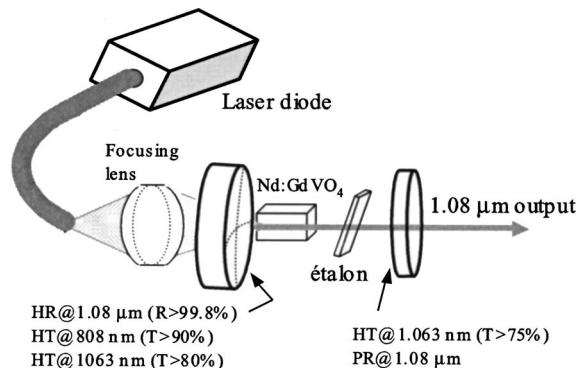


Fig. 2. Experimental configuration for the diode-pumped Nd:GdVO₄ laser at 1083 nm: HR, highly reflective; HT, highly transmissive; PR; partially reflective.

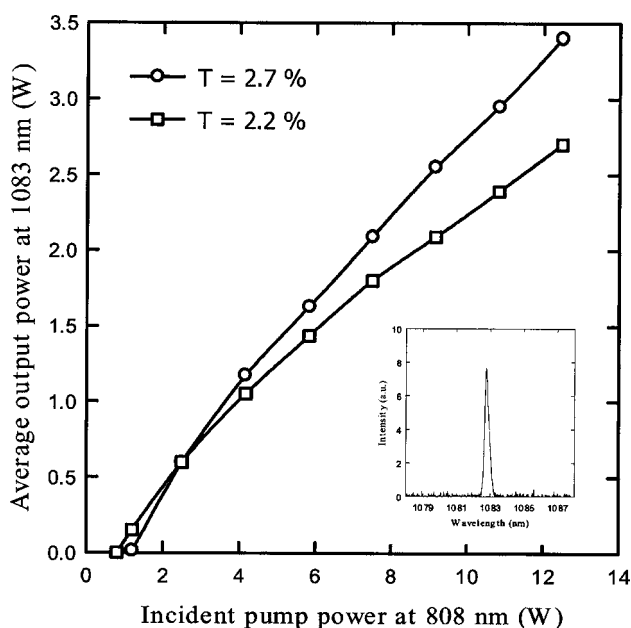


Fig. 3. Free-running output power at 1083 nm without the frequency-selective element in the cavity as a function of incident pump power for two couplers, with $T=2.7\%$ and $T=2.2\%$. The optical spectrum is shown in the inset.

needed on the output couplers for high loss at 1063 nm; otherwise emission at 1063 nm could occasionally occur. An uncoated etalon of thickness 0.25 mm was used for the investigation of tuning characteristics. The optical spectrum of the laser was monitored by an optical spectrum analyzer (Advantest Q8347). The spectrum analyzer described in this Letter employs a Michelson interferometer with a Fourier spectrum system to reach a resolution of 0.004 nm. Since the longitudinal-mode spacing is approximately 0.02 nm, the longitudinal-mode spectral information can be clearly resolved.

Figure 3 shows the experimental results for the output power at 1083 nm without the frequency-selective element in the cavity as a function of the incident pump power for two couplers, with $T=2.7\%$ and $T=2.2\%$. The free-running linewidth of the Nd:GdVO₄ laser was measured to be ~ 0.4 nm

FWHM and centered at 1082.7 nm, as shown in the inset of Fig. 3. When the output coupler with 2.2% transmission was used, the maximum output power was approximately 2.7 W, with a slope efficiency of 24%. The maximum output power of 3.4 W was obtained with the 2.7% output coupler at an incident pump power of 12.5 W, corresponding to a slope efficiency of 30% and a threshold power of 1.2 W. Beam quality factor M^2 was less than 1.5 for all pump powers. Using the experimental slope efficiency and the Findlay-Clay method,¹⁸ we estimated the round-trip cavity excess losses to be 0.45%. With standard cavity mirrors coated for 1063 nm, the slope efficiency for 1063 nm was in the range from 50% to 60%. Making a comparison between the slope efficiencies of 1063 and 1083 nm, we estimated the quantum efficiency for 1083 nm to be approximately half of that for 1063 nm. Even so, the output power is considerably higher than the previous result obtained with other Nd-doped laser crystals.⁸⁻¹⁰

With a simple uncoated etalon in the laser cavity, the spectral output of the laser was generally less than 0.05 nm. Furthermore, the laser can easily be tuned from 1082.3 to 1083.6 nm, as shown in Fig. 4. The 1.3 nm tuning range centered about 1083 nm covers the entire wavelength region containing the ⁴He transitions at wavelengths 1082.908 (D_0), 1083.025 (D_1), and 1083.034 nm (D_2). With a pump power of 12.5 W, the output power at each helium transition was higher than 2.5 W.

It is worthwhile to mention that the laser cavity can generate simultaneous laser action at wavelengths 1083 and 1086 nm. The spontaneous emission strength for the 1086 nm transition is only 1.5 times smaller than that for the 1083 nm line, as shown in Fig. 1. Therefore dual-wavelength operation could be achieved with an output coupler to balance the gains for 1083 and 1086 nm. Figure 5 shows the free-running output power at a dual-wavelength operation as a function of the incident pump power for an output coupler with $T=8.1\%$ at 1083 nm and $T=5.3\%$ at 1086 nm. It can be seen that the relative output powers at 1083 and 1086 nm were dependent

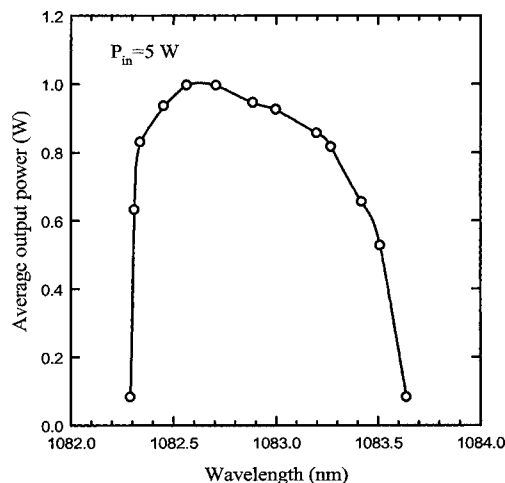


Fig. 4. Tuning curve of the Nd:GdVO₄ laser with an uncoated, 0.25 mm thick etalon.

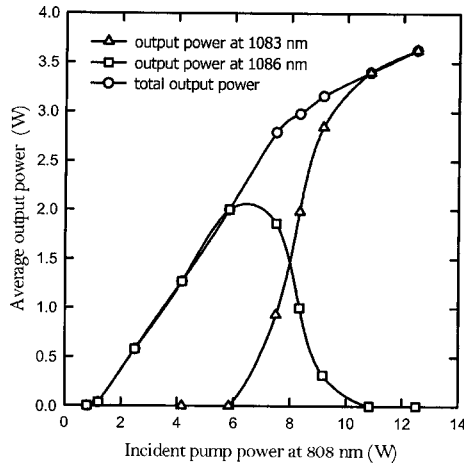


Fig. 5. Free-running output power at $1.08 \mu\text{m}$ as a function of the incident pump power for an output coupler with $T=8.1\%$ at 1083 nm and $T=5.3\%$ at 1086 nm.

on the pump power. As the pump power increased, the output power was initially dominated at 1086 nm, whereas, from a certain value of pump power, the output power at 1083 nm was started and the lasing power at 1086 nm began to decrease until the output power was completely dominated at 1083 nm. The power decrease of 1086 nm light above 6 W of pump power comes mainly from the gain competition between 1083 and 1086 nm light. Nevertheless, dual-wavelength operation could be obtained with the pump powers in the range from 6 to 10 W.


In summary, an efficient compact diode-pumped Nd:GdVO₄ laser at 1083 nm has been demonstrated. With 12.5 W pump power, 3.4 W of 1083 nm average output power was obtained, corresponding to an optical-to-optical conversion efficiency of 30.1%. Employing an uncoated etalon in the laser cavity, we could tune the laser from 1082.3 to 1083.6 nm, and more than 2.5 W of power at the $2^3S_1 \rightarrow 2^3P_J$ ($J=0, 1, 2$) transitions of atomic helium was achieved. We believe the Nd:GdVO₄ laser at 1083 nm

to be a useful alternative to previous light sources for helium optical pumping.

Y. F. Chen's e-mail address is yfchen@cc.nctu.edu.tw.

References

1. R. E. Slocum, L. D. Scheerer, P. Tin, and R. Marquedant, *J. Appl. Phys.* **64**, 6615 (1988).
2. C. L. Bohler, *J. Appl. Phys.* **66**, 4614 (1989).
3. A. Aspect, E. Arimondo, R. Kaiser, N. Vansteenkiste, and C. Cohen-Tannoudju, *Phys. Rev. Lett.* **61**, 826 (1988).
4. P. Zhao, J. R. Lawall, and F. M. Pipkin, *Phys. Rev. Lett.* **66**, 592 (1991).
5. P. Mueller, L. B. Wang, R. J. Holt, Z. T. Lu, T. P. O'Connor, and J. P. Schiffer, *Phys. Rev. Lett.* **92**, 022501 (2004).
6. C. L. Bohler and B. I. Marton, *Opt. Lett.* **19**, 1346 (1994).
7. M. Prevedelli, P. Cancio, G. Giusfredi, F. S. Pavone, and M. Inguscio, *Opt. Commun.* **125**, 231 (1996).
8. L. D. Scheerer and P. Tin, *J. Appl. Phys.* **68**, 943 (1990).
9. E. F. Stephens, R. Vandiver, P. Tin, and M. R. Kokta, *J. Appl. Phys.* **78**, 3543 (1995).
10. H. A. Abu Safia, *Opt. Commun.* **139**, 212 (1997).
11. A. I. Zagumennyi, V. G. Ostroumov, I. A. Shcherbarkov, T. Jensen, J. P. Meyn, and G. Huber, *Sov. J. Quantum Electron.* **22**, 1071 (1992).
12. T. Jensen, V. G. Ostroumov, J. P. Meyn, G. Huber, A. I. Zagumennyi, and I. A. Shcherbarkov, *Appl. Phys. B* **58**, 373 (1994).
13. T. Ogawa, Y. Urata, S. Wada, K. Onodera, H. Machida, H. Sagae, M. Higuchi, and K. Kodaira, *Opt. Lett.* **28**, 2333 (2003).
14. V. Lupei, N. Pavel, Y. Sato, and T. Taira, *Opt. Lett.* **28**, 2366 (2003).
15. Chr. P. Wyss, W. Luthy, H. P. Weber, V. I. Vlasov, Y. D. Zavartsev, P. A. Studenikin, A. I. Zagumennyi, and I. A. Shcherbakov, *Appl. Phys. B* **68**, 659 (1999).
16. F. G. Anderson, P. L. Summers, H. Weidner, P. Hong, and R. E. Peale, *Phys. Rev. B* **50**, 14802 (1994).
17. Y. F. Chen, *IEEE J. Quantum Electron.* **35**, 234 (1999).
18. D. Findlay and R. A. Clay, *Phys. Lett.* **20**, 277 (1966).

Y.F. CHEN 
Y.S. CHEN
T.H. OU
K.W. SU

Compact efficient diode-pumped Nd:YVO₄ Q-switched blue laser with intracavity frequency tripling

Department of Electrophysics, National Chiao Tung University, Hsinchu, Taiwan

Received: 1 February 2005 / Revised version: 14 April 2005
Published online: 28 June 2005 • © Springer-Verlag 2005

ABSTRACT We demonstrate a compact efficient diode-pumped acousto-optically Q-switched intracavity-frequency-tripled Nd:YVO₄ blue laser. The optimum polarization state is experimentally investigated to optimize the output performance. Greater than 280 mW of 447-nm average power at a repetition rate of 25 kHz was generated with a 15-W diode pump power. At 25 kHz, the pulse width is shorter than 15 ns and the peak power is higher than 800 W.

PACS 42.60.Gd; 42.65.Ky; 42.55.Rz

Efficient, compact, high-peak-power, and high-repetition-rate (> 20 kHz) visible-wavelength lasers are of practical importance for many applications such as environmental analysis, spectroscopy and undersea imaging. Diode-pumped solid-state lasers have been shown to be efficient, compact, and reliable all-solid-state optical sources. Frequency doubling of Nd-doped lasers operating at the $4F_{3/2}-4I_{9/2}$ transition has been extensively explored during the past few years for producing coherent blue light [1–5]. Another approach for blue laser sources is based on frequency tripling of a Nd-doped laser operating at the $4F_{3/2}-4I_{13/2}$ transition [6–10]. Unlike the three-level system of the $4F_{3/2}-4I_{9/2}$ transition, stimulated emission at the $4F_{3/2}-4I_{13/2}$ transition is a four-level system that can provide a low-threshold and stable laser output due to the lack of sensitive temperature dependence of the transition rate. Up to now, most of the research results involving blue-light generation were focused on the aspects of extracavity third-harmonic generation (THG); the average output power for a blue laser was approximately several tens of milliwatts and the peak power was only up to several tens of watts.

In this work, we demonstrate a compact blue laser by using intracavity THG at 1342 nm in a diode-pumped Q-switched Nd:YVO₄ laser. Efficient THG for yielding blue light is achieved by cascading second-harmonic generation (SHG) in a KTP crystal and sum-frequency generation (SFG) in a LBO crystal. At an incident pump power of 15 W, the compact laser cavity, operating at 25 kHz, produces average output powers at 447 nm up to 282 mW and a peak power greater than 800 W.

The experimental configuration for the diode-pumped actively Q-switched blue laser at 447 nm is depicted in Fig. 1. The cavity mirrors have a special dichroic coating for efficient intracavity THG. The input mirror is a 500-mm radius-of-curvature concave mirror with antireflection coating at the pump wavelength (~ 808 nm) on the entrance face ($R < 0.2\%$), high-reflection coating at 1342 nm, 671 nm, and 447 nm ($R > 99.8\%$) and high-transmission coating at the pump wavelength on the other surface ($T > 95\%$). The output coupler has high-reflection coating at 1342 nm and 671 nm ($R > 99.8\%$) and high-transmission coating at 447 nm ($T > 85\%$). Both mirrors have a transmission of 90% at 1064 nm to suppress parasitic oscillations on lines in the 1064-nm region.

The pump source was an 808-nm fiber-coupled laser diode with a core diameter of 800 μm , a numerical aperture of 0.16, and a maximum output power of 16 W. A focusing lens with 12.5-mm focal length and 90% coupling efficiency was used to re-image the pump beam into the laser crystal. The focus radius of the pump beam was around 300 μm . The laser-active medium was a 0.25 at.% Nd:YVO₄ crystal with a length of 9 mm. A Nd:YVO₄ crystal with a low dopant concentration was used to avoid thermally induced fracture [11]. The laser crystal was placed very near (2–3 mm) to the input mirror. The nonlinear crystal for efficient SHG was a 10-mm-long KTP crystal cut for type-II phase matching at 1342 nm. On the other hand, a sum-frequency mixer for THG was an 8-mm-long LBO crystal cut for type-I phase matching. Both sides of all crystals were coated for antireflection at 1342 nm

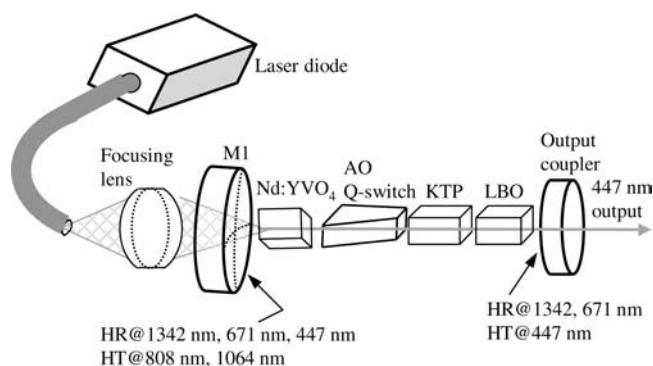


FIGURE 1 Experimental setup for the diode-pumped Q-switched intracavity frequency-tripled blue laser

and 671 nm ($R < 0.2\%$). The gain medium and nonlinear crystals were wrapped with indium foils and mounted in water-cooled copper blocks. The water temperature was maintained at 25°C . The 20-mm-long acousto-optical Q-switcher (Gooch and Housego) had antireflection coatings at 1342 nm on both faces and was driven at a 40.68-MHz center frequency with 3.0-W of radio-frequency power. The overall laser-cavity length was 65 mm. The spectral information of the laser was monitored by an optical spectrum analyzer (Advantest Q8381A). The spectrum analyzer employing a grating monochromator can be used for high-speed measurement of pulse light with the resolution of 0.1 nm. The pulse temporal behavior was recorded by a LeCroy digital oscilloscope with a fast PIN photodiode.

Since the efficient SHG is of the essence for blue-light generation in SFG, we first investigate the SHG performance in the KTP crystal. For this investigation, only KTP crystal was put into the cavity for the SHG process without LBO crystal. In addition, an output coupler with high-reflection coating at 1342 nm ($R > 99.8\%$) and high-transmission coating at 671 nm ($T > 85\%$) was used instead of the above-mentioned output coupler for THG. For single-pass external type-II SHG, $\varphi = 45^\circ$ can lead to the most effective conversion efficiency, where φ is the angle between the extraordinary axis (E axis) of the KTP crystal and the c axis of the Nd:YVO₄ crystal. Note that the angle φ also represents the angle between the polarization of the pump fundamental wave and the polarization of the generated second-harmonic wave. In the intracavity type-II SHG, however, the optimum φ is usually not equal to 45° because the fundamental wave becomes an elliptically polarized wave due to the birefringent effect of the KTP crystal. Based on the experimental results, the optimum φ is found to be approximately 35° . The influence of the polarization effects on the efficiency of intracavity SHG can be analyzed from the theoretical model [12]. The SHG conversion efficiency at $\varphi = 35^\circ$, on the whole, is approximately ten percent higher than that at $\varphi = 45^\circ$. Figure 2 shows the average output power at 671 nm as a function of the incident pump power at a repetition rate of 25 kHz for $\varphi = 35^\circ$. It can be seen that the maximum red output power of 1.08 W was obtained at an incident pump power of 15 W, corresponding to a conversion efficiency of 7.2%. It is worthwhile to mention that the highest average output power at 1342 nm that could be extracted with a proper output coupler ($\sim 94\%$ reflectivity at 1342 nm) was about 2.4 W. Accordingly, the maximum second-harmonic power is close to 45% of the available Q-switched fundamental power. Since the following THG is accomplished via a type-I SFM, a smaller φ essentially produces higher conversion efficiency for blue output at 447 nm. Therefore, the configuration with $\varphi = 35^\circ$ is employed for the subsequent intracavity THG experiment.

Since the polarization of the fundamental wave is not parallel to the polarization of the second-harmonic wave, the THG conversion efficiency from type-I SFM strongly depends on the parameter ϑ , where ϑ is the angle between the ordinary axis (O axis) of the LBO crystal and the E axis of the KTP crystal. In general, efficient THG from type-I SFM comes from the power intensities of the fundamental and second-harmonic beams in a ratio of 1:1. In the present configuration, however, the power intensity of the second-harmonic wave is

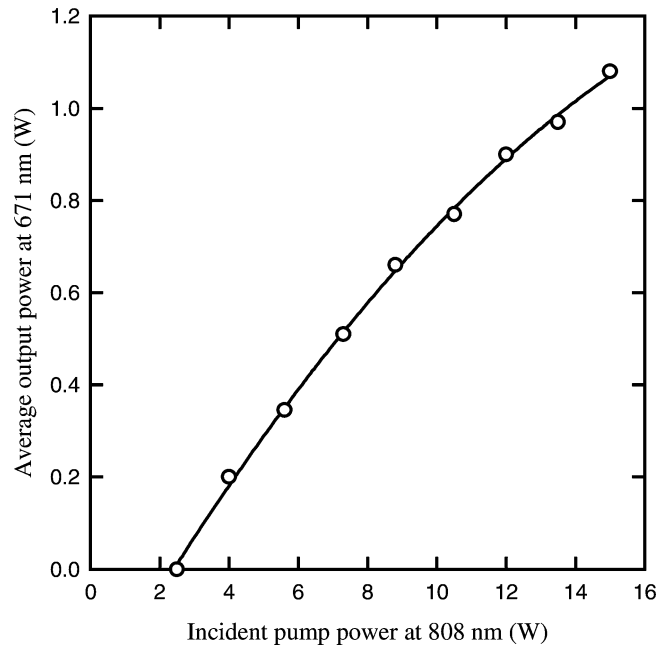


FIGURE 2 The average output power at 671 nm as a function of the incident pump power at a repetition rate of 25 kHz for $\varphi = 35^\circ$, where φ is the angle between the E axis of the KTP crystal and the c axis of the Nd:YVO₄ crystal

found to be approximately 1.4 times less than that of the fundamental wave. Therefore, the difference of the power intensities between the fundamental and second-harmonic waves for effective SFM can be minimized by setting the O axis of the LBO crystal to be parallel to the polarization of the second harmonic, i.e. $\vartheta = 0^\circ$. Figure 3 depicts the average output power at 447 nm as a function of the incident pump power at a repetition rate of 25 kHz for $\vartheta = 0^\circ$, 15° , and 30° . As

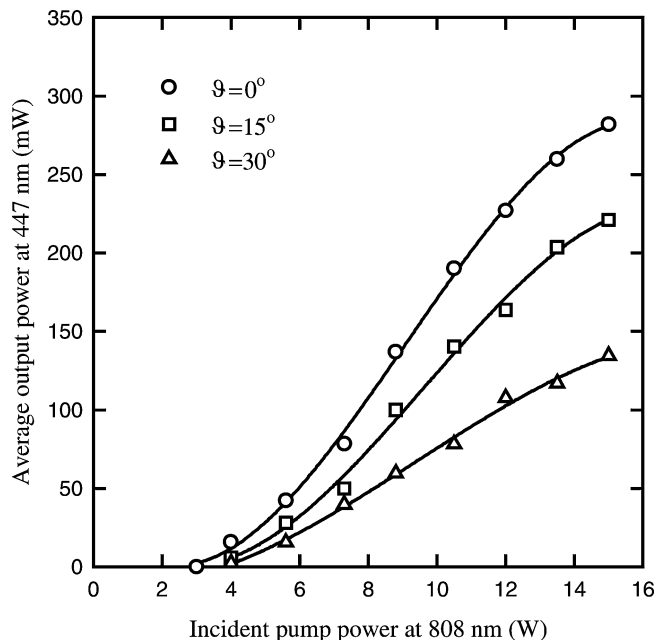


FIGURE 3 The average output power at 447 nm as a function of the incident pump power at a repetition rate of 25 kHz for $\vartheta = 0^\circ$, 15° , and 30° , where ϑ is the angle between the O axis of the LBO crystal and the E axis of the KTP crystal

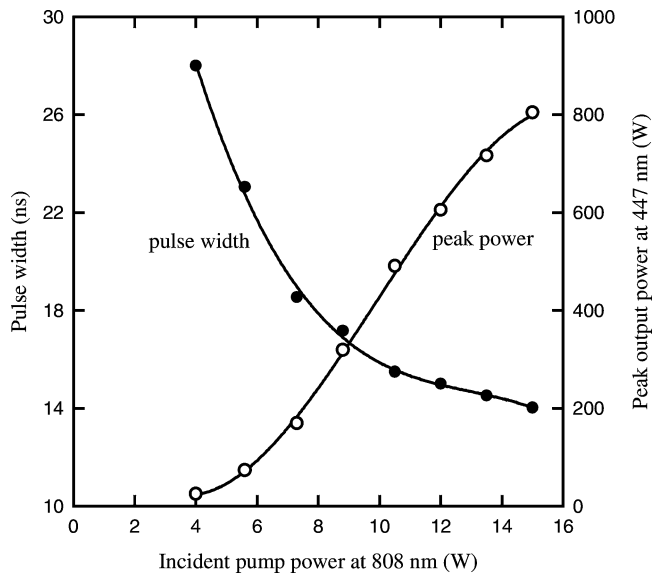


FIGURE 4 The peak blue power and pulse width versus diode pump power at a repetition rate of 25 kHz and $\vartheta = 0^\circ$

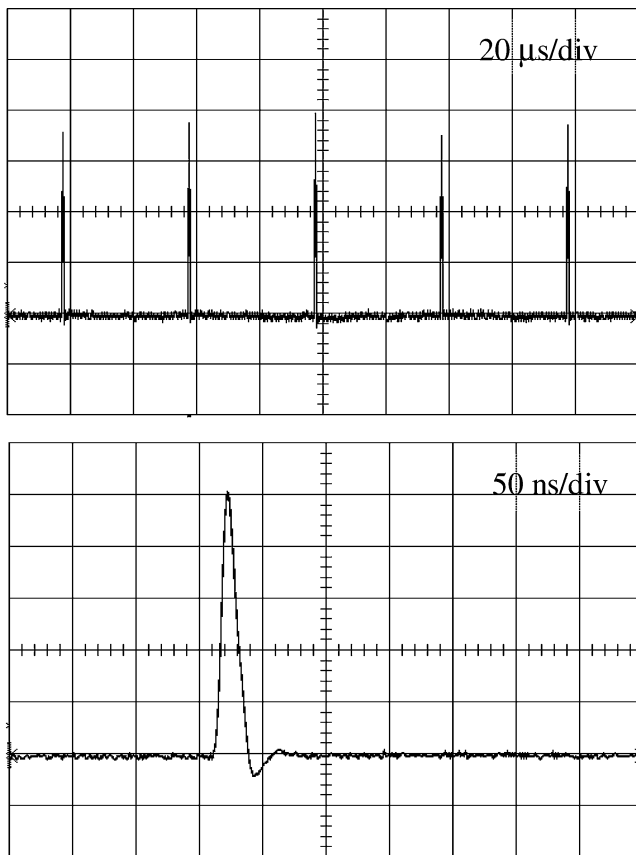


FIGURE 5 Oscilloscope traces of a train of output pulses; the lower trace is an expanded shape of a single pulse

expected, the average blue output power is highest at $\vartheta = 0^\circ$ and is up to 282 mW at an incident pump power of 15 W, corresponding to a conversion efficiency of 1.9% from pump diode input to blue output. The present result is considerably higher than the output power of ~ 55 mW obtained with extra-cavity THG [6, 7]. After the optical elements were thermally

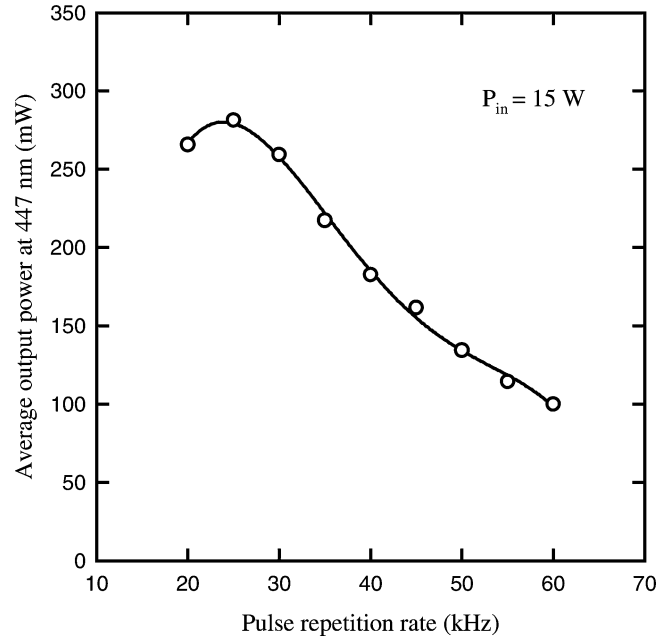


FIGURE 6 The average blue output power at 15 W of pump power as a function of the pulse-repetition rate with the configuration of $\vartheta = 0^\circ$

stabilized, the fluctuations of the average power over hours of operation have been observed to be approximately $\pm 5\%$. The laser performance was reproducible on a day-to-day basis. With the algorithms of knife-edge technique [13], the beam-quality factor at the maximum output power was estimated to be better than 2.0.

Figure 4 shows the peak blue power and pulse width versus diode pump power at a repetition rate of 25 kHz and $\vartheta = 0^\circ$. The pulse width decreases from 25 ns to 14 ns by increasing the pump power from 5 W to 15 W. The maximum blue peak power amounts to 800 W at 15-W pump power. To our knowledge, this is the highest power ever reported for a diode-end-pumped Q-switched Nd:YVO₄ blue laser. The typical output pulse shape is shown in Fig. 5. Figure 6 shows the average blue output power at 15 W of pump power as a function of the pulse-repetition rate with the configuration of $\vartheta = 0^\circ$. To avoid damage to the intracavity optical components, the Q-switcher is operated above 20 kHz. It can be seen that the conversion efficiency falls at a higher repetition rate (> 30 kHz) due to lower power intensities of the fundamental and second-harmonic waves. Even so, the maximum average output power at 447 nm still exceeds 100 mW at a repetition rate of 60 kHz.

We have demonstrated a compact efficient Q-switched Nd:YVO₄ blue laser with an intracavity THG scheme. The conversion efficiencies for intracavity SHG and THG were optimized via controlling the polarization state. In the intracavity SHG experiment, 1.08 W of average red output power at a repetition rate of 25 kHz was obtained by setting the *E* axis of the KTP crystal with respect to the *c* axis of the Nd:YVO₄ crystal at an incident pump power of 15 W. In the intracavity THG experiment, 282 mW of average blue output power with a 14-ns pulse width at a repetition rate of 25 kHz was generated by setting the *O* axis of the LBO crystal to be along the polarization of the second-harmonic wave at an

incident pump power of 15 W. The short pulse width leads to a peak third-harmonic power at 447 nm of up to 800 W.

REFERENCES

- 1 A. Harada, Y. Nihei, Y. Okazaki, H. Hyuga, *Opt. Lett.* **22**, 805 (1997)
- 2 M. Pierrou, F. Laurell, H. Karlsson, T. Kellner, C. Czeranowsky, G. Huber, *Opt. Lett.* **24**, 205 (1999)
- 3 W.P. Risk, W. Length, *Opt. Lett.* **12**, 993 (1987)
- 4 P. Zeller, P. Peuser, *Opt. Lett.* **25**, 34 (2000)
- 5 S. Bjurshagen, D. Evekull, R. Koch, *Electron. Lett.* **38**, 324 (2002)
- 6 G.Z. Luo, S.N. Zhu, J.L. He, Y.Y. Zhu, H.T. Wang, Z.W. Liu, C. Zhang, N.B. Ming, *Appl. Phys. Lett.* **78**, 3006 (2001)
- 7 X. Mu, W. Shi, Y.J. Ding, *J. Appl. Phys.* **93**, 9437 (2003)
- 8 R.A. Stolzenberger, C.C. Hsu, N. Peyghambarian, J.E. Reid, R.A. Morgan, *IEEE Photon. Technol. Lett.* **1**, 446 (1989)
- 9 X. Mu, Y.J. Ding, in *Digest of Technical Papers of CLEO 2002* (Optical Society of America, Washington, DC, 2002), paper CtuG3, p. 166
- 10 G.W. Ross, N.S. Felgate, W.A. Clarkson, P.G.R. Smith, P.E. Britton, D.C. Hanna, in *Digest of Technical Papers of CLEO 1998* (Optical Society of America, Washington, DC, 1998), paper CThN6, p. 384
- 11 Y.F. Chen, *IEEE J. Quantum Electron.* **35**, 234 (1999)
- 12 L. Friob, P. Mandel, E.A. Viktorov, *Quantum Semiclass. Opt.* **10**, 1 (1998)
- 13 A.E. Siegman, M.W. Sasnett, T.F. Johnston, Jr., *IEEE J. Quantum Electron.* **27**, 1098 (1991)

Quantum signatures of nonlinear resonances in mesoscopic systems: Efficient extension of localized wave functions

Y. F. Chen, T. H. Lu, K. W. Su, and K. F. Huang

Department of Electrophysics, National Chiao Tung University, Hsinchu, Taiwan

(Received 17 June 2005; revised manuscript received 12 August 2005; published 16 November 2005)

We investigate the quantum signatures of classical nonlinear resonances by making the analytic connection between the quantum wave functions and the classical periodic orbits for the uncoupled systems. It is found that the highly efficient extension of the localized coherent states within the classical caustics is an intriguing phenomenon in mesoscopic systems with nonlinear resonances. With the theoretical analysis, we experimentally demonstrate that the laser resonator with an intracavity saturable absorber can be employed to visualize the wave patterns analogous to the quantum wave functions associated with Fermi resonance.

DOI: [10.1103/PhysRevE.72.056210](https://doi.org/10.1103/PhysRevE.72.056210)

PACS number(s): 05.45.Mt, 03.65.Ge, 45.05.+x, 42.60.Jf

I. INTRODUCTION

Investigations of the quantum ballistic transport in nanostructure devices have revealed that the intriguing observations of conductance fluctuations are closely related to the quantum wave functions associated with the classical periodic orbits [1–6]. In recent years, there has been growing attention to quantum manifestations of classical periodic orbits in mesoscopic systems [7–17]. Nonlinear resonances, which are originally described by Fermi in the molecule of CO₂ [18], have been shown to have a dramatic influence on the shapes of classical trajectories [19]. The phenomenon of nonlinear resonances play a crucial role in experimental studies of molecular excitations, tunneling effect, stellar trajectories, as well as other theoretical works [19–22]. Therefore, the connection between the quantum wave functions and the classical trajectories in mesoscopic systems with internal nonlinear resonances is important for understanding the quantum features of nonlinear classical dynamics, which is also a central issue in modern physics.

A single trajectory in the coupled Fermi resonance system often sweeps out a region similar to that described by an ensemble of periodic orbits in the uncoupled system [19]. Therefore, the wave functions related to classical periodic orbits in the zero-order systems can serve as an excellent basis to manifest the quantum effect of nonlinear resonances. In this paper, we analytically construct the connection between the quantum wave functions and the classical periodic orbits to investigate the quantum signatures of classical nonlinear resonances in mesoscopic systems. With the analytical formalism, we disclose that only a few localized stationary states in mesoscopic systems are already sufficient to extend wave patterns within the classical caustics to reveal the quantum features of nonlinear resonances. Moreover, we experimentally demonstrate that the quantum wave functions associated with 2:1 coupled resonance can be analogously visualized from the laser patterns emitted from a nearly hemispherical laser cavity with an intracavity saturable absorber.

II. CLASSICAL TRAJECTORIES IN THE 2D HARMONIC OSCILLATOR WITH NONLINEAR RESONANCE

A single classical trajectory in the coupled resonance system is usually found to cover a region similar to that of an

ensemble of periodic orbits in the uncoupled system [19]. Here we present a brief synopsis for the purpose of completeness. Considering the 2D harmonic oscillator with nonlinear resonances, the Hamiltonian for this system can be generally modeled as

$$H = H_o + V_c, \quad (1)$$

where V_c is the coupling potential and

$$H_o = \frac{1}{2}(p_x^2 + p_y^2 + \omega_x^2 x^2 + \omega_y^2 y^2), \quad (2)$$

where $\omega_x = q\omega$ and $\omega_y = p\omega$, ω is the common factor of the frequencies by ω_x and ω_y , and p and q are relative prime integers. In terms of action-angle variables $(J_x, J_y, \phi_x, \phi_y)$ and the particle mass m , the representation for the trajectories of Eq. (2) is given by

$$x(t) = \sqrt{\frac{2J_x}{m(q\omega)}} \cos(q\omega t - \phi_x), \quad (3a)$$

$$y(t) = \sqrt{\frac{2J_y}{m(p\omega)}} \cos(p\omega t - \phi_y). \quad (3b)$$

The trajectories for Eq. (3) are the so-called Lissajous figures. Furthermore, four constants of motion for the zero-order system in Eq. (2) are given by [23,24]

$$J = \frac{H_o}{qp\omega} = \frac{1}{qp}(qJ_x + pJ_y), \quad (4a)$$

$$\Delta = \frac{1}{qp}(qJ_x - pJ_y), \quad (4b)$$

$$K = \sqrt{\frac{2J_x J_y}{qp}} \cos(p\phi_x - q\phi_y), \quad (4c)$$

$$L = \sqrt{\frac{2J_x J_y}{qp}} \sin(p\phi_x - q\phi_y). \quad (4d)$$

An ensemble of the Lissajous trajectories for a given values of the Cartesian actions (J_x, J_y) is to form a rectangular caus-

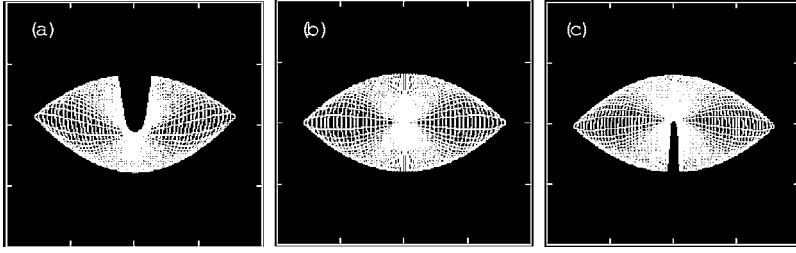


FIG. 1. Family of periodic orbits for the zero-order system with $p:q=2:1$ at a fixed $J=24$ and (a) $K=8$, (b) $K=0$, and (c) $K=-3$.

tic in (x, y) space. Alternatively, J and one of the remaining constants of motion (Δ, K, L) can be used to generate an ensemble of Lissajous trajectories with different shapes of the caustics. Figure 1 depicts the calculated results for a family of trajectories in the zero-order (uncoupled) system with different K values and $J=24$.

To demonstrate the characteristics of the classical trajectories in the coupled system, the coupling potential that is originally considered by Noid *et al.* is employed:

$$V_c = \varepsilon y(x^2 + \eta y^2). \quad (5)$$

Figure 2 displays the numerical results for the typical trajectories of the coupled systems in Eq. (1) for different initial conditions with the parameters of $2\omega_x = \omega_y = 2.0$, $\hbar = 1$, $\varepsilon = -0.03$, $\eta = -0.2$, and $J = 24$. It is clear that the sweeping region of a single trajectory in the coupled system is similar to the caustic formed by an ensemble of the uncoupled system, as shown in Fig. 1. This similarity means that the quantum effect of classical nonlinear resonance can be manifested with the quantum wave functions related to classical periodic orbits in the zero-order systems. As a consequence, the connection between the quantum wave functions and the classical periodic orbits for the zero-order systems can be employed to manifest the quantum features of classical nonlinear resonance [25,26].

III. DERIVATION OF QUANTUM WAVE FUNCTIONS ASSOCIATED WITH CLASSICAL LISSAJOUS TRAJECTORIES

The conventional eigenstates of a 2D harmonic oscillator with commensurate frequencies do not reveal the characteristics of classical Lissajous figures even in the correspondence limit of large quantum number. It is well known that Schrödinger in 1926 [27] originally constructed a coherent state of a one-dimensional (1D) harmonic oscillator to describe a classical particle with a wave packet whose center in the time evolution follows the corresponding classical motion. Extended to 2D system, the Schrödinger coherent state is expected to correspond to a wave packet with its center

generally moving along a classical trajectory. This exact correspondence enables us to derive the quantum stationary states localized on the classical Lissajous orbits from the time-dependent Schrödinger coherent state.

Since the Hamiltonian is separable, the Schrödinger coherent state for a 2D harmonic oscillator can be expressed as [27]

$$|\alpha_x, \alpha_y\rangle = \left(\sum_{n_1=0}^{\infty} \frac{|\alpha_x|^{n_1} e^{in_1\phi_x}}{\sqrt{n_1!}} e^{|\alpha_x|^2/2} |n_1\rangle_x e^{-i(n_1+1/2)\omega_x t} \right) \times \left(\sum_{n_2=0}^{\infty} \frac{|\alpha_y|^{n_2} e^{in_2\phi_y}}{\sqrt{n_2!}} e^{|\alpha_y|^2/2} |n_2\rangle_y e^{-i(n_2+1/2)\omega_y t} \right). \quad (6)$$

It can be analytically deduced that the probability density for the coherent state $|\alpha_x, \alpha_y\rangle$ follows the motion of a classical 2D isotropic harmonic oscillator, i.e.,

$$x(t) = \sqrt{\frac{2\hbar}{m\omega_x}} |\alpha_x| \cos(\omega_x t - \phi_x),$$

$$y(t) = \sqrt{\frac{2\hbar}{m\omega_y}} |\alpha_y| \cos(\omega_y t - \phi_y). \quad (7)$$

With this result, the coherent state $|\alpha_x, \alpha_y\rangle$ can be related to the classical trajectory in Eq. (3) by use of the following substitutions:

$$\alpha_x = \sqrt{\frac{J_x}{\hbar}} e^{i\phi_x}, \quad \alpha_y = \sqrt{\frac{J_y}{\hbar}} e^{i\phi_y}. \quad (8)$$

Consider the case of the ratio $\omega_x:\omega_y=q:p$, the set of states with indices (n_1, n_2) in Eq. (6) can be divided into subsets characterized by a pair of indices (u_1, u_2) given by $n_1 \equiv u_1 \pmod{p}$ and $n_2 \equiv u_2 \pmod{q}$. In terms of these subsets and the action-angle variables $(J_x, J_y, \phi_x, \phi_y)$ in Eq. (8), the Schrödinger coherent state in Eq. (6) can be rewritten as

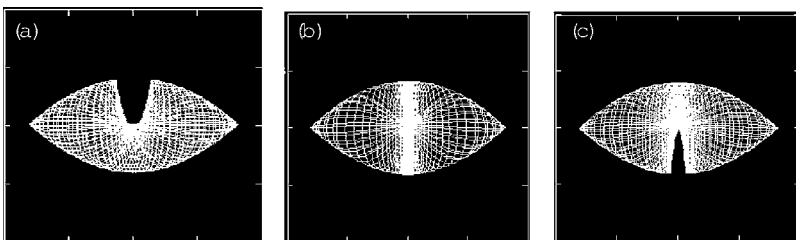


FIG. 2. Classical trajectories for Hamiltonian in Eq. (1) with the coupling potential in Eq. (5) at a fixed $J=24$ and different initial conditions chosen such that the sweeping regions of (a)–(c) similar to the K representation shown in Figs. 1(a)–1(c), respectively.

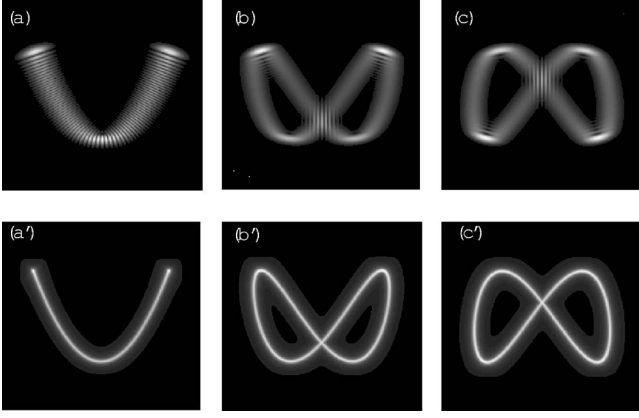


FIG. 3. Comparison between the quantum stationary state $|\Psi_N^{p,q}(x,y;A,\phi)\rangle^2$ [(a)–(c)] and the classical Lissajous orbits [(a')–(c')] for the system of $p:q=2:1$ with $N=40$, $A=5.2$ and (a) $\phi=0$, (b) $\phi=0.3\pi$, and (c) $\phi=0.6\pi$.

$$\begin{aligned}
 |\alpha_x, \alpha_y\rangle = & \left(\sum_{u_1=0}^{p-1} \sum_{N_1=0}^{\infty} \frac{(\sqrt{J_x/\hbar})^{pN_1+u_1} e^{i(pN_1+u_1)\phi_x}}{\sqrt{(pN_1+u_1)!}} \right. \\
 & \times e^{J_x/2\hbar} |pN_1+u_1\rangle_x e^{-i(pN_1+u_1+1/2)q\omega t} \left. \right) \\
 & \times \left(\sum_{u_2=0}^{q-1} \sum_{N_2=0}^{\infty} \frac{(\sqrt{J_y/\hbar})^{qN_2+u_2} e^{i(qN_2+u_2)\phi_y}}{\sqrt{(qN_2+u_2)!}} \right. \\
 & \times e^{J_y/2\hbar} |qN_2+u_2\rangle_y e^{-i(qN_2+u_2+1/2)p\omega t} \left. \right). \quad (9)
 \end{aligned}$$

As seen in Eq. (9), the 2D Schrödinger coherent state is divided into a product of two infinite series and two finite series. The method of the triangular partial sums is used to make precise sense out of the product of two infinite series in Eq. (9). Mathematically, the notion of triangular partial sums is called the Cauchy product of the double infinite series [28]. With the representation of the Cauchy product, the terms $|pN_1+u_1\rangle_x |qN_2+u_2\rangle_y$ in Eq. (9) can be arranged diago-

nally by grouping together those terms for which $N_x+N_y=N$:

$$\begin{aligned}
 |\alpha_x, \alpha_y\rangle = & \sum_{N=0}^{\infty} e^{(J_x+J_y)/2\hbar} \sum_{u_2=0}^{q-1} \sum_{u_1=0}^{p-1} e^{-i[Npq+(u_1+1/2)q+(u_2+1/2)p]\omega t} \\
 & \times \left\{ \sum_{K=0}^N \frac{(\sqrt{J_x/\hbar})^{pK+u_1} (\sqrt{J_y/\hbar})^{q(N-K)+u_2}}{\sqrt{(pK+u_1)!} \sqrt{[q(N-K)+u_2]!}} \right. \\
 & \left. \times |pK+u_1\rangle_x |q(N-K)+u_2\rangle_y \right\}. \quad (10)
 \end{aligned}$$

After some algebra, Eq. (10) can be rewritten as

$$\begin{aligned}
 |\alpha_x, \alpha_y\rangle = & \sum_{N=0}^{\infty} e^{(J_x+J_y)/2\hbar} \sum_{u_2=0}^{q-1} \sum_{u_1=0}^{p-1} e^{-i[Npq+(u_1+1/2)q+(u_2+1/2)p]\omega t} \\
 & \times \left(\sqrt{\frac{J_x}{\hbar}} e^{i\phi_x} \right)^{u_1} \left(\sqrt{\frac{J_y}{\hbar}} e^{i\phi_y} \right)^{qN+u_2} \\
 & \times \left\{ \sum_{K=0}^N \frac{[\sqrt{(J_x)^p/(J_y)^q} e^{i(p\phi_x-q\phi_y)}]^K}{\sqrt{(pK+u_1)!} \sqrt{[q(N-K)+u_2]!}} \right. \\
 & \left. \times |pK+u_1\rangle_x |q(N-K)+u_2\rangle_y \right\}. \quad (11)
 \end{aligned}$$

The expression in the curly bracket of Eq. (11) represents the stationary coherent states labeled with one major index N and two minor indices u_1 and u_2 . These stationary coherent states are physically expected to be associated with the Lissajous orbits. Since the minor indices u_1 and u_2 essentially do not affect the characteristics of the stationary states, the condition of $u_1=u_2=0$ is used for the following analysis unless otherwise specified. Including the normalization condition, the stationary coherent states in Cartesian coordinates are given by

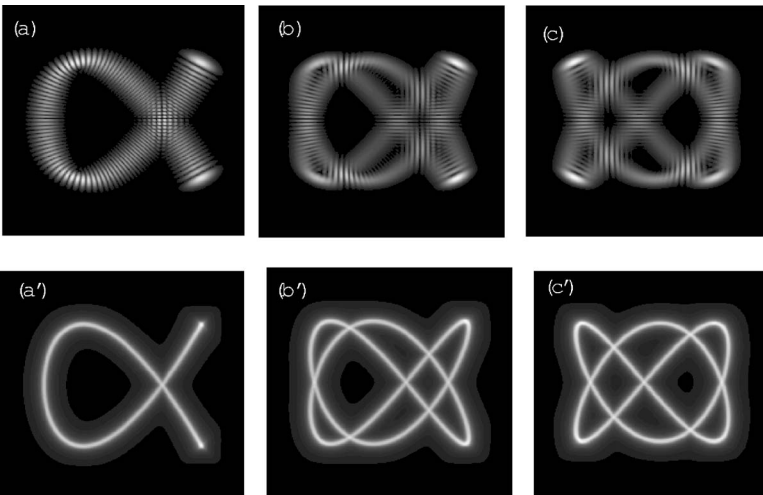


FIG. 4. The same as Fig. 3 for the system of $p:q=3:2$ with $N=22$, $A=5.2$ and (a) $\phi=0$, (b) $\phi=0.3\pi$, and (c) $\phi=0.6\pi$.

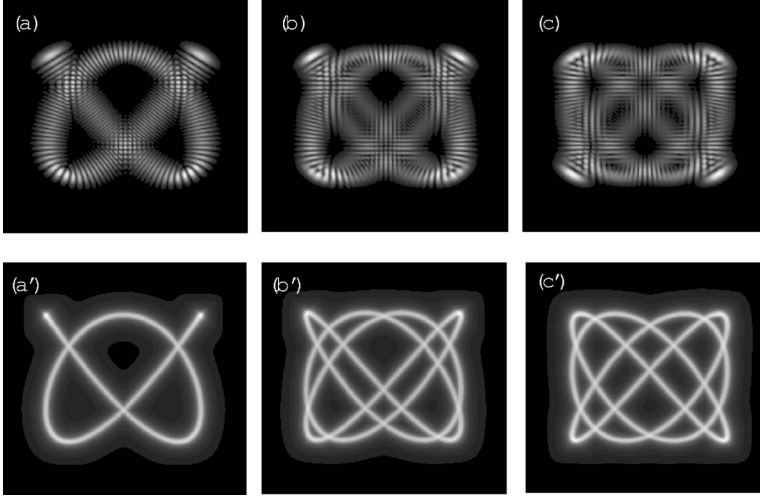


FIG. 5. The same as Fig. 3 for the system of $p:q=4:3$ with $N=15$, $A=5.2$ and (a) $\phi=0$, (b) $\phi=0.3\pi$, and (c) $\phi=0.6\pi$.

$$\begin{aligned} \Psi_N^{p,q}(x,y;A,\phi) &= \left[\sum_{K=0}^N \frac{A^{2K}}{(pK)! [q(N-K)]!} \right]^{-1/2} \\ &\times \sum_{K=0}^N \frac{(Ae^{i\phi})^K}{\sqrt{(pK)! [q(N-K)]!}} \Phi_{pK}(x;\lambda_x) \\ &\times \Phi_{q(N-K)}(y;\lambda_y), \end{aligned} \quad (12)$$

where

$$A = \sqrt{(J_x)^p / (J_y)^q}, \quad (13)$$

$$\phi = p\phi_x - q\phi_y, \quad (14)$$

$$\Phi_n(x;\lambda) = \langle x|n\rangle_x = \sqrt{\frac{\sqrt{\lambda}}{2^n n! \sqrt{\pi}}} H_n(\sqrt{\lambda}x) e^{-\lambda x^2/2}, \quad (15)$$

$H_n(\dots)$ are the Hermite polynomials, $\lambda_x = m\omega_x/\hbar$, and $\lambda_y = m\omega_y/\hbar$. Equation (12) reveals that the stationary coherent states associated with the Lissajous orbits are the superposition of degenerate eigenstates with the relative amplitude factor A and phase factor ϕ . Equations (13) and (14) indicate that the relative amplitude factor A and phase factor ϕ in the stationary coherent states $\Psi_N^{p,q}(x,y;A,\phi)$ are explicitly related to the classical action-angle variables $(J_x, J_y, \phi_x, \phi_y)$.

From Eq. (11), the eigenenergies of the stationary coherent states $\Psi_N^{p,q}(x,y;A,\phi)$ are found to be

$$E_N = \left[Npq + \frac{1}{2}q + \frac{1}{2}p \right]_{N \gg 1} \hbar\omega \rightarrow (Npq)\hbar\omega. \quad (16)$$

In comparison of Eq. (16) with Eq. (4a), the relationship between the index N and the classical action J is given by

$$J = N\hbar. \quad (17)$$

With Eqs. (12)–(17), the connection between the quantum wave functions and the classical Lissajous orbits is completely manifested. Figures 3–5 depict the comparison between the quantum wave patterns $|\Psi_N^{p,q}(x,y;A,\phi)|^2$ and the corresponding classical periodic orbits for $p:q$ to be 2:1, 3:2, and 4:3, respectively. Here three different phase factors, $\phi=0$, $\phi=0.3\pi$, and $\phi=0.6\pi$, are displayed in each fig-

ure for the purpose of clear comparison. The behavior of the quantum wave patterns in all cases can be found to be in precise agreement with the classical Lissajous figures.

It is worthwhile to mention that the stationary states $\Psi_N^{p,q}(x,y;A,\phi)$ for the 2D isotropic harmonic oscillator, i.e., $p:q=1:1$, can be simplified to give rise to the well-known expression of SU(2) elliptic states [29–32]:

$$\begin{aligned} \Psi_N(x,y;A,\phi) &= [1 + A^2]^{-N/2} \sum_{K=0}^N \frac{\sqrt{N!}}{\sqrt{K!} \sqrt{(N-K)!}} \\ &\times (Ae^{i\phi})^K \Phi_K(x;\lambda) \Phi_{N-K}(y;\lambda). \end{aligned} \quad (18)$$

In other words, the stationary states $\Psi_N^{p,q}(x,y;A,\phi)$ in Eq. (12) are a kind of SU(2) coherent states. To our knowledge, it is original to derive the stationary coherent states related to the classical Lissajous orbits from the time-dependent Schrödinger coherent state. Since the stationary coherent states $\Psi_N^{p,q}(x,y;A,\phi)$ are well localized on the classical periodic orbits, we call them “localized states.”

IV. QUANTUM FEATURES OF CLASSICAL NONLINEAR RESONANCES

As mentioned in Sec. II a classical trajectory in the weakly perturbed systems can be characterized by an ensemble of the unperturbed periodic orbits. The quantum fea-

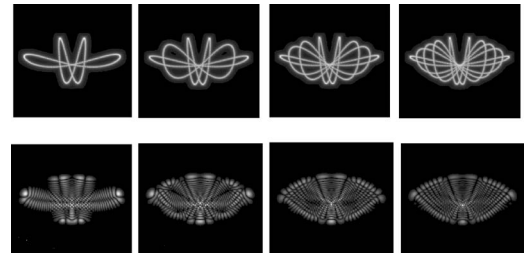


FIG. 6. Calculated results for the variation of the coherent wave patterns (real part) with the number of participant localized states. Top: classical Lissajous trajectories. Bottom: quantum stationary states.

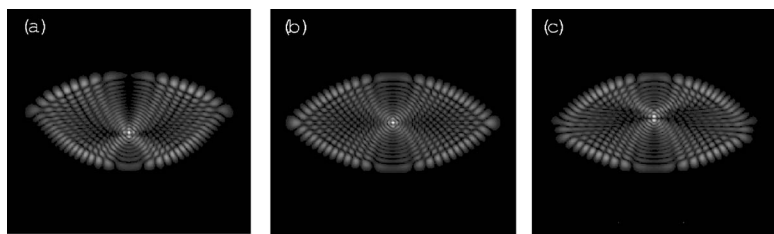


FIG. 7. Quantum wave patterns corresponding to the classical tori shown in Fig. 1.

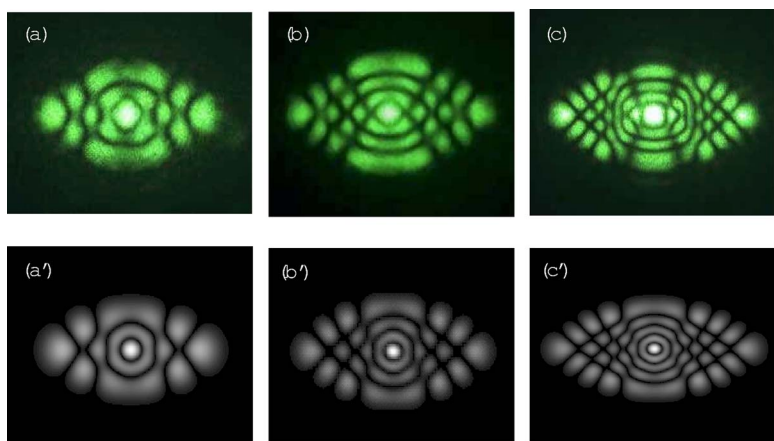


FIG. 8. (Color online) Comparison between the experimental wave patterns [(a)–(c)] observed in the laser experiment and the theoretical patterns of quantum coherent states [(a)–(c)] in a 2:1 intrinsic Fermi resonance.

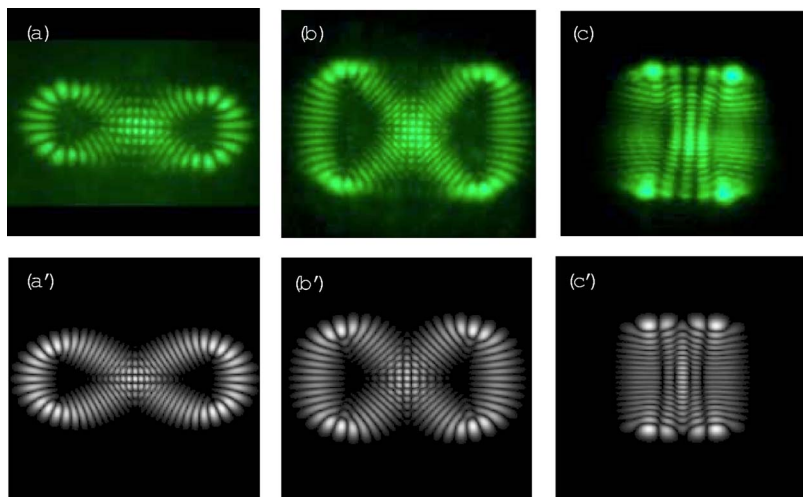


FIG. 9. (Color online) Experimental far-field wave patterns [(a)–(c)] for the stationary figure-eight states that were generated at three different pump positions on the laser crystal, respectively. Theoretical patterns of quantum coherent states $|\Psi_{20}^{2,1}(x,y;A,\pi/2)|^2$ (real part) corresponding to the experimental results: (a) $A=10$, (b) $A=5$, (c) $A=1$.

tures of classical nonlinear resonance can be manifested with a coherent superposition of an ensemble of the localized states. Figure 6 displays the variation of the coherent wave patterns with the number of participant localized states corresponding to the trajectory in Fig. 1(a). It is found that only a few localized states are already sufficient to form a well extended pattern within the classical caustics, similar to a kaleidoscopic pattern. The high efficiency of the wave extension comes from the fact that the encompassing region of each localized state covers a width of several de Broglie wavelengths. Since the de Broglie wavelength is inversely proportional to \sqrt{N} , the critical number of localized states for a well extended pattern is of order \sqrt{N} . In other words, the highly efficient extension of the wave pattern is a salient quantum phenomenon in mesoscopic systems with nonlinear resonances. Figure 7 depicts the quantum wave functions corresponding to the classical tori shown in Fig. 1. A close classical quantum correspondence can be clearly seen; the quantum wave distributions are well extended within the associated classical caustics. In the following section, we give an intriguing demonstration that the laser cavity is a promising analogous experiment for visualizing the quantum wave functions associated with nonlinear resonances.

V. ANALOGOUS EXPERIMENTAL OBSERVATIONS

In recent years, microwave cavities have been used to perform analog studies of transport in open quantum dots [33–35]. Recently, Doya *et al.* [36] have introduced the paraxial approximation to establish an analogy between light propagation along a multimode fiber and quantum confined systems. Furthermore, we have demonstrated that it is promising to explore the high-order quantum wave function from the pattern formation of the laser resonators [37–39]. This demonstration is based on the fact that the wave equation for the transverse mode of the laser resonators in the paraxial approximation is in analogy with the Schrödinger equation for the 2D quantum confined systems [40,41]. More recently, we have observed the kaleidoscope of laser patterns in a near-hemispheric microchip laser with an intracavity saturable absorber [42]. However, the origin of the salient pattern formation was not clearly understood at that moment. Here we demonstrate that the observed laser modes are a kind of analogous wave patterns associated with the quantum coherent states in a 2:1 stretch-bend Fermi resonance.

The experimental configuration in Ref. [42] is a near-hemispheric cavity in which the transverse mode spacing $\Delta\nu_T$ and the longitudinal mode spacing $\Delta\nu_L$ are very close to be commensurable, i.e., $\Delta\nu_L:\Delta\nu_T \approx 2:1$. The inherent commensurability between $\Delta\nu_T$ and $\Delta\nu_L$ have a dramatic effect on the formation of laser patterns, as shown in the internal nonlinear resonances. In other words, the coupling of a 2:1 longitudinal-transverse resonance is identical in form to the well-known phenomenon of Fermi resonance in molecular systems. We have redone the experiment but with a semiconductor quantum well instead of a bulk crystal as a saturable absorber in the laser cavity. Similar patterns to those found in Ref. [42] can be almost reproduced. This similarity implies that the observed patterns are insensitive to the types of the

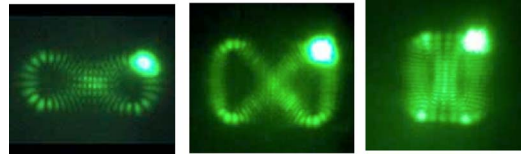


FIG. 10. (Color online) Experimental images of the wave intensities on the laser crystal corresponding to the experimental far-field patterns shown in Fig. 9, respectively. The bright spot on the experimental image represents the location of the pump beam.

saturable absorbers, even though the saturable absorber provides a source of nonlinear coupling. As shown in Fig. 8, the formation of the observed laser patterns can be well explained with the quantum coherent states of a 2:1 intrinsic Fermi resonance. Note that the bright spot near the center of the kaleidoscopic patterns arises from the quantum-classical correspondence that all figure-eight classical orbits pass through the focal point near origin. The excellent agreement between the experimental and theoretical patterns confirms that the coupling of a 2:1 longitudinal-transverse resonance in a near-hemispheric laser resonator is analogous to the well-known phenomenon of Fermi resonance in molecular systems. The present analysis also provides a further indication that laser resonators can be designed to demonstrate the quantum phenomenon in mesoscopic physics [43].

With the same laser cavity configuration, the stationary localized states related to the single figure-eight classical orbits can be excited by use of the off-axis pumping scheme. Figure 9 shows three experimental far-field patterns for the stationary figure-eight states that were generated at different off-axis pump positions on the laser crystal, respectively. The theoretical patterns corresponding to the experimental results are also plotted in Fig. 9 for comparison. Again, excellent agreement is found for all cases. Figure 10 shows the experimental images of the field intensities on the laser crystal to reveal the relationship between the pump positions and the formation of the stationary localized states. The bright spot on the experimental image in Fig. 10 represents the location of the pump beam. It can be seen that the formation of the stationary figure-eight states is primarily dependent on the overlap between the pump intensity and the lasing mode distribution. This is consistent with the fact that the cavity mode with the biggest overlap with the gain region will dominate the lasing process. As a consequence, controlling the pump position can straightforwardly manipulate the generation of different stationary localized figure-eight states in a near-hemispheric resonator. Nowadays, manipulation of the spatially localized optical wave may be promising for optical information process applications [44]. One central part of the theory in Sec. III is to derive the analytical representation for the stationary Lissajous states. Our experimental results illustrate that this analytical representation is not only important for understanding the quantum features of the mesoscopic states with nonlinear coupling but also useful for providing the idea to manipulate the generation of the stationary localized states in laser cavities. For the first time to our knowledge, the analytic representation for the stationary Lissajous states is derived and employed to explore the manipulation properties of the coherent optical wave in a degenerate laser cavity.

VI. CONCLUSIONS

In summary, we have analytically derived the stationary coherent states associated with the classical Lissajous orbits from the Schrödinger coherent states for the 2D harmonic oscillators with commensurate frequencies. We have employed the connection between the quantum wave functions and the classical Lissajous orbits for the zero-order systems to investigate the quantum features of classical nonlinear resonances. It is found that the highly efficient extension of the quantum wave functions within the classical caustics is an intriguing phenomenon in mesoscopic systems with non-

linear coupling resonances. Furthermore, we have theoretically and experimentally demonstrated that a nearly hemispherical laser resonator with an intracavity saturable absorber forms an experimental system for visualizing the quantum wave functions associated with Fermi resonance.

ACKNOWLEDGMENT

The author thanks the National Science Council for their financial support of this research under Contract No. NSC-94-2112-M-009-034.

-
- [1] J. P. Bird, R. Akis, D. K. Ferry, A. P. S. de Moura, Y. C. Lai, and K. M. Indlekofer, *Rep. Prog. Phys.* **66**, 583 (2003).
- [2] I. V. Zozoulenko and K. F. Berggren, *Phys. Rev. B* **56**, 6931 (1997).
- [3] Y. Takagaki and K. H. Ploog, *Phys. Rev. E* **62**, 4804 (2000).
- [4] D. K. Ferry, R. Akis, and J. P. Bird, *J. Phys.: Condens. Matter* **17**, S1017 (2005).
- [5] L. Christensson, H. Linke, P. Ornlind, P. E. Lindelof, I. V. Zozoulenko, and K. F. Berggren, *Phys. Rev. B* **57**, 12306 (1998).
- [6] Y. H. Kim, M. Barth, U. Kuhl, H. J. Stöckmann, and J. P. Bird, *Phys. Rev. B* **68**, 045315 (2003).
- [7] W. Li, L. E. Reichl, and B. Wu, *Phys. Rev. E* **65**, 056220 (2002).
- [8] R. Narevich, R. E. Prange, and O. Zaitsev, *Phys. Rev. E* **62**, 2046 (2000).
- [9] J. Wiersig, *Phys. Rev. E* **64**, 026212 (2001).
- [10] J. A. de Sales and J. Florencio, *Physica A* **290**, 101 (2001).
- [11] M. Brack and R. K. Bhaduri, *Semiclassical Physics* (Addison-Wesley, Reading, MA, 1997), Sec. 2.7.
- [12] F. von Oppen, *Phys. Rev. B* **50**, 17151 (1994).
- [13] R. W. Robinett, *Am. J. Phys.* **65**, 1167 (1997).
- [14] Y. F. Chen, K. F. Huang, and Y. P. Lan, *Phys. Rev. E* **66**, 046215 (2002).
- [15] Y. F. Chen, K. F. Huang, and Y. P. Lan, *Phys. Rev. E* **66**, 066210 (2002).
- [16] Y. F. Chen and K. F. Huang, *Phys. Rev. E* **68**, 066207 (2003).
- [17] Y. F. Chen and K. F. Huang, *J. Phys. A* **36**, 7751 (2003).
- [18] E. Fermi, *Z. Phys.* **71**, 250 (1931).
- [19] D. W. Noid, M. L. Koszykowski, and R. A. Marcus, *J. Chem. Phys.* **71**, 2864 (1979).
- [20] D. Farrelly and T. Uzer, *J. Chem. Phys.* **84**, 308 (1986).
- [21] G. Contopoulos and B. Barbanis, *Astron. Astrophys.* **153**, 44 (1985).
- [22] A. Elipe, *Phys. Rev. E* **61**, 6477 (2000).
- [23] H. Goldstein, *Classical Mechanics* (Addison-Wesley, Reading, MA, 1980).
- [24] C. C. Martens and G. S. Ezra, *J. Chem. Phys.* **87**, 284 (1987).
- [25] M. C. Gutzwiller, *Chaos in Classical and Quantum Mechanics* (Springer-Verlag, New York, 1990).
- [26] M. V. Berry and M. Tabor, *Proc. R. Soc. London, Ser. A* **349**, 101 (1976).
- [27] E. Schrödinger, *Naturwiss.* **14**, 644 (1926).
- [28] G. B. Folland, *Advanced Calculus* (Prentice-Hall, Upper Saddle River, NJ, 2002).
- [29] V. Bužek and T. Quang, *J. Opt. Soc. Am. B* **6**, 2447 (1989).
- [30] S. De Bièvre, *J. Phys. A* **25**, 3399 (1992).
- [31] J. Pollet, O. Méplan, and C. Gignoux, *J. Phys. A* **28**, 7287 (1995).
- [32] J. Banerji and G. S. Agarwal, *Opt. Express* **5**, 220 (1999).
- [33] Y. H. Kim, M. Barth, H. J. Stöckmann, and J. P. Bird, *Phys. Rev. B* **65**, 165317 (2002).
- [34] R. G. Nazmitdinov, K. N. Pichugin, I. Rotter, and P. Šeba, *Phys. Rev. B* **66**, 085322 (2002).
- [35] T. Blomquist, H. Schanze, I. V. Zozoulenko, and H. J. Stöckmann, *Phys. Rev. E* **66**, 026217 (2002).
- [36] V. Doya, O. Legrand, F. Mortessagne, and C. Miniatura, *Phys. Rev. Lett.* **88**, 014102 (2002).
- [37] K. F. Huang, Y. F. Chen, H. C. Lai, and Y. P. Lan, *Phys. Rev. Lett.* **89**, 224102 (2002).
- [38] Y. F. Chen and Y. P. Lan, *Phys. Rev. A* **66**, 053812 (2002).
- [39] Y. F. Chen, K. F. Huang, H. C. Lai, and Y. P. Lan, *Phys. Rev. E* **68**, 026210 (2003).
- [40] S. Danakas and P. K. Aravind, *Phys. Rev. A* **45**, 1973 (1992).
- [41] A. E. Siegman, *Lasers* (University Science Books, Mill Valley, CA, 1986).
- [42] Y. F. Chen and Y. P. Lan, *Phys. Rev. Lett.* **93**, 013901 (2004).
- [43] D. Dragoman and M. Dragoman, *Prog. Quantum Electron.* **23**, 131 (1999).
- [44] K. Staliunas, *Transverse Patterns in Nonlinear Optical Resonators*, Springer Tracts in Modern Physics Vol. 183 (Springer, Berlin, 2003), p. 1.

Efficient diode-pumped actively *Q*-switched Nd:YAG/BaWO₄ intracavity Raman laser

Y. F. Chen and K. W. Su

Department of Electrophysics, National Chiao Tung University, Hsinchu, Taiwan

H. J. Zhang, J. Y. Wang, and M. H. Jiang

National Laboratory of Crystal Materials and Institute of Crystal Materials, Shandong University, Shandong, China

Received August 9, 2005; revised manuscript received September 7, 2005; accepted September 9, 2005

Barium tungstate (BaWO₄) is employed to achieve efficient stimulated Raman scattering conversion in a compact diode-pumped actively *Q*-switched Nd:YAG laser. With an incident pump power of 9.2 W, 1.56 W of 1181 nm first-Stokes average output power was generated at a pulse repetition rate of 20 kHz, corresponding to an optical-to-optical conversion efficiency of 16.9%. © 2005 Optical Society of America

OCIS codes: 140.3550, 140.3480.

The development of new Raman crystals has generated a resurgence of interest in solid-state Raman lasers.^{1,2} Until now, the important Raman crystals for achievement of stimulated Raman scattering (SRS) have comprised nitrates [Ba(NO₃)₂],^{3,4} calcites (CaCO₃),^{3,4} iodates (LiIO₃),^{5,6} molybdates (SrMoO₄ and CaMoO₄),⁷ vanadates (YVO₄ and GdVO₄),^{8–10} and tungstates [KGd(WO₄)₂, BaWO₄, CaWO₄, and PbWO₄].^{11–14} Among the tungstate crystals, BaWO₄ is regarded as a promising Raman-active crystal suitable for a wide range of pump pulse durations from picoseconds to nanoseconds.¹⁵

Although the most widespread approach to SRS is based on an external cavity configuration, intracavity SRS systems take advantage of the high intensity inside the laser cavity and use multiple round trips of the pump laser inside the Raman cavity to increase the effective interaction length. Recently Černý *et al.* reported a compact quasi-cw diode-pumped passively *Q*-switched Nd:YAG–BaWO₄ Raman laser with an overall conversion efficiency of 4.4% from diode laser input power to Raman output power.^{15,16} However, actively *Q*-switched intracavity Raman lasers based on BaWO₄ crystals have not yet been achieved to our knowledge.

In this Letter we present our first results on efficient intracavity BaWO₄ SRS generation in a compact, actively *Q*-switched diode-pumped Nd:YAG laser. At an incident pump power of 9.2 W, the compact intracavity SRS system, operating at 20 kHz, produces average output powers at 1181 nm of as much as 1.56 W and a peak power greater than 3 kW.

Figure 1 depicts the experimental configuration of the diode-pumped actively *Q*-switched Nd:YAG/BaWO₄ Raman laser. The cavity mirrors have a special dichroic coating for efficient conversion at the first-Stokes component in an intracavity Raman configuration. The input mirror (M1) is a 500 mm radius-of-curvature concave mirror with an anti-reflection coating at 808 nm on the entrance face ($R < 0.2\%$), a high-reflection (HR) coating at 1000–1200

nm ($R > 99.8\%$), and a high-transmission (HT) coating at 808 nm on the other surface ($T > 90\%$). The output coupler is a flat mirror with a high-reflection coating at 1064 nm ($R > 99.8\%$) and a partial-reflection (PR) coating at 1181 nm ($R = 50\%$). Note that the output coupler's reflectivity is not optimized and it is limited in availability.

The pump source was an 808 nm fiber-coupled laser diode with a core diameter of 800 μm , a numerical aperture of 0.16, and a maximum output power of 10 W. A focusing lens system with 12.5 mm focal length and 90% coupling efficiency was used to reim-age the pump beam into the laser crystal. The waist radius of the pump beam was approximately 300 μm . The laser medium was an 0.8 at. % Nd³⁺:YAG crystal with a length of 10 mm. The Raman-active medium was an *a*-cut BaWO₄ crystal with a length of 10 mm. Both sides of the Nd:YAG and BaWO₄ crystals were coated for antireflection at 1000–1200 nm ($R < 0.2\%$). Furthermore, both crystals were wrapped with indium foil and mounted in water-cooled copper blocks. The water temperature was maintained at 25°C. The 30 mm long acousto-optic (AO) *Q*-switch (NEOS Technologies) had antireflection coatings at 1064 nm on both faces and was driven at a 27.12 MHz center frequency with 15.0 W of rf power. The overall laser cavity length was approximately 10 cm.

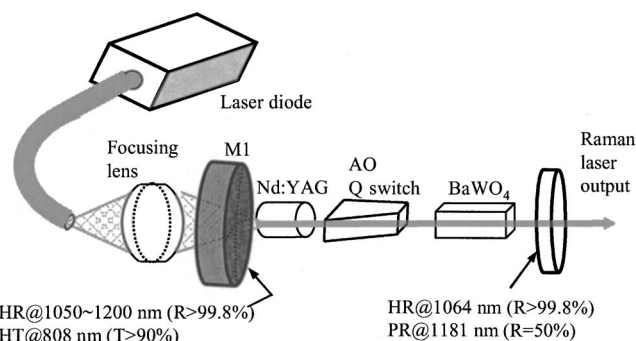


Fig. 1. Schematic of a diode-pumped actively *Q*-switched Nd:YAG–BaWO₄ intracavity Raman laser.

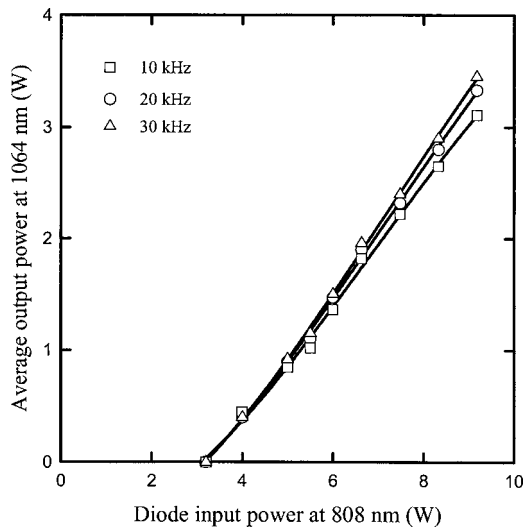


Fig. 2. Average output power at 1064 nm with respect to the incident pump power for pulse repetition rates of 10, 20, and 30 kHz.

First we studied the diode-pumped Q -switched Nd:YAG laser performance at 1064 nm for evaluating the optical-to-optical conversion efficiency of the intracavity SRS. For this investigation, an output coupler with partial reflection at 1064 nm was used instead of the Raman cavity output coupler mentioned above. The optimum reflectivity of the output coupler was approximately 80%. Figure 2 depicts the average output power at 1064 nm with respect to the incident pump power at pulse repetition frequencies (PRFs) of 10, 20, and 30 kHz. The threshold for 1064 nm oscillation was approximately 3.2 W and was insensitive to the PRF. With an incident pump power of 9.2 W, the average output powers at 1064 nm were 3.3–3.5 W for PRFs in the range 10–30 kHz.

When the intracavity Raman laser was used the pumping threshold for the Raman laser output was found to be strongly dependent on the PRF. The spectral information on the intracavity SRS output was measured by an optical spectrum analyzer (Advantest Q8381A) that employs a diffraction grating monochromator to measure high-speed light pulses with a resolution of 0.1 nm. Figure 3 depicts the optical spectrum for the actively Q -switched Nd:YAG–BaWO₄ SRS output. It can be seen that the frequency shift between Stokes and laser lines agrees very well with the optical vibration modes of tetrahedral WO₄²⁻ ionic groups (925 cm⁻¹). Figure 4 shows the average output power for the intracavity SRS laser at 1181 nm as a function of the incident pump power for PRFs of 10, 20, and 30 kHz. The output polarization was found to be along the c axis of the BaWO₄ crystal. For all pump powers, we did not observe the second Stokes. The output power at the fundamental wavelength was of the order of tens of milliwatts. Even though reducing the PRF leads to a lower threshold for Raman output, experimental results revealed that self-focusing-induced damage to the volume of the BaWO₄ Raman crystal usually occurred at a lower PRF. We often induced self-focusing damage in the BaWO₄ Raman crystal by finely ad-

justing the cavity alignment or slightly changing the pump beam for the optimum output. For example, the critical pump power related to the damage threshold induced by self-focusing was approximately 8 W at a PRF of 10 kHz. Nevertheless, the average output power at 1181 nm was as much as 1.56 W at a PRF of 20 kHz with an incident pump power of 9.2 W, corresponding to a conversion efficiency of 47% with respect to the output power available from the fundamental laser of 1064 nm under optimum conditions. As a consequence, the conversion efficiency from diode laser input power to Raman output power was 16.9% at a PRF of 20 kHz. To our knowledge, this is the highest efficiency for a BaWO₄ Raman laser reported to date.

The pulse's temporal behavior was recorded by a LeCroy digital oscilloscope (Wavepro 7100, 10 Gsamples/s, 1 GHz bandwidth) with a fast p - i - n photodiode. The typical time shapes for the fundamental and Raman pulses are shown in Fig. 5. The pulse duration of the Raman output was approxi-

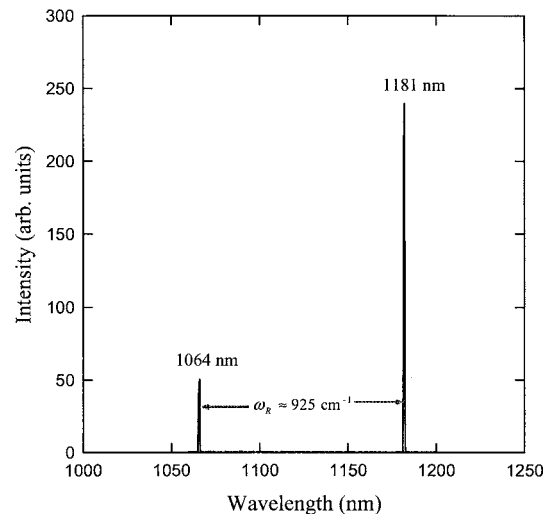


Fig. 3. Optical spectrum for the actively Q -switched intracavity Raman laser.

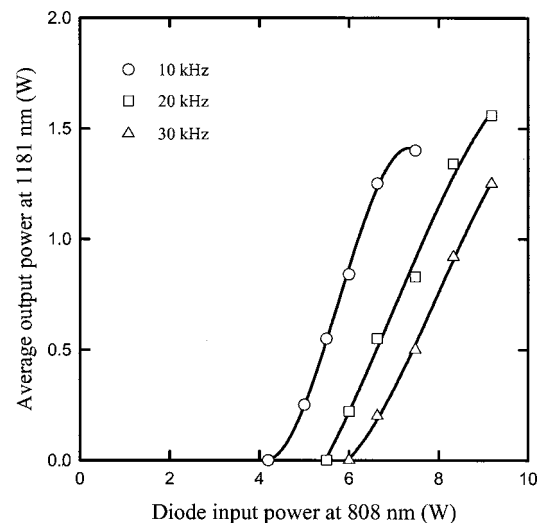


Fig. 4. Average output power at the Stokes wavelength of 1181 nm with respect to the incident pump power for pulse repetition rates of 10, 20, and 30 kHz.

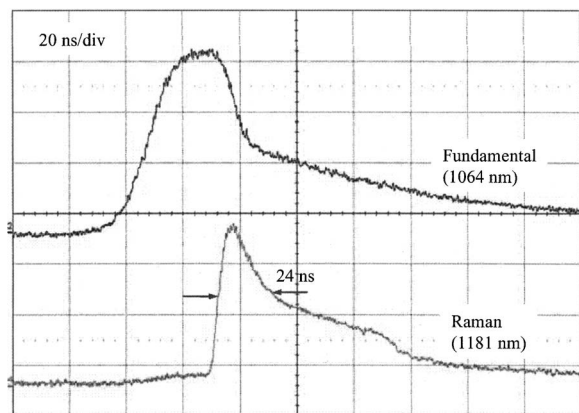


Fig. 5. Typical oscilloscope traces for the fundamental and Raman pulses.

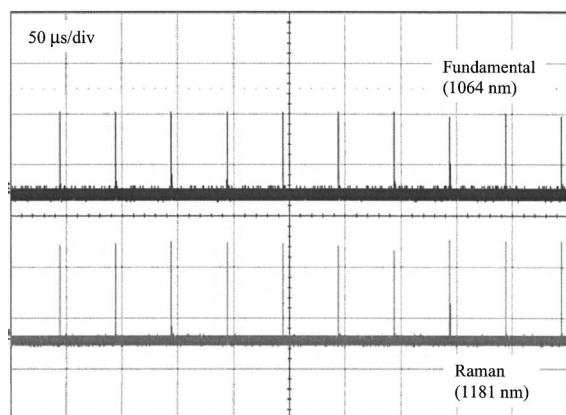


Fig. 6. Oscilloscope traces of a train of the fundamental and Raman output pulses.

mately 24 ns. As a consequence, the peak power was higher than 3.2 kW. Oscilloscope traces of a train of the output pulses are shown in Fig. 6. The pulse-to-pulse amplitude fluctuation was not more than $\pm 10\%$.

In summary, an efficient high-power diode-pumped actively Q -switched Nd:YAG–BaWO₄ intracavity Raman laser has been demonstrated. With an incident pump power of 9.2 W, as much as 1.56 W of average power at the Stokes wavelength was generated at a pulse repetition rate of 20 kHz, corresponding to an

optical-to-optical conversion efficiency of 16.9%. Experimental results indicate that the effect of self-focusing-induced damage is a critical issue for power scale-up of intracavity BaWO₄ SRS.

The laser experiments described here were supported by the National Science Council of Taiwan (contract NSC-92-2112-M-009-013), and the BaWO₄ samples were supported by grants from State Key Programs of China (grant 2004CB19002) and the National Natural Science Foundation of China (grant 50590401). Y. F. Chen's e-mail address is yfchen@cc.nctu.edu.tw.

References

1. H. M. Pask, *Prog. Quantum Electron.* **27**, 3 (2003).
2. J. T. Murray, W. L. Austin, and R. C. Powell, *Opt. Mater.* **11**, 353 (1999).
3. S. N. Karpukhin and A. I. Stepanov, *Sov. J. Quantum Electron.* **16**, 1027 (1986).
4. A. S. Eremenko, S. N. Karpukhin, and A. I. Stepanov, *Sov. J. Quantum Electron.* **10**, 113 (1980).
5. E. O. Ammann and C. D. Decker, *J. Appl. Phys.* **48**, 1973 (1977).
6. H. M. Pask and J. A. Piper, *IEEE J. Quantum Electron.* **36**, 949 (2000).
7. T. T. Basiev, A. A. Sobol, P. G. Zverev, V. V. Osiko, and R. C. Powell, *Appl. Opt.* **38**, 594 (1999).
8. A. A. Kaminskii, K. Ueda, H. J. Eichler, Y. Kuwano, H. Kouta, S. N. Bagaev, T. H. Chyba, J. C. Barnes, G. M. A. Gad, T. Murai, and J. Lu, *Opt. Commun.* **194**, 201 (2001).
9. Y. F. Chen, *Opt. Lett.* **29**, 1915 (2004).
10. Y. F. Chen, *Opt. Lett.* **29**, 2632 (2004).
11. A. V. Gul'in, G. I. Narkhova, and N. S. Ustimenko, *Quantum Electron.* **28**, 804 (1998).
12. K. Andryunas, Yu. Vishchakas, V. Kabelka, I. V. Mochalov, A. A. Pavlyuk, G. T. Petrovskii, and V. Syrus, *JETP Lett.* **42**, 410 (1985).
13. J. Findeisen, H. J. Eichler, and A. A. Kaminskii, *IEEE J. Quantum Electron.* **35**, 173 (1999).
14. A. Kaminskii, H. Eichler, K. Ueda, N. Klassen, B. Redkin, L. Li, J. Findeisen, D. Jaque, J. Garcia-Sole, J. Fernandez, and R. Balda, *Appl. Opt.* **38**, 4533 (1999).
15. P. Černý, H. Jelínková, P. G. Zverev, and T. T. Basiev, *Prog. Quantum Electron.* **28**, 113 (2004).
16. P. Černý, W. Žendzian, J. Jabczyński, H. Jelínková, J. Šulc, and K. Kopczyński, *Opt. Commun.* **209**, 403 (2002).

Manifestation of Weak Localization and Long-Range Correlation in Disordered Wave Functions from Conical Second Harmonic Generation

Y. F. Chen,* K. W. Su, T. H. Lu, and K. F. Huang

Department of Electrophysics, National Chiao Tung University, Hsinchu, Taiwan

(Received 3 November 2005; published 26 January 2006)

We experimentally demonstrate that the near-field patterns of conical second harmonic generation of a laser in random domain structures can be used to explore the spatial structure of two-dimensional disordered wave functions with weak localization. The statistics of the experimental near-field patterns agree very well with the theoretical distributions. In addition to the short-range correlation, the localization effects are found to contribute a nearly constant value to the long-range correlation. The result of this Letter also confirms the possibility of using conical second harmonic generation as a diagnostic tool for topographical characterization of crystals.

DOI: [10.1103/PhysRevLett.96.033905](https://doi.org/10.1103/PhysRevLett.96.033905)

PACS numbers: 42.25.Dd, 42.55.Xi, 42.65.Ky, 72.15.Rn

Interference effects between scattered waves lead to striking phenomena beyond the radiative transfer treatment and diffusion theory [1]. Weak localization (WL) is a hallmark of interference of multiply scattered waves in disordered media [2–4] and is a direct consequence of the constructive interference between reciprocal paths in wave scattering [5]. The phenomenon of weak localization has been extensively studied in coherent backscattering from colloidal suspension [6], strongly scattering powders [7], cold atom gases [8], two-dimensional (2D) random systems [9], randomized laser materials [10], disordered liquid crystals [11], and disordered microcavities [12]. Especially, microwave experiments have provided direct observation of quantum wave functions in disordered quantum billiards [13]. Even so, there have been few experimental studies of quantum disordered wave functions because of their lack of accessibility.

The underlying wave nature of the particles leads to the striking feature that the propagation of electrons in conducting devices shows many similarities with random multiple scattering of light in disordered media [2–4]. This relevance stimulated active research in the propagation of light waves in random scattering media since the 1980s [6]. Recently, it has been observed that multiple scattering of laser light in a microdomained nonlinear crystal constitutes a novel mechanism for conical second harmonic generation (SHG) [14]. The coherent wave in laser cavities enables one to achieve very precise measurements of intensity patterns. Nevertheless, experiments on the spatial structure of disordered wave functions with conical SHG have never been realized as yet.

In this Letter, we originally develop an intracavity conical SHG scheme to explore the spatial structure of 2D disordered wave functions with weak localization. By using a nonlinear crystal with extended defects, the conical SHG is efficiently produced from a Q -switched laser with intracavity frequency doubling. The near-field patterns of the conical SHG beams evidently represent the wave func-

tions of disordered quantum systems. The statistics of the wave functions are found to be in quantitative agreement with the supersymmetry sigma model [15]. More importantly, the analysis of the intensity correlation for the experimental patterns reveals that the localization effects significantly enhance the magnitude of the long-range correlation.

In the past few years, a new nonlinear crystal family of calcium oxyborates such as $\text{GdCa}_4\text{O}(\text{BO}_3)_3$ (GdCOB) and $\text{YCa}_4\text{O}(\text{BO}_3)_3$ has been developed for efficient SHG and other parametric processes in various fields [16]. The optical properties of the nonlinear crystals are greatly affected by their structural imperfection that is strongly dependent on the material preparation and the growth conditions. Recent investigations [17] revealed that the disordered domain structures may be spontaneously present in nominal GdCOB samples which do not contain any macroscopic defects and cracks. Intriguingly, the presence of an appropriate distribution of disordered domains allows broadband frequency conversion processes without any temperature or angular tuning of the crystal, especially for conical SHG. Here we used a GdCOB crystal with moderate random defect domains to investigate the spatial structure of disordered wave functions. Figure 1 depicts the experimental configuration for the diode-pumped actively Q -switched Nd:YAG laser with intracavity SHG in the GdCOB crystal. The input mirror is a 500 mm radius-of-curvature concave mirror with antireflection coating at 808 nm on the entrance face ($R < 0.2\%$), high-reflection coating at 1064 nm ($R > 99.8\%$) and 532 nm ($R > 99\%$), and high-transmission coating at 808 nm on the other surface ($T > 90\%$). The output coupler is a flat mirror with high-reflection coating at 1064 nm ($R > 99.8\%$) and high-transmission coating at 532 nm ($T > 85\%$). The pump source was an 808 nm fiber-coupled laser diode with a core diameter of 800 μm , a numerical aperture of 0.16, and a maximum output power of 10 W. A focusing lens with 12.5 m focal length and 90% coupling efficiency

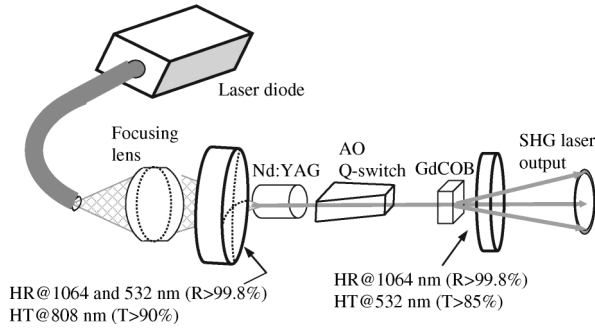


FIG. 1. The experimental configuration for the diode-pumped actively Q -switched Nd:YAG laser with intracavity SHG in the GdCOB crystal.

was used to reimaged the pump beam into the laser crystal. The laser medium was a 0.8-at. % Nd^{3+} :YAG crystal with a length of 10 mm. The GdCOB crystal was cut for type I frequency doubling in the XY planes ($\theta = 90^\circ$, $\phi = 46^\circ$) with a length of 2 mm and a cross section of $3 \text{ mm} \times 3 \text{ mm}$. Both sides of the Nd:YAG and GdCOB crystals were coated for antireflection at 1064 nm ($R < 0.2\%$). The diameters of the laser beams were approximately 580 and $500 \mu\text{m}$ in the Nd:YAG and GdCOB crystals, respectively. The 30 mm-long acousto-optic Q switch (NEOS Technologies) had antireflection coatings at 1064 nm on both faces and was driven at a 27.12 MHz center frequency with 15.0 W of rf power. The laser cavity length was approximately 10 cm.

The pulse repetition rate for the Q -switched pulses was fixed at 20 kHz. The lasing thresholds for the axial and conical SHG beams were nearly the same and approximately 3 W. The typical far-field pattern is shown in Fig. 2(a). At a pump power of 8 W, the output powers of both the axial and conical SHG beams were on the order of 1 mW. The phase-matching condition for the conical SHG in a nonlinear crystal with disordered domain structures is generally written as $\bar{k}_1 + \bar{k}'_1 = \bar{k}_2$, as shown in Fig. 2(b), where \bar{k}_1 is the axial fundamental beam, \bar{k}'_1 is the scattered off-axis fundamental beam, and \bar{k}_2 is the phase-matched

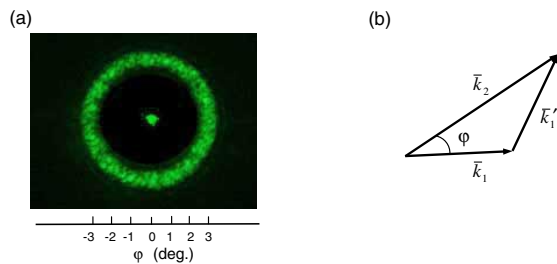


FIG. 2 (color online). (a) The typical far-field pattern of conical SHG. (b) Phase-matching diagram for a conical SHG process in which \bar{k}_1 is the axial fundamental beam, \bar{k}'_1 is the scattered off-axis fundamental beam, and \bar{k}_2 is the phase-matched off-axis SHG beam.

off-axis SHG beam. The cone angle φ is determined by the effective refractive indices. Experimental results revealed that the cone angles of the far-field patterns were almost the same for all the transverse positions of the GdCOB crystal. Even so, the near-field patterns were found to be profoundly related to the topographical characterization of the nonlinear crystal. Figures 3(a)–3(d) show four examples of the near-field wave patterns measured at different transverse positions of the GdCOB crystal. It can be seen that the experimental near-field pattern $|\Psi(\vec{r})|^2$ exhibits a network of quasilinear ridge structures which result from the superposition of monochromatic plane waves with random directions and phases in two dimensions, as discovered by O'Connor, Gehlen, and Heller [18]. Note that the paraxial propagation and the phase-matching condition lead the present conical SHG to be a kind of 2D random scattering process. The quasilinear ridge patterns should be distinguished from the ordinary speckle patterns that are a 2D projection of the light formed by the superposition of monochromatic plane waves with random directions and phases in three dimensions. In other words, the ordinary speckle pattern has a spread in the magnitudes of the projected wave vectors, whereas the quasilinear ridge pattern consists of only a nearly constant transverse wave vector. With the cone angle of the far-field patterns, the present near-field patterns are associated with a superposition of random plane waves with the transverse wave number $K = k_2 \sin\varphi$. To our knowledge, this is the first time that the near-field patterns of conical SHG are used to visualize the spatial structures of the quantum disordered wave functions.

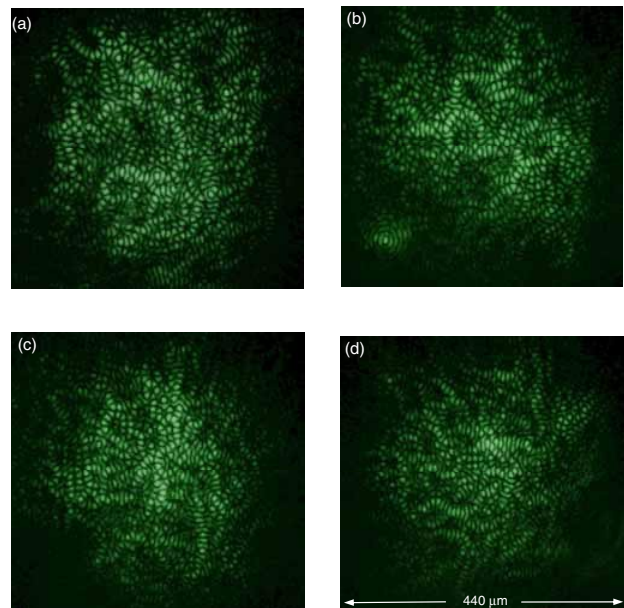


FIG. 3 (color online). Four examples of the near-field wave patterns measured at different transverse positions of the GdCOB crystal.

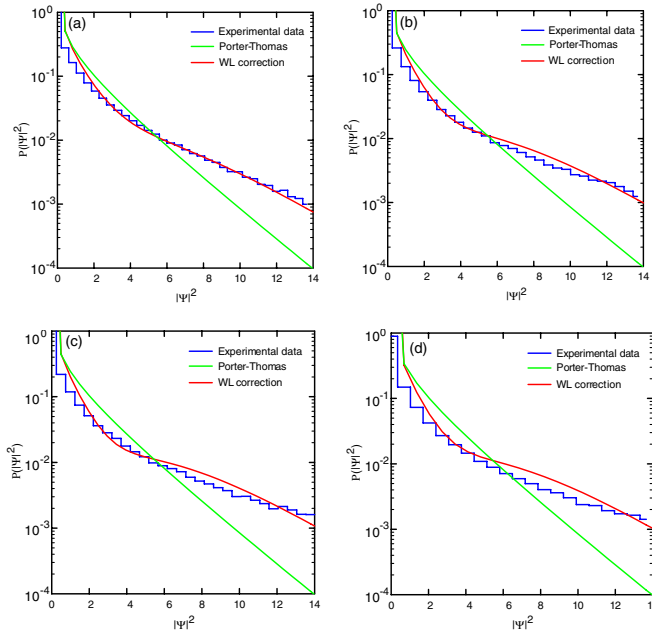


FIG. 4 (color online). (a)–(d) The density probabilities $P(I)$ for the experimental data shown in Figs. 3(a)–3(d), respectively.

The density probability distribution $P(I)$ is extensively used to characterize the localization of the wave function, where $I = |\Psi|^2$. Fyodorov and Mirlin [15] found that the density probability distribution for the normalized disordered wave functions with WL can be expressed as

$$P_{\text{FM}}(I) = P_{\text{PT}}(I) \left[1 + (\text{IPR} - 3) \left(\frac{1}{8} - \frac{1}{4}I + \frac{1}{24}I^2 \right) \right], \quad (1)$$

where $P_{\text{PT}}(I) = \exp(-I/2)/\sqrt{2\pi I}$ is the classic Porter-Thomas (PT) distribution, and $\text{IPR} = \int I^2 d^2r$ is the inverse participation ratio that is closely linked to the degree of localization. The IPR for chaotic systems can be immediately obtained from PT distribution, i.e., $\text{IPR} = \int_0^\infty I^2 P_{\text{PT}}(I) dI = 3.0$, which is a universal value. The IPR is inversely proportional to the volume in which the wave function is confined. As a consequence, the IPR values for disordered systems are generally greater than 3.0, and large IPR values correspond to strongly localized states. We analyzed the experimental near-field patterns to obtain the density probability distribution. Figures 4(a)–4(d) display the density probabilities $P(I)$ for the experimental data shown in Figs. 3(a)–3(d), respectively. The IPR values for the experimental wave patterns in Figs. 3(a)–3(d) are 4.39, 4.91, 5.35, and 5.67, respectively. All four intensity distributions clearly deviate from the PT distribution but show fairly good agreement with the theoretical distribution $P_{\text{FM}}(I)$. The good agreement indicates that the localization effect plays an important role for conical SHG in disordered domain structures.

With the experimental near-field patterns, we calculated the intensity correlation function (ICF) to get further information about the disordered wave function. The ICF for

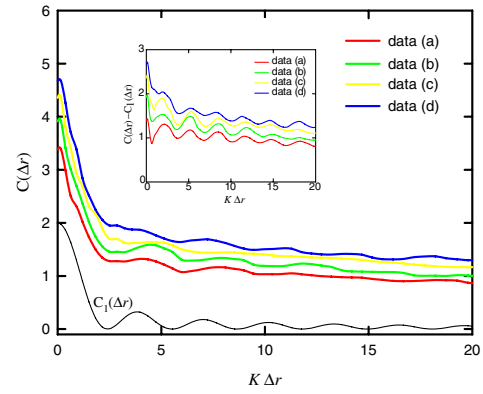


FIG. 5 (color online). The measurement of intensity correlation function $C(\Delta r)$ for the experimental wave patterns shown in Figs. 3(a)–3(d). Inset: The difference $C(\Delta r) - C_1(\Delta r)$.

the normalized wave function is defined as $C(\Delta r) = \langle (I(\bar{r})I(\bar{r}')) - 1 \rangle$, where $\Delta r = |\bar{r} - \bar{r}'|$. The ICF $C(\Delta r)$ for disorder systems is composed of three terms describing short-range $C_1(\Delta r)$, long-range $C_2(\Delta r)$, and infinite-range $C_3(\Delta r)$ [19]. For the 2D orthogonal case, $C_1(\Delta r)$ is given by $2J_0(K\Delta r)$, where J_0 is the Bessel function of zero order. Note that the ICF for chaotic systems is contributed only by $C_1(\Delta r)$. Figure 5 shows the measurement of $C(\Delta r)$ for the experimental wave patterns shown in Figs. 3(a)–3(d). Since $C(\Delta r)$ at $\Delta r = 0$ is equal to the value of $(\text{IPR} - 1)$, the increase of the short-range correlation due to localization is perceptible. A more intriguing feature is that the measured $C(\Delta r)$ are found to approach a constant value for long range. The spatial dependence of the long-range contribution can be examined from the difference $C(\Delta r) - C_1(\Delta r)$, as shown in the inset in Fig. 5. It can be seen that the long-range contribution depends on the degree of localization, and its magnitude increases with increasing the IPR value. The similar long-range correlation has also been observed in the transmission of microwaves [20]. Although numerical study of light in a random medium reveals the analogous phenomenon [21], the present investigation provides the first experimental evidence for the long-range correlation due to transverse localization.

In summary, the spatial structure of 2D disorder wave functions with weak localization has been explored with the conical SHG of a laser in random domain structures. The statistics of the experimental near-field patterns are found to be in quantitative agreement with the theoretical distributions with the correction of weak localization. Furthermore, the analysis of the ICF reveals that the localization effect not only increases the magnitude of the short-range correlation but also introduces a nearly constant value to the long-range correlation. The present result also confirms the possibility of using conical SHG as a diagnostic tool for topographical characterization of crystals in which localization phenomenon occurs naturally.

This work is supported by the National Science Council of Taiwan (Contract No. NSC-94-2112-M-009-034).

*Electronic address: yfchen@cc.netu.edu.tw

- [1] E. Abrahams, P. W. Anderson, D. C. Licciardello, and T. V. Ramakrishnan, Phys. Rev. Lett. **42**, 673 (1979); S. John, Phys. Rev. Lett. **53**, 2169 (1984); P. W. Anderson, Philos. Mag. B **52**, 505 (1985); F. Scheffold and G. Maret, Phys. Rev. Lett. **81**, 5800 (1998).
- [2] P. Sheng, *Introduction to Wave Scattering, Localization, and Mesoscopic Phenomena* (Academic, New York, 1995).
- [3] V. L. Kuzmin and V. P. Romanov, Phys. Usp. **39**, 231 (1996).
- [4] M. C. W. van Rossum and Th. M. Nieuwenhuizen, Rev. Mod. Phys. **71**, 313 (1999).
- [5] B. A. van Tiggelen, Phys. Rev. Lett. **75**, 422 (1995); B. A. van Tiggelen and R. Maynard, in *Wave Propagation in Complex Media*, edited by G. Papanicolaou, IMA Volumes in Mathematics and Its Applications Vol. 96 (Springer, New York, 1998).
- [6] M. P. van Albada and A. Lagendijk, Phys. Rev. Lett. **55**, 2692 (1985); P. E. Wolf and G. Maret, Phys. Rev. Lett. **55**, 2696 (1985).
- [7] D. S. Wiersma, M. P. van Albada, B. A. Van Tiggelen, and A. Lagendijk, Phys. Rev. Lett. **74**, 4193 (1995).
- [8] G. Labeyrie, F. De Tomasi, J. C. Bernard, C. A. Müller, C. Miniatura, and R. Kaiser, Phys. Rev. Lett. **83**, 5266 (1999); Y. Bidel, B. Klappauf, J. C. Bernard, D. Delande, G. Labeyrie, C. Miniatura, D. Wilkowski, and R. Kaiser, Phys. Rev. Lett. **88**, 203902 (2002).
- [9] I. Freund, M. Rosenbluh, R. Berkovitsm, and M. Kaveh, Phys. Rev. Lett. **61**, 1214 (1988).
- [10] D. S. Wiersma, M. P. van Albada, and A. Lagendijk, Phys. Rev. Lett. **75**, 1739 (1995).
- [11] R. Sapienza, S. Mujumdar, C. Cheung, A. G. Yodh, and D. Wiersma, Phys. Rev. Lett. **92**, 033903 (2004); L. V. Kuzmin, V. P. Romanov, and L. A. Zubkov, Phys. Rev. E **54**, 6798 (1996).
- [12] M. Gurioli, F. Bogani, L. Cavigli, H. Gibbs, G. Khitrova, and D. S. Wiersma, Phys. Rev. Lett. **94**, 183901 (2005).
- [13] P. Pradhan and S. Sridhar, Phys. Rev. Lett. **85**, 2360 (2000); A. Kudrolli, V. Kidambi, and S. Sridhar, Phys. Rev. Lett. **75**, 822 (1995); M. Barth, U. Kuhl, and H. J. Stöckmann, Phys. Rev. Lett. **82**, 2026 (1999).
- [14] A. R. Tunyagi, M. Ulex, and K. Betzler, Phys. Rev. Lett. **90**, 243901 (2003); P. Xu, S. H. Ji, S. N. Zhu, X. Q. Yu, J. Sun, H. T. Wang, J. L. He, Y. Y. Zhu, and N. B. Ming, Phys. Rev. Lett. **93**, 133904 (2004).
- [15] Y. V. Fyodorov and A. D. Mirlin, Phys. Rev. B **51**, 13403 (1995); A. D. Mirlin, Phys. Rep. **326**, 259 (2000); V. Prigodin and B. Altshuler, Phys. Rev. Lett. **80**, 1944 (1998); K. B. Efetov, *Supersymmetry in Disorder and Chaos* (Cambridge University Press, Cambridge, England, 1997).
- [16] M. V. Pack, D. J. Armstrong, A. V. Smith, G. Aka, B. Ferrand, and D. Pelenc, J. Opt. Soc. Am. B **22**, 417 (2005).
- [17] M. Lefeld-Sosnowska, E. Olszyńska, A. Pajaczkowska, and A. Klos, J. Cryst. Growth **262**, 388 (2004).
- [18] P. O'Connor, J. Gehlen, and E. J. Heller, Phys. Rev. Lett. **58**, 1296 (1987).
- [19] S. Feng, C. Kane, P. A. Lee, and A. D. Stone, Phys. Rev. Lett. **61**, 834 (1988).
- [20] P. Sebbah, B. Hu, A. Z. Genack, R. Pnini, and B. Shapiro, Phys. Rev. Lett. **88**, 123901 (2002).
- [21] S. H. Chang, A. Taflove, A. Yamilov, A. Burin, and H. Cao, Opt. Lett. **29**, 917 (2004).

Devil's Staircase in Three-Dimensional Coherent Waves Localized on Lissajous Parametric Surfaces

Y. F. Chen,* T. H. Lu, K. W. Su, and K. F. Huang

Department of Electrophysics, National Chiao Tung University, 1001 TA Hsueh Road, Hsinchu 30050, Taiwan

(Received 1 March 2006; published 2 June 2006)

We experimentally demonstrate the significance of the longitudinal-transverse coupling in the mesoscopic regime by using a high- Q laser resonator as an analog experiment. The longitudinal-transverse coupling is found to lead to the three-dimensional (3D) coherent waves that are localized on the parametric surfaces with Lissajous transverse patterns. More strikingly, experimental results reveal that the mode locking of the 3D coherent states forms a nearly complete Devil's staircase with the hierarchical ordering.

DOI: [10.1103/PhysRevLett.96.213902](https://doi.org/10.1103/PhysRevLett.96.213902)

PACS numbers: 42.60.Jf, 03.65.Vf, 05.45.-a, 42.55.Xi

The bunch of energy levels in the quantum spectra has been found to lead to the shell structures in nuclei [1], metallic clusters [2], and quantum dots [3]. More intriguingly, the existence of the bunch level has a deep and far-reaching relation with the emergence of classical features in a mesoscopic quantum system [4]. Recent experimental and theoretical studies have verified that the coherent superposition of degenerate or nearly degenerate quantum states can result in mesoscopic quantum wave functions localized on periodic orbits in the classical counterpart of the given system [5]. Furthermore, experimental results [6] indicated that the mode-locking effects lead to the stationary coherent waves associated with periodic orbits to be robust and structurally stable within a finite range of the perturbation or detuning. Devil's staircases, Arnold tongues, and Farey trees are the hallmark of mode locking and have been found to be ubiquitous in physical, chemical, and biological systems [7]. The phenomenon of mode-locked staircases has been extensively studied in Rayleigh-Bénard experiments [8], charge-density-wave systems [9], Josephson-junction arrays [10], reaction-diffusion systems [11], the modulated external-cavity semiconductor laser [12], the driven vortex lattices with periodic pinning [13], the motion of a charge particle in two waves [14], and the bimode CO₂ laser with a saturable absorber [15]. Nevertheless, experiments on the mode-locked staircase in high-order optical coherent waves have never been realized.

In this Letter we originally show that the longitudinal-transverse coupling leads to the formation of three-dimensional (3D) coherent waves localized on Lissajous parametric surfaces which are formed by the Lissajous curves with the relative phase varying with the longitudinal direction. A high- Q symmetric laser cavity is experimentally employed to verify the existence and prevalence of 3D coherent waves in the mesoscopic regime. More importantly, the detailed experimental measurements indicate that the formation of plentiful 3D coherent waves constructs a nearly complete devil's staircase in the mesoscopic regime. Since the laser cavity may be used as an excellent analog system for the investigation of quantum

systems [6], the present results will be useful for understanding the mesoscopic wave functions.

The resonance frequency for an optical cavity with two spherical mirrors and the mirror distance L is generally expressed as $f(n, m, l) = \Delta f_L [l + (m + n + 1) \times (\Delta f_T / \Delta f_L)]$, where $\Delta f_L = c/2L$ is the longitudinal mode spacing, Δf_T is the transverse mode spacing, l is the longitudinal mode index, and m and n are the transverse mode indices. For an empty symmetric resonator consisting of two identical spherical mirrors with radius of curvature R , the bare ratio between the transverse and the longitudinal mode spacing is given by $\Omega = \Delta f_T / \Delta f_L = (2/\pi) \tan^{-1}(L/2z_R)$, where $z_R = \sqrt{L(2R - L)}/2$. As a consequence, the bare mode-spacing ratio Ω can be changed in the range between 0 and 1 by varying the cavity length L for a given R . Figure 1 shows a portion of the spectrum $f(l, n, m)$ as a function of the bare mode-spacing ratio Ω for the range of $10 \leq l \leq 30$ and $0 \leq (m + n) \leq 20$. It can be seen that the degeneracies and gaps appear at

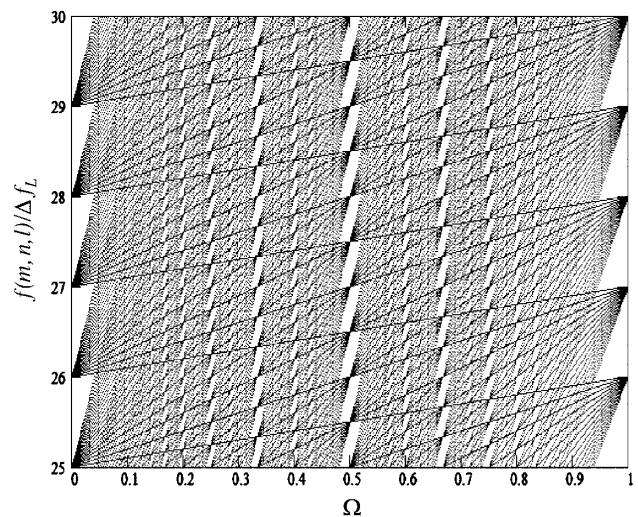


FIG. 1. A portion of the spectrum $f(l, n, m)$ as a function of the bare mode-spacing ratio Ω for the range of $10 \leq l \leq 30$ and $0 \leq (m + n) \leq 20$.

the values of Ω corresponding to the rational numbers P/Q , forming an interesting fractal structure. Degeneracies in the spectra of the quantum systems have been found to play a vital role in the relationship between quantum shell structures and classical periodic orbits, especially in the mesoscopic regime [1–4]. The following

$$\Phi_{m,n,l}^{(\text{HG})}(x, y, z) = \Phi_{m,n}(x, y, z)e^{i(m+n+1)\tan^{-1}(z/z_R)} e^{-i(\pi z/L)[l+(m+n+1)\Omega][(x^2+y^2)/2(z^2+z_R^2)+1]}, \quad (1)$$

where

$$\Phi_{m,n}(x, y, z) = \frac{1}{\sqrt{2^{m+n-1}\pi m!n!}} \frac{1}{w(z)} H_m\left(\frac{\sqrt{2}x}{w(z)}\right) H_n\left(\frac{\sqrt{2}y}{w(z)}\right) \times \exp\left[-\frac{x^2+y^2}{w(z)^2}\right], \quad (2)$$

$w(z) = w_0\sqrt{1+(z/z_R)^2}$, w_0 is the beam radius at the waist, and z_R is the Rayleigh range. When the mode-spacing ratio Ω is locked to a rational number P/Q , the group of the HG modes $\Phi_{m_0+pk, n_0+qk, l_0+sk}^{(\text{HG})}(x, y, z)$, with $k = 0, 1, 2, 3, \dots$, can be found to constitute a family of frequency degenerate states, provided that the given integers (p, q, s) obey the equation $s + (p + q)(P/Q) = 0$. For convenience, the integer s is taken to be negative.

$$\Psi_{m_0, n_0, l_0}^{p, q, s}(x, y, z; \phi_0) = \Psi_{m_0, n_0}^{p, q}(x, y, z; \phi_0) e^{-i(\pi z/L)[l_0+(m_0+n_0+1)P/Q][(x^2+y^2)/2(z^2+z_R^2)+1]}, \quad (3)$$

where

$$\Psi_{m_0, n_0}^{p, q}(x, y, z; \phi_0) = \sum_{k=0}^M e^{ik\phi(z)} \Phi_{m_0+pk, n_0+qk}(x, y, z), \quad (4)$$

and

$$\phi(z) = (q + p)\tan^{-1}(z/z_R) + \phi_0. \quad (5)$$

Equation (3) indicates that the wave pattern of the 3D coherent state $\Psi_{m_0, n_0, l_0}^{p, q, s}(x, y, z; \phi_0)$ is utterly determined by the wave function $\Psi_{m_0, n_0}^{p, q}(x, y, z; \phi_0)$. As seen in Eq. (4), the wave function $\Psi_{m_0, n_0}^{p, q}(x, y, z; \phi_0)$ is a coherent superposition of the modes $\Phi_{m_0+pk, n_0+qk}(x, y, z; \phi_0)$ with the phase factor $\phi(z)$. It is worthwhile to mention that the z dependence of the phase factor $\phi(z)$ arises from the Gouy-phase difference between the HG modes with distinct transverse orders. With the results obtained in the 2D quantum harmonic oscillator [18], the wave function $\Psi_{m_0, n_0}^{p, q}(x, y, z; \phi_0)$ can be manifestly deduced to have the intensity distribution concentrated on the parametric surface:

$$\begin{aligned} x(\vartheta, z) &= \sqrt{m_0 + \frac{M}{2}w(z)} \cos\left[q\vartheta - \frac{\phi(z)}{P}\right]; \\ y(\vartheta, z) &= \sqrt{n_0 + \frac{M}{2}w(z)} \cos(p\vartheta), \end{aligned} \quad (6)$$

where $0 \leq \vartheta \leq 2\pi$ and $-\infty \leq z \leq \infty$. Equation (6) reveals that the parametric surface related to the 3D coherent waves is formed by the Lissajous curves with the relative

analysis will verify that the longitudinal-transverse coupling and the mode-locking effect can lead to the 3D coherent waves to be localized on the parametric surfaces with Lissajous transverse patterns.

The wave functions of the Hermite-Gaussian (HG) modes for a spherical cavity are given by [16]

The equation $s + (p + q)(P/Q) = 0$ indicates that $q + p$ needs to be an integral multiple of Q , i.e., $q + p = KQ$, where $K = 1, 2, 3, \dots$. It has been verified that the coherent superposition of the mode-locked degenerate states manifestly leads to the wave functions to be associated with the classical periodic orbits in the 2D quantum systems [17]. In the present case, the 3D coherent states constructed by the family of $\Phi_{m_0+pk, n_0+qk, l_0+sk}^{(\text{HG})}(x, y, z)$ can be generally given by $\Psi_{m_0, n_0, l_0}^{p, q, s}(x, y, z; \phi_0) = \sum_{k=0}^M e^{ik\phi_0} \Phi_{m_0+pk, n_0+qk, l_0+sk}^{(\text{HG})}(x, y, z)$, where the parameter ϕ_0 is the relative phase between various HG modes at $z = 0$. The relative phase ϕ_0 has been verified to play an important role in the quantum-classical connection [17]. With the expression of Eq. (1), the 3D coherent states can be rewritten as

phase varying with the position z . In other words, the longitudinal-transverse coupling leads to the 3D coherent states to be localized on the Lissajous parametric surfaces. With $q + p = KQ$ and Eq. (5), the total change of the relative phase of the 3D coherent wave from $z = -\infty$ to $z = \infty$ is given by $\phi(\infty) - \phi(-\infty) = (KQ)\pi$. On the other hand, the total change of the relative phase of the 3D coherent wave from one cavity mirror at $z = -L/2$ to another one at $z = L/2$ is given by $\phi(L/2) - \phi(-L/2) = (KP)\pi$, where the mode-locking condition $\tan^{-1}(L/2z_R) = (P/Q)(\pi/2)$ is used. Figure 2 depicts an example for the Lissajous parametric surface described in Eq. (6) for the range from $z = -L/2$ to $z = L/2$ with $(p, q) = (3, 2)$, $P = 2$, and $\phi_0 = 0$. The tomographic transverse patterns are also plotted in the same figure to display the Lissajous feature of the 3D coherent state. Even though the relationship between the 2D quantum coherent states and the Lissajous curves has been previously developed [17], this is the first time that the 3D coherent states are derived to be related to the Lissajous parametric surfaces.

The wave patterns localized on the classical orbits have been realized in the degenerate laser resonator with the ring-shaped pump profile [19]. However, the index order of the laser modes is not high enough to explore the complete devil's staircase phenomenon in the wave-ray correspondence or quantum-classical correspondence. To generate super-high-order laser modes, here we use the off-axis focused pumping scheme to excite a very high gain crystal in a symmetric cavity with extremely low losses ($<0.5\%$),

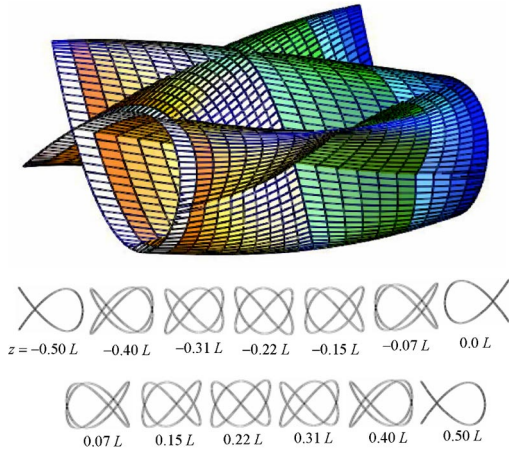


FIG. 2 (color online). Upper: An example for the Lissajous parametric surface described in Eq. (6) for the range from $z = -L/2$ to $z = L/2$ with $(p, q) = (3, 2)$, $P = 2$, and $\phi_0 = 0$. Bottom: The tomographic transverse patterns along the longitudinal axis.

as depicted in Fig. 3. The laser medium was a *a*-cut 2.0-at. % Nd³⁺:YVO₄ crystal with a length of 1 mm. Both sides of the Nd:YVO₄ crystal was coated for antireflection at 1064 nm (reflection <0.1%). The radius of curvature of the cavity mirrors are $R = 10$ mm and their reflectivity is 99.8% at 1064 nm. The pump source was an 809 nm fiber-coupled laser diode with a core diameter of 100 μm , a numerical aperture of 0.16, and a maximum output power of 1 W. A focusing lens with 20 mm focal length and 90% coupling efficiency was used to reimage the pump beam into the laser crystal. The pump radius was estimated to be 25 μm . A microscope objective lens mounted on a translation stage was used to reimage the tomographic transverse patterns inside the cavity onto a CCD camera. To measure the far-field pattern, the output beam was directly projected on a paper screen at a distance of ~ 50 cm from the rear cavity mirror and the scattered light was captured by a digital camera.

At a pump power of 1 W, the emission powers were generally found to be on the order of 0.5 mW. The low

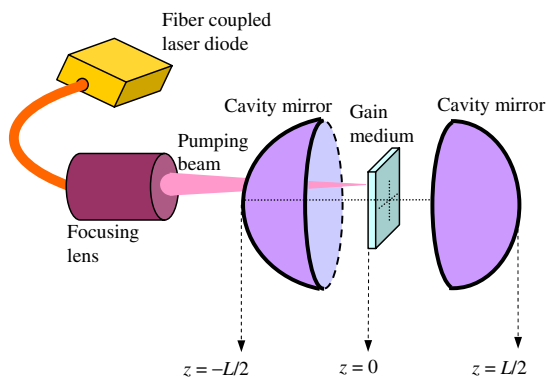


FIG. 3 (color online). Experimental setup for the generation of 3D coherent waves in a diode-pumped microchip laser with off-axis pumping scheme in a symmetric spherical resonator.

emission powers indicate the cavity Q value to be rather high. The pump positions on the gain medium were controlled to excite the laser modes with the transverse orders n and m in the range of 100 to 500. Experimental results revealed that the far-field transverse patterns were not the familiar HG modes but were almost the coherent waves concentrated on various Lissajous figures for all cavity lengths. Furthermore, the tomographic transverse patterns inside the cavity evidently displayed the revolution of the Lissajous curve along the longitudinal axis to form a Lissajous parametric surface. Figure 4 shows the experimental tomographic transverse patterns observed at $\Omega \approx 0.422$. The experimental tomographic transverse patterns are found to be in good agreement with the feature that the 3D coherent states are well localized on the Lissajous parametric surfaces. Furthermore, the experimental patterns shown in Fig. 4 for $-0.15L \leq z \leq 0.15L$ have a noticeable bright spot that represents the location of the pump beam. It can be seen that the pump intensity has a great overlap with the lasing mode distribution. Since the cavity mode possessing the biggest overlap with the gain region will dominate the laser emission, distinct 3D coherent waves can be precisely generated by manipulating the pump position.

Continuously adjusting the bare mode-spacing ratio Ω , the far-field transverse patterns were found to change from one mode-locked Lissajous wave to another in discrete steps. According to the above-mentioned analysis, the appearance of the Lissajous waves signifies the mode-spacing ratios to be locked to rational numbers P/Q . The analytical representation of the 3D coherent states enables us to identify the mode-locked ratios P/Q precisely from the information of the revolution numbers of the Lissajous wave patterns inside and outside the cavity. Based on thorough experiments, we found that each mode-locked ratio P/Q is composed of numerous 3D coherent waves localized on various Lissajous parametric surfaces with

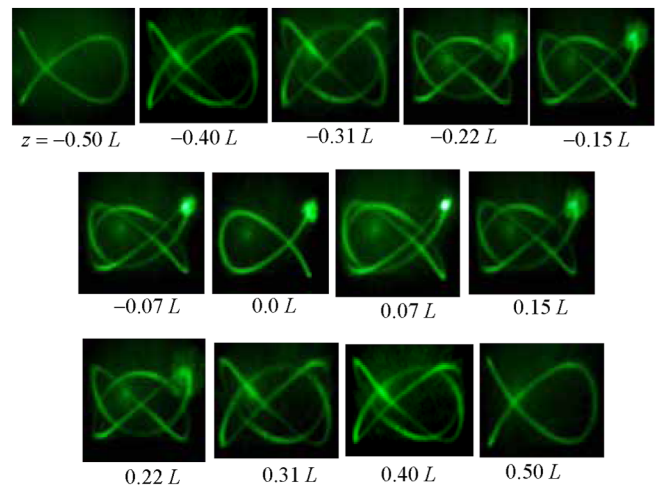


FIG. 4 (color online). Experimental tomographic transverse patterns inside the cavity observed at $\Omega \approx 0.422$.

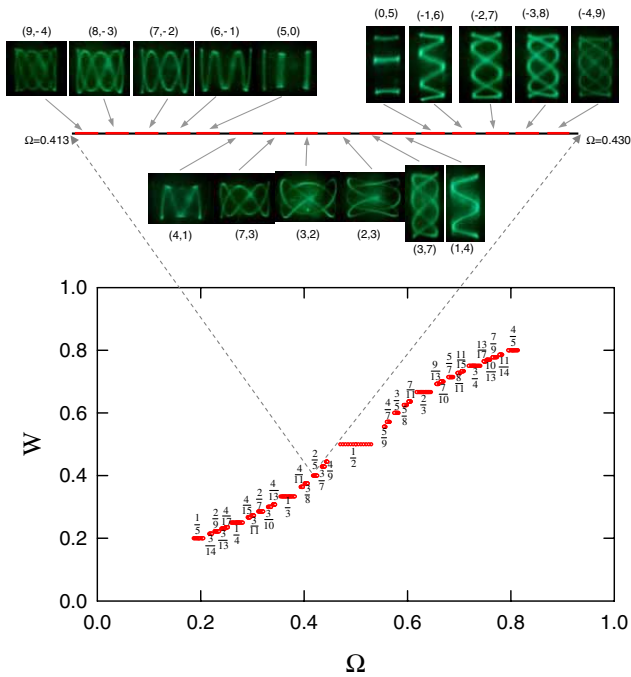


FIG. 5 (color online). Bottom: Experimental mode-locked ratio P/Q as a function of the bare mode-spacing ratio Ω . Upper: Experimental far-field patterns observed in the mode-locked plateau with $P/Q = 2/5$.

indices $q + p$ to be an integral multiple of Q . On the whole, more than 560 different 3D coherent states have been obtained. The locking range of each coherent state was found to be $\Delta\Omega \approx (1.5 \pm 0.2) \times 10^{-3}$ on average. More noticeably, the experimental mode-locked ratios P/Q were found to form a fairly complete devil's staircase, as shown in Fig. 5. Figure 5 also demonstrates the experimental far-field patterns observed in the mode-locked plateau with $P/Q = 2/5$. The absolute values of the indices p and q were first determined from the feature of the Lissajous transverse pattern and their signs were determined from the equation of $q + p = KQ$, where the factor K could be found from the total change of the relative phase of the Lissajous transverse pattern inside the cavity and the indices Q and P were confirmed with the cavity length. It is worthwhile to mention that p and q can have the opposite sign, as long as $q + p$ is an integral multiple of Q . On the other hand, the locking regimes for the coherent states with the indices (p, q) and (q, p) are split due to the anisotropic properties of the gain medium [6]. As the transverse order (m_0, n_0) of the coherent mode is increased, the number of mode-locked plateaus increases, suggesting that all rational steps will be seen in an infinite order system.

In summary, the longitudinal-transverse coupling has been verified to cause the formation of 3D coherent waves with localization on parametric surfaces in the mesoscopic regime. The theoretical analysis reveals that the tomographic transverse patterns of the 3D coherent waves exhibit to be well localized on the Lissajous parametric

surfaces. A high- Q symmetric laser cavity with the off-axis pumping scheme has been utilized to realize the experiment. Experimental results reveal that the mode locking of the 3D coherent states forms a nearly complete devil's staircase with the hierarchical ordering. Our studies may provide some useful insights into the nature of the mesoscopic wave functions.

This work is supported by the National Science Council of Taiwan (Contract No. NSC-94-2112-M-009-034).

*To whom correspondence should be address.

Electronic address: yfchen@cc.nctu.edu.tw

- [1] A. Bohr and B.R. Mottelson, *Nuclear Structure* (Benjamin, New York, 1975), Vol. 2.
- [2] M. Brack, *Rev. Mod. Phys.* **65**, 677 (1993).
- [3] S.M. Reimann and M. Manninen, *Rev. Mod. Phys.* **74**, 1283 (2002).
- [4] R.K. Bhaduri, S. Li, K. Tanaka, and J.C. Waddington, *J. Phys. A* **27**, L553 (1994); B.L. Johnson and G. Kirczenow, *Europhys. Lett.* **51**, 367 (2000).
- [5] I.V. Zozoulenko and K.F. Berggren, *Phys. Rev. B* **56**, 6931 (1997); R. Narevich, R.E. Prange, and O. Zaitsev, *Phys. Rev. E* **62**, 2046 (2000).
- [6] K.F. Huang, Y.F. Chen, H.C. Lai, and Y.P. Lan, *Phys. Rev. Lett.* **89**, 224102 (2002); Y.F. Chen and Y.P. Lan, *Phys. Rev. A* **66**, 053812 (2002); Y.F. Chen, K.F. Huang, H.C. Lai, and Y.P. Lan, *Phys. Rev. E* **68**, 026210 (2003).
- [7] H.G. Shuster, *Deterministic Chaos* (VCH Verlag, Weinheim, 1988); E. Ott, *Chaos in Dynamic System* (Cambridge University Press, Cambridge, 1993); A. Pikovsky, M. Rosenblum, and J. Kurths, *Synchronization* (Cambridge University Press, Cambridge, 2001).
- [8] J. Stavans, F. Heslot, and A. Libchaber, *Phys. Rev. Lett.* **55**, 596 (1985).
- [9] S.E. Brown, G. Mozurkewich, and G. Grüner, *Phys. Rev. Lett.* **52**, 2277 (1984); A.A. Middleton, O. Biham, P.B. Littlewood, and P. Sibani, *Phys. Rev. Lett.* **68**, 1586 (1992).
- [10] P. Alstrøm and M.T. Levinsen, *Phys. Rev. B* **31**, 2753 (1985); E. Orignac and T. Giamarchi, *Phys. Rev. B* **64**, 144515 (2001).
- [11] A.L. Lin, M. Bertram, K. Martinez, and H.L. Swinney, *Phys. Rev. Lett.* **84**, 4240 (2000).
- [12] D. Baums, W. Elsässer, and E.O. Göbel, *Phys. Rev. Lett.* **63**, 155 (1989).
- [13] C. Reichardt and F. Nori, *Phys. Rev. Lett.* **82**, 414 (1999).
- [14] A. Macor, F. Doveil, and Y. Elskens, *Phys. Rev. Lett.* **95**, 264102 (2005).
- [15] D. Hennequin, D. Dangoisse, and P. Glorieux, *Phys. Rev. A* **42**, 6966 (1990).
- [16] A.E. Siegman, *Lasers* (University Science Books, Mill Valley, CA, 1986).
- [17] Y.F. Chen, K.F. Huang, and Y.P. Lan, *Phys. Rev. E* **66**, 046215 (2002); **66**, 066210 (2002); Y.F. Chen and K.F. Huang, *Phys. Rev. E* **68**, 066207 (2003).
- [18] Y.F. Chen and K.F. Huang, *J. Phys. A* **36**, 7751 (2003).
- [19] Y.F. Chen, Y.P. Lan, and K.F. Huang, *Phys. Rev. A* **68**, 043803 (2003).

High-peak-power AlGaInAs quantum-well 1.3- μm laser pumped by a diode-pumped actively Q-switched solid-state laser

K. W. Su, S. C. Huang, A. Li, S. C. Liu, Y. F. Chen, and K. F. Huang

Department of Electrophysics, National Chiao Tung University, Hsinchu, Taiwan

Received March 21, 2006; revised April 28, 2006; accepted April 28, 2006; posted May 1, 2006 (Doc. ID 69172)

We report a room-temperature high-peak-power AlGaInAs 1.36 μm TEM₀₀ laser pumped by a diode-pumped actively Q-switched Nd:YAG 1.06 μm laser. With an average pump power of 1.0 W, an average output power of 140 mW was obtained at a pulse repetition rate of 10 kHz. With a peak pump power of 8.3 kW, the highest peak output power was 1.5 kW at a pulse repetition rate of 5 kHz. © 2006 Optical Society of America

OCIS codes: 140.5960, 140.5560, 140.3380, 250.7270.

High-peak-power all-solid-state laser sources in the 1.3–1.6 μm spectral region are of particular interest in remote sensing, eye-safe optical ranging, fiber sensing, and communication.^{1–4} Diode-pumped solid-state lasers (DPSSLs) that have the advantages of relatively compact size, high power, excellent beam quality, long lifetime, and low heat production have been widely used for various applications, including industry, pure science, medical diagnostics, and entertainment.⁵ Nevertheless, the spectral range of diode-pumped solid-state laser systems is limited by the properties of existing doped crystals and glasses. Recently, the optically pumped vertical-external-cavity surface-emitting semiconductor lasers (VECSELs) have been proposed as a novel class of all-solid-state lasers with potential spectral coverage from the near ultraviolet to the midinfrared.^{6,7}

Typically, a VECSEL device consists of a highly reflecting distributed Bragg reflector (DBR) and a resonant periodic gain structure that comprises a series of barriers to provide the pump absorption, quantum wells (QWs) to provide gain, and layers to prevent oxidation. Although InP-based material could offer a gain region with a smaller lattice mismatch for 1.3 μm wavelengths, the small contrast of refractive indices hinders the performance of the DBRs. As a consequence, until now the InP-based material has never been used as a VECSEL device at 1.3 μm . To reach a wavelength near 1.3 μm , GaInNAs/GaAs QWs have been developed as a gain medium⁸ and a 0.6 W cw output power has been demonstrated.⁹ Even so, there has been no experimental demonstration of room-temperature high-peak-power 1.3 μm laser sources with semiconductor QWs as gain media in an external cavity.

In this Letter we report, for the first time to our knowledge, a room-temperature high-peak-power nanosecond semiconductor QW laser at 1.36 μm , using a diode-pumped actively Q-switched Nd:YAG 1.06 μm laser as a pump source. The gain medium was composed of an AlGaInAs QW/barrier structure grown on an Fe-doped InP transparent substrate. Note that the conventional S-doped InP substrate has significant absorption in the 1.0–2.0 μm spectral

region. Since the Fe-doped InP substrate is transparent at the lasing wavelength, the function of the DBRs in the VECSEL device can be replaced by an external mirror. With an average pump power of 1.0 W, an average output power of 140 mW at a pulse repetition rate of 10 kHz was obtained. The peak output power was up to 1.5 kW at a pulse repetition rate of 5 kHz.

The present gain medium is an AlGaInAs QW/barrier structure grown on an Fe-doped InP substrate by metalorganic chemical-vapor deposition. It is worthwhile to mention that the AlGaInAs material system has a larger conduction band offset than the most widely used InGaAsP system.^{10–13} This larger conduction band offset has been confirmed to yield better electron confinement in the conduction band and higher temperature stability. The AlGaInAs material has been used as a surface-emitting optical amplifier pumped by a laser diode.¹⁴ However, until now there has been no experimental realization involving the VECSEL with AlGaInAs. Here the gain region consists of 30 groups of two QWs with the luminescence wavelength around 1365 nm, spaced at half-wavelength intervals by AlGaInAs barrier layers with the bandgap wavelength around 1070 nm. The barrier layers are used not only to absorb the pump light but also to locate the QW groups in the antinodes of the optical field standing wave. An InP window layer was deposited on the gain structure to avoid surface recombination and oxidation. The back side of the substrate was mechanically polished after growth. Both sides of the gain chip were antireflection (AR) coated to reduce backreflections and coupled-cavity effects. The total residual reflectivity of the AR-coated sample is approximately 5%. Figure 1 shows the transmittance spectrum at room temperature for the AR-coated AlGaInAs/InP gain chip. It can be seen that the strong absorption of the barrier layers leads to low transmittance near 1070 nm. The total absorption efficiency of the barrier layers at 1064 nm was found to be approximately 95%. On the other hand, an abrupt change in transmittance near 1365 nm comes from the absorption of the AlGaInAs QWs. The room-temperature spontaneous-emission

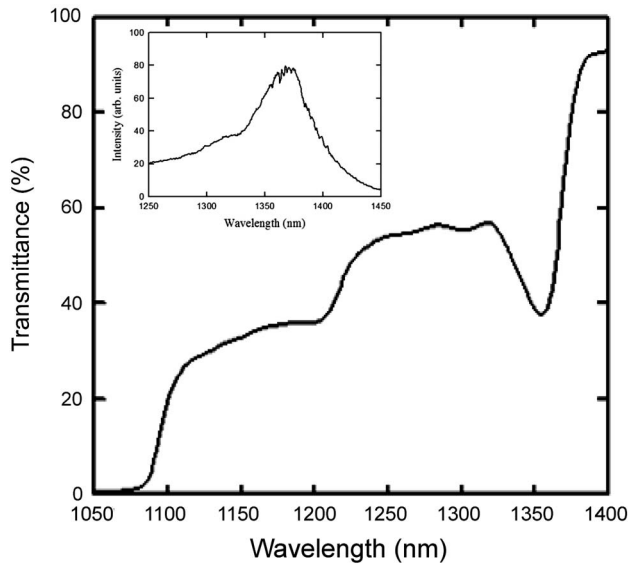


Fig. 1. Transmittance spectrum at room temperature for the AR-coated AlGaInAs/InP gain chip. Inset, room-temperature spontaneous-emission spectrum, obtained by pulse excitation at 1064 nm.

spectrum, obtained by pulse excitation at 1064 nm, is shown in the inset of Fig. 1. As expected, the emission is quite broad, with a peak around 1365 nm, and has a long tail extending to shorter wavelengths.

Figure 2 shows the experimental configuration of the room-temperature high-peak-power AlGaInAs QWs laser at 1365 nm. The pump source is a diode-pumped acousto-optically Q-switched Nd:YAG 1064 nm laser to provide 15-50 ns pulses at repetition rates between 5 and 50 kHz. The pump spot diameter is controlled to be $380 \pm 20 \mu\text{m}$ for efficient spatial overlap with the fundamental transverse mode. The gain chip was mounted on a copper heat sink, but no active cooling was applied. The laser resonator is a concave–plano cavity. The input mirror was a 500 mm radius-of-curvature concave mirror with AR coating on the entrance face at 1064 nm ($R < 0.2\%$), high-reflection coating at 1365 nm ($R > 99.8\%$), and high-transmission coating at 1064 nm on the other surface ($T > 90\%$). The reflectivity of the flat output coupler is 94% at 1365 nm. The overall laser cavity length is approximately 10 mm.

Figure 3 shows the performance of the optically pumped AlGaInAs laser at pump repetition rates of 5, 10, and 50 kHz. The pump pulse widths for repetition rates of 5, 10, and 50 kHz are approximately 15, 25, and 50 ns, respectively. The cavity decay time is ~ 0.11 ns. The beam quality factor was determined by a Gaussian fit to the laser beam waist, and the divergence angle and was found to be less than 1.5. At a repetition of 10 kHz, the average output power could be up to 140 mW; the output power saturation beyond the average pump power of 1.0 W was due to the thermally induced gain degradation. At a repetition of 5 kHz, the absorption efficiency of the gain chip for the pump higher than 0.7 W was found to be significantly reduced because of pump-saturation effects of the barrier layers. As a conse-

quence, maximum average output power at a repetition rate of 5 kHz was saturated at around 90 mW. With the experimental data on a pump pulse energy of $140 \mu\text{J}$, a pump pulse width of 15 ns, and a pump area of 0.113 mm^2 , the pump saturation intensity was estimated to be 8.2 MW/cm^2 . This value was 2–3 orders of magnitude higher than conventional solid-state laser crystals because of its shorter fluorescence decay time.¹⁵ However, the lower conversion efficiency at the 50 kHz repetition rate might be due to the longer pump pulse duration that enhanced the local heating effect. The maximum output power at 50 kHz was found to be nearly the same as the result obtained at 10 kHz. In other words, management of the thermal effects is necessary to scale up the average output power.

Figure 4 shows a typical oscilloscope trace of a train of output and pump pulses and expanded

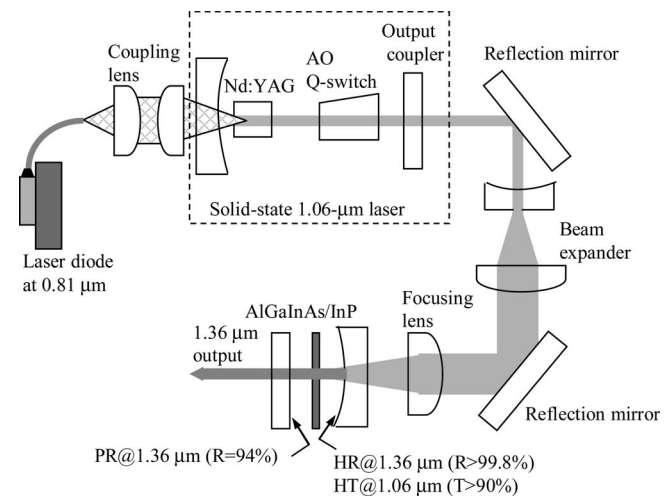


Fig. 2. Experimental configuration of the room-temperature optically pumped AlGaInAs laser at 1365 nm.

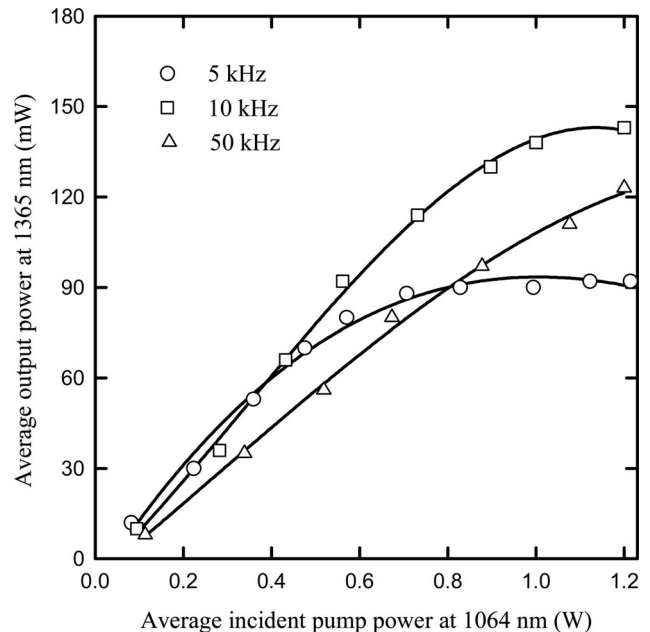


Fig. 3. Experimental results for the optically pumped AlGaInAs laser at pump repetition rates of 5, 10, and 50 kHz.

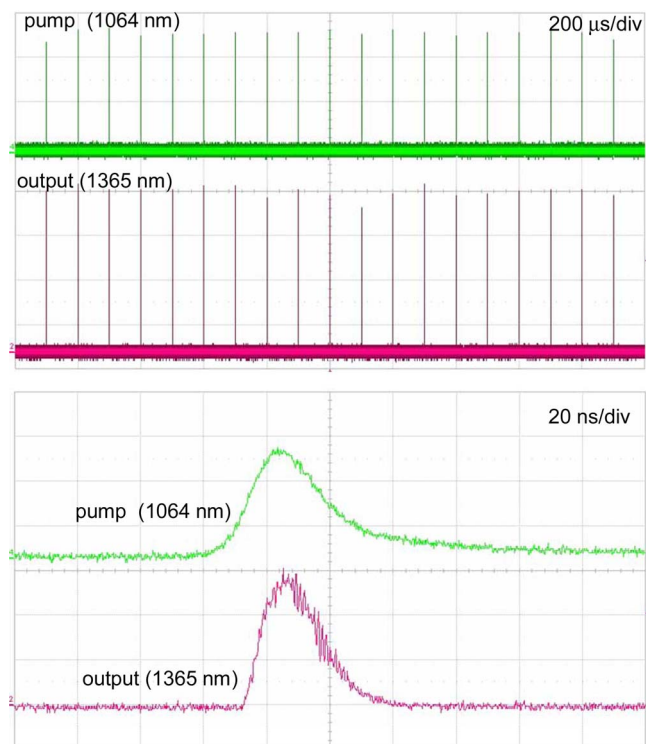


Fig. 4. (Color online) (a) Typical oscilloscope trace of a train of pump and output pulses and (b) expanded shapes of a single pulse.

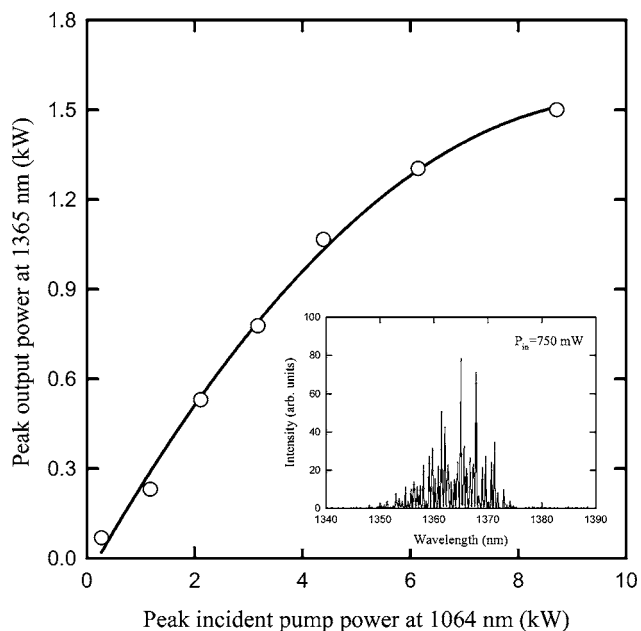


Fig. 5. Experimental results for the peak output power as a function of peak pump power. Inset, typical lasing spectrum obtained with 750 mW of average pump power at a repetition rate of 10 kHz.

shapes of a single pulses. It can be seen that the output pulses tracked the pump pulses for each pumping case. Figure 5 shows the peak output power as a function of peak pump power. The peak output power was up to 1.5 kW at a peak pump power of 8.3 kW, and the slope efficiency was approximately 18%.

The typical lasing spectrum shown in the inset of Fig. 5 was obtained with 750 mW of average pump

power at a repetition rate of 10 kHz. The lasing spectrum was composed of dense longitudinal modes, and its bandwidth was up to 20 nm for an average pump power greater than 200 mW. The wide spectral range indicates the potential for achieving ultrashort pulses in mode-locked operation.

In summary, an AlGaInAs QW/barrier structure grown on an Fe-doped InP transparent substrate was developed to be a gain medium in a room-temperature high-peak-power nanosecond laser at 1365 nm. Using an actively Q-switched 1064 nm laser to pump the gain chip, an average output power of 140 mW was obtained at a pulse repetition rate of 10 kHz and an average pump power of 1.0 W. At a pulse repetition rate of 5 kHz, the peak output power was found to be up to 1.5 kW at a peak pump power of 8.3 kW.

The authors gratefully acknowledge various AlGaInAs/InP gain chips from TrueLight Corporation. The authors also thank the National Science Council for their financial support of this research under contract NSC-93-2112-M-009-034. Address correspondence to Y.-F. Chen, yfchen@cc.nctu.edu.tw.

References

1. A. S. Grabtchikov, A. N. Kuzmin, V. A. Lisinetskii, V. A. Orlovich, A. A. Demidovich, K. V. Yumashev, N. V. Kuleshov, H. J. Eichler, and M. V. Danailov, *Opt. Mater.* **16**, 349 (2001).
2. R. Fluck, R. Häring, R. Paschotta, R. Gini, H. Melchior, and U. Keller, *Appl. Phys. Lett.* **72**, 3273 (1998).
3. R. D. Stultz, V. Leyva, and K. Spariosu, *Appl. Phys. Lett.* **87**, 241118 (2005).
4. V. G. Savitski, N. N. Posnov, P. V. Prokoshin, A. M. Malyarevich, K. V. Yumashev, M. I. Demchuk, and A. A. Lipovski, *Appl. Phys. B* **75**, 841 (2002).
5. D. L. Spies, *Appl. Phys. Lett.* **47**, 74 (1985).
6. M. Kuznetsov, F. Hakimi, R. Sprague, and A. Mooradian, *IEEE J. Sel. Topics Quantum Electron.* **5**, 561 (1999).
7. A. C. Tropper, H. D. Foreman, A. Garnache, K. G. Wilcox, and S. H. Hoogland, *J. Phys. D* **39**, R74 (2004).
8. M. Kondow, K. Uomi, A. Niwa, T. Kitatani, S. Watahiki, and Y. Yazawa, *Jpn. J. Appl. Phys. Part 1* **35**, 1273 (1996).
9. J. M. Hopkins, S. A. Smith, C. W. Jeon, H. D. Sun, D. Burns, S. Calvez, M. D. Dawson, T. Jouhti, and M. Pessa, *Electron. Lett.* **4**, 30 (2004).
10. C. E. Zah, R. Bhat, B. N. Pathak, F. Favire, W. Lin, M. C. Wang, N. C. Andreadakis, D. M. Hwang, M. A. Koza, T. P. Lee, Z. Wang, D. Darby, D. Flanders, and J. J. Hsieh, *IEEE J. Quantum Electron.* **30**, 511 (1994).
11. J. Minch, S. H. Park, T. Keating, and S. L. Chuang, *IEEE J. Quantum Electron.* **35**, 771 (1999).
12. S. R. Selmic, T. M. Chou, J. P. Sih, J. B. Kirk, A. Mantie, J. K. Butler, D. Bour, and G. A. Evans, *IEEE J. Sel. Top. Quantum Electron.* **7**, 340 (2001).
13. N. Nishiyama, C. Caneau, B. Hall, G. Guryanov, M. H. Hu, X. S. Liu, M.-J. Li, R. Bhat, and C. E. Zah, *IEEE J. Sel. Top. Quantum Electron.* **11**, 990 (2005).
14. O. Hanaizumi, K. T. Jeong, S. Y. Kashiwada, I. Syuaib, K. Kawase, and S. Kawakami, *Opt. Lett.* **21**, 269 (1996).
15. F. Sanchez, M. Brunel, and K. Ait-Ameur, *J. Opt. Soc. Am. B* **15**, 2390 (1998).

A. LI
S.C. LIU
K.W. SU
Y.L. LIAO
S.C. HUANG
Y.F. CHEN[✉]
K.F. HUANG

InGaAsP quantum-wells saturable absorber for diode-pumped passively *Q*-switched 1.3- μm lasers

Department of Electrophysics, National Chiao Tung University, 1001 TA Hsueh Road, Hsinchu, 30050 Taiwan

Received: 15 January 2006/Revised version: 24 March 2006
Published online: 20 May 2006 • © Springer-Verlag 2006

ABSTRACT We demonstrate the first use of InGaAsP quantum wells as a saturable absorber in the *Q*-switching of a diode-pumped Nd-doped 1.3 μm laser. The barrier layers of the InGaAsP quantum-well device are designed to be a strong absorber for the suppression of the transition channel at 1.06 μm . With an incident pump power of 1.8 W, an average output power of 160 mW with a *Q*-switched pulse width of 19 ns at a pulse repetition rate of 38 kHz was obtained.

PACS 42.60.Gd; 42.55.Xi; 42.65.Re

1 Introduction

Compact, rugged, all-solid-state *Q*-switched lasers at 1.3 μm wavelength are of practical importance for numerous applications such as medical diagnostics, fiber sensing, distance measurements, intracavity optical parametric oscillators, and intracavity Raman conversion. Compared with active *Q*-switching, passive *Q*-switching is compact, and has simplicity in operation because it requires no electro-optic or acoustic-optic devices. Nowadays, the saturable absorbers for 1.3 μm lasers comprise V^{3+} :YAG [1–3], Co^{2+} : MgAl_2O_4 [4], Co^{2+} :MAS [5], PbS-doped glasses [6], and semiconductor saturable absorber mirrors (SESAMs) [7–10]. The material for SESAMs at 1.3 μm wavelength include InGaAs/GaAs quantum wells (QWs) [7], GaInNAs/GaAs QWs [8, 9], InAs/GaAs quantum dots (QDs) [10], and InGaAsP/InP bulk layers [11]. InGaAs QWs for 1.3 μm SESAMs have the drawback of large insertion losses because the high indium concentration gives rise to significantly strained layers on the GaAs distributed Bragg reflectors (DBRs). Even though InAs QDs for 1.3 μm SESAMs have lower nonsaturable losses, it is difficult to scale up the amount of the maximum reflectivity change between low and high intensities [10]. On the contrary, the lattice-matched InGaAsP-based SESAMs could offer saturable absorbers with larger modulation depths and longer recovery lifetimes for passive *Q*-switching operation at 1.3 μm . However, the overall performance of the DBRs on InP substrates are hindered by the disadvantage

of a small contrast between refractive indices. Even though AlGaAsSb/InP has been demonstrated to be lattice-matched DBRs at 1.55 μm [12], it is more difficult for the 1.3 μm wavelength because the choice of DBR becomes tighter. Nevertheless, the DBRs are merely an optional structure for the cavity design of the passive *Q*-switched lasers. Without the use of DBRs, the semiconductor saturable absorber (SESA) has to be grown on a transparent substrate. The Fe-doped InP material is a particularly useful substrate to grow the SESA for passively *Q*-switched Nd-doped or Yb-doped solid-state lasers [13], since it is transparent at the lasing spectral region. More importantly, the double-pass configuration with an external output coupler is beneficial to the flexibility of the cavity design and the optimization of the output coupler.

Here we present an InGaAsP QW/barrier structure grown on an Fe-doped InP substrate to be a semiconductor saturable absorber (SESA) for a Nd:YVO₄ 1.34 μm laser. The novelty of this work lies in the present semiconductor device serving simultaneously as a saturable absorber for 1.34 μm lasers and a strong absorber for the suppression of the transition channel at 1.06 μm . With an incident pump power of 1.8 W, an average output power of 160 mW with a peak power of 220 W at a pulse repetition rate of 38 kHz was obtained.

2 Experimental

This InGaAsP QW/barrier structure was monolithically grown on an Fe-doped InP substrate by metalorganic chemical-vapor deposition. The saturable-absorber region consists of fifteen InGaAsP QWs with the band-gap wavelength around 1.34 μm , spaced at quarter-wavelength intervals by InGaAsP barrier layers with the band-gap wavelength around 1.06 μm . In other words, the composition of the barrier layers was designed to have a strong absorbance at 1.06 μm . With this SESA, the cavity mirrors require no special dichroic coatings to suppress the strongest transition channel at 1.06 μm . The backside of the substrate was mechanically polished after growth. Both sides of the SESA were antireflection (AR) coated to reduce back reflections and couple-cavity effects. Figure 1 shows the transmittance spectrum at room temperature for the AR-coated InGaAsP/InP saturable absorber. The transmittance of the AR-coated Fe-doped InP substrate is also shown for comparison. It can be seen that the strong absorption of the barrier layers leads to

✉ Fax: +886-35-725230, E-mail: yfchen@cc.nctu.edu.tw

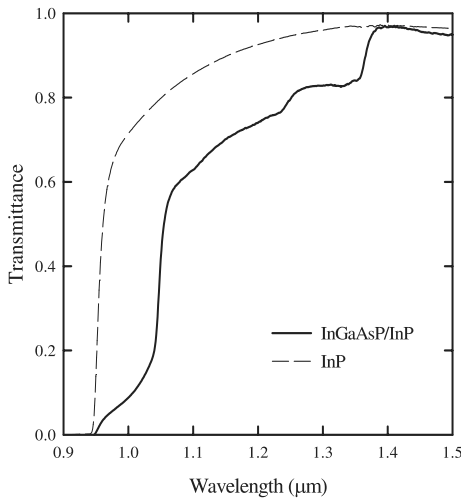


FIGURE 1 Solid line: the transmittance spectrum at room temperature for the AR-coated InGaAsP/InP saturable absorber. Dashed line: the transmittance of the AR-coated Fe-doped InP substrate

a low transmittance near $1.06 \mu\text{m}$. The initial transmissions at $1.06 \mu\text{m}$ and $1.34 \mu\text{m}$ are 0.54 and 0.82, respectively. As a consequence, the gain suppression of $1.06 \mu\text{m}$ is approximately 3 dB compared to that of $1.34 \mu\text{m}$ for a double pass. On the other hand, an abrupt change in the transmittance near $1.36 \mu\text{m}$ comes from the absorption of the InGaAsP QWs. The modulation depth of the SESA device is experimentally estimated to be approximately 10% in a single pass, so in total 20% for a cavity roundtrip. From the numerical simulations of the SESA design, the saturation fluence is estimated to be in the range of $10 \mu\text{J}/\text{cm}^2$. The relaxation time and optical damage threshold of the SESA are approximately $10 \sim 20 \text{ ns}$ and $200 \sim 300 \text{ MW}/\text{cm}^2$, respectively.

Figure 2 depicts the experimental configuration for the passively Q -switched $1.34 \mu\text{m}$ Nd:YVO₄ laser by use of InGaAsP/InP QWs as a saturable absorber. The active medium was a 0.5 at. % Nd³⁺, 6 mm long Nd:YVO₄ crystal. Both sides of the laser crystal were coated for antireflection at $1.34 \mu\text{m}$ ($R < 0.2\%$). The pump source was a 2.0 W 808 nm fiber-coupled laser diode with a core diameter of $200 \mu\text{m}$ and

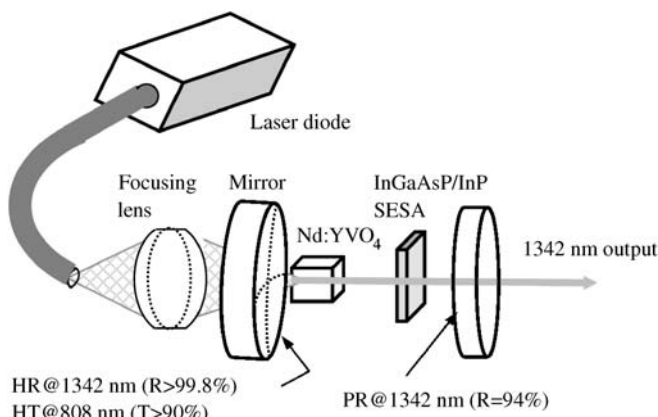


FIGURE 2 Experimental configuration for the passively Q -switched $1.34 \mu\text{m}$ Nd:YVO₄ laser by use of InGaAsP/InP QWs as a saturable absorber

a numerical aperture of 0.16. A focusing lens with a 16.5 mm focal length and 90% coupling efficiency was used to re-image the pump beam into the laser crystal. The pump spot radius was around $100 \mu\text{m}$. The input mirror was a 500 mm radius-of-curvature concave mirror with antireflection coating at the diode wavelength on the entrance face ($R < 0.2\%$), high-reflection coating at the lasing wavelength ($R > 99.8\%$) and a high-transmission coating at the diode wavelength on the other surface ($T > 90\%$). Note that the laser crystal was placed near the input mirror ($< 1 \text{ mm}$) for the spatial overlap of the transverse mode structure and radial pump power distribution. The reflectivity of the output coupler is 94% at 1342 nm . The overall Nd:YVO₄ laser cavity length was approximately 20 mm. The cavity losses introduced by the pump mirror and output coupler are approximately 0.48 and 0.065 for wavelengths at 1.06 and $1.34 \mu\text{m}$. The total nonsaturable loss introduced by the SESA is approximately 0.05. The nonsaturable loss of the SESA mainly comes from electron overflow. The nonsaturable loss may be reduced by the QW materials with relatively large conduction band offsets. Without the SESA in the cavity, cw operation at $1.34 \mu\text{m}$ could be achieved with the cavity losses introduced by the resonator mirrors. However, the gain suppression at $1.06 \mu\text{m}$ needed to be larger for the Q -switching operation at $1.34 \mu\text{m}$. In the present setup, the extra gain suppression at $1.06 \mu\text{m}$ was introduced by the SESA.

3 Results and discussion

Figure 3 shows the average output powers at 1342 nm with respect to the incident pump power in cw and passively Q -switching operations. Without the SESA in the cavity, the cw laser at 1342 nm had a slope efficiency of 37% and an output power of 580 mW at an incident pump power of 1.8 W. In the passively Q -switching regime an average output power of 160 mW was obtained at an incident pump power of 1.8 W. The Q -switching efficiency (ratio of the Q -switched output power to the cw power at the maximum pump power) was found to be 27.6%. This Q -switching efficiency is considerably higher than that obtained with an InGaAsP SESAM [4]

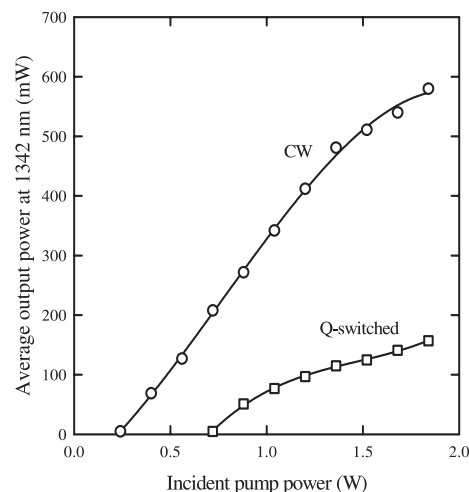


FIGURE 3 Average output powers at $1342 \mu\text{m}$ with respect to the incident pump power in cw and passively Q -switching operations

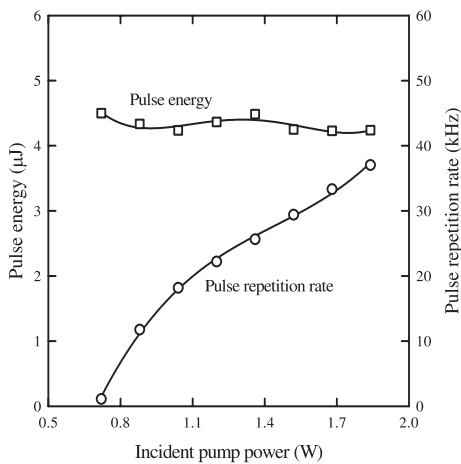


FIGURE 4 Experimental results for the pulse repetition rate and the pulse width versus incident pump power

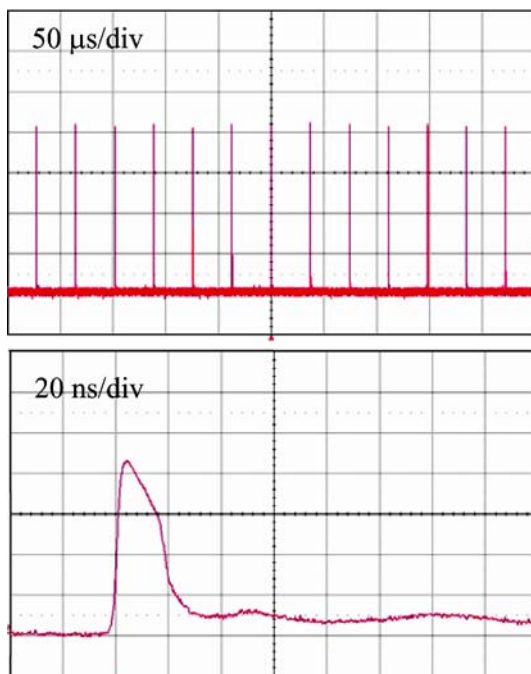


FIGURE 5 (a) Typical oscilloscope trace of a train of output pulses and (b) expanded shape of a single pulse

and is close to the results obtained with $\text{V}^{3+}:\text{YAG}$ [1–3] and $\text{Co}^{2+}:\text{MAS}$ [5] saturable absorbers.

The pulse temporal behavior was recorded by a LeCroy digital oscilloscope (Wavepro 7100, 10 G – samples/sec, 1 GHz bandwidth) with a fast p-i-n photodiode. Figure 4 shows the pulse repetition rate and the pulse energy versus the incident pump power. The pulse repetition rate increases monotonically with the pump power up to 38 kHz.

On the other hand, the pulse energy, like typical passively Q -switched lasers, is insensitive to the pump power. A typical oscilloscope trace of a train of output pulses and an expanded shape of a single pulse are shown in Fig. 5. Under the optimum alignment condition, the pulse-to-pulse amplitude fluctuation was found to be within $\pm 5\%$. The pulse width was measured to be 19 ns. As a consequence, the peak power was found to be higher than 220 W. It is worthwhile mentioning that although the $\text{Nd}:\text{YVO}_4$ crystal is an efficient Raman gain medium, the present intracavity peak power is not high enough to reach the Raman self-conversion.

The InGaAsP QW/barrier structure grown on a Fe-doped substrate was used as a saturable absorber for the Q -switching of a diode-pumped $\text{Nd}:\text{YVO}_4$ laser operating at 1342 nm. An average output power of 160 mW was obtained at an incident pump power of 1.8 W. Stable Q -switched pulses of 19 ns duration with a repetition rate of 38 kHz were generated. The present result indicates the possibility of using InGaAsP QW/barrier structure to generate a Q -switched 1.3 μm laser with peak power greater than 1 kW. Attempts to use InGaAsP-based SESA to scale up Nd-doped 1.3 μm lasers are under way.

ACKNOWLEDGEMENTS The authors gratefully acknowledge various InGaAsP/InP QW structures from TrueLight Corporation. The authors also thank the National Science Council for their financial support of this research under contract No. NSC-93-2112-M-009-034.

REFERENCES

- 1 A.M. Malyarevich, I.A. Denisov, K.V. Yumashev, V.P. Mikhailov, R.S. Conroy, B.D. Sinclair, *Appl. Phys. B* **67**, 555 (1998)
- 2 A.S. Grabtchikov, A.N. Kuzmin, V.A. Lisinetskii, V.A. Orlovich, A.A. Demidovich, K.V. Yumashev, N.V. Kuleshov, H.J. Eichler, M.V. Danailov, *Opt. Mater.* **16**, 349 (2001)
- 3 A. Agnesi, A. Guandalini, G. Reali, J.K. Jabczynski, K. Kocpczynski, Z. Mierczyk, *Opt. Commun.* **194**, 429 (2001)
- 4 K.V. Yumashev, I.A. Denisov, N.N. Posnov, P.V. Prokoshin, V.P. Mikhailov, *Appl. Phys. B* **70**, 179 (2000)
- 5 Y.V. Volk, I.A. Denisov, A.M. Malyarevich, K.V. Yumashev, O.S. Dymshits, A.V. Shashkin, A.A. Zhilin, U. Kang, K.H. Lee, *Appl. Opt.* **43**, 682 (2004)
- 6 V.G. Savitski, N.N. Posnov, P.V. Prokoshin, A.M. Malyarevich, K.V. Yumashev, M.I. Demchuk, A.A. Lipovski, *Appl. Phys. B* **75**, 841 (2002)
- 7 R. Fluck, Z. Zhang, U. Keller, K.J. Weingarten, M. Moser, *Opt. Lett.* **21**, 1378 (1996)
- 8 H.D. Sun, G.J. Valentine, R. Macaluso, S. Calvez, D. Burns, M.D. Dawson, T. Jouhti, M. Pessa, *Opt. Lett.* **27**, 2124 (2002)
- 9 V. Liverini, S. Schön, R. Grange, M. Haiml, S.C. Zeller, U. Keller, *Appl. Phys. Lett.* **84**, 4002 (2004)
- 10 H.C. Lai, A. Li, K.W. Su, M.L. Ku, Y.F. Chen, K.F. Huang, *Opt. Lett.* **30**, 480 (2005)
- 11 R. Fluck, B. Braun, E. Gini, H. Melchior, U. Keller, *Opt. Lett.* **22**, 991 (1997)
- 12 O. Ostinelli, W. Bächtold, M. Haiml, R. Grange, U. Keller, M. Ebnöther, E. Gini, G. Almuneau, *J. Cryst. Growth* **286**, 247 (2006)
- 13 Y. Tsou, E. Garmire, W. Chen, M. Birnbaum, R. Asthana, *Opt. Lett.* **18**, 1514 (1993)

InGaAs quantum-well saturable absorbers for a diode-pumped passively Q-switched Nd:YAG laser at 1123 nm

J. Y. Huang, H. C. Liang, K. W. Su, H. C. Lai, Y.-F. Chen, and K. F. Huang

A low-loss semiconductor saturable absorber based on InGaAs quantum wells was developed for highly efficient Q switching of a diode-pumped Nd:YAG laser operating at 1123 nm. With an incident pump power of 16 W, an average output power of 3.1 W with a Q-switched pulse width of 77 ns at a pulse repetition rate of 100 kHz was obtained. © 2007 Optical Society of America

OCIS codes: 140.3480, 140.3540, 140.3580.

1. Introduction

Nd:YAG crystals that have excellent optical and mechanical properties have been identified to be one of the promising gain media in diode-pumped solid-state lasers.^{1–3} Most of the research involving the ${}^4F_{3/2} \rightarrow {}^4I_{11/2}$ transition of Nd:YAG crystals were focused on the wavelength of 1064 nm. However, there are many Stark components in the ${}^4F_{3/2} \rightarrow {}^4I_{11/2}$ transition of the Nd:YAG crystal, such as 1112, 1117, and 1123 nm.¹ Even though the fluorescent intensity at 1123 nm is in excess of ten times smaller than that at 1064 nm, the diode-end-pumped configuration has been successfully used to achieve highly efficient Nd:YAG 1123 nm lasers.^{4–8} The 1123 nm laser has been demonstrated to be a useful pump source for a thulium upconversion fiber laser with blue light emission.^{4,9} Recently, a diode-pumped passively Q-switched Nd:YAG 1123 nm laser has been achieved by the use of a Cr⁴⁺:YAG crystal with a low modulation depth as a saturable absorber.⁷ Note that the modulation depth is defined as the maximum change of absorption (or reflectivity), which can be induced by incident light with a given wavelength. Nevertheless, the nonsaturable losses of the Cr⁴⁺:YAG crystal are relatively high in comparison with the gain of the Nd:YAG crystal at 1123 nm.

As a consequence, the Cr⁴⁺:YAG crystal brings about a considerably low Q-switching efficiency (ratio of the Q-switched average output power to the cw output power at the same pump power) in the Nd:YAG 1123 nm laser. Therefore it is of practical value to develop the saturable absorbers with low modulation depths (<5%) as well as low nonsaturable losses for the low-gain Nd:YAG 1123 nm laser.

InGaAs/GaAs quantum wells (QWs) have often been used as semiconductor saturable-absorber mirrors (SESAMs) in Nd-doped lasers at 1.06 μm .¹⁰ Even so, such highly strained QWs were previously difficult to use as saturable absorbers for the wavelengths beyond 1.1 μm because of their high nonsaturable losses.¹¹ Recent progress in the growth methodology has made it possible to realize InGaAs QWs with emission wavelengths up to and somewhat beyond 1.2 μm .^{12–14} However, to our knowledge, there has been no work using InGaAs QWs to be SESAMs in Nd:YAG lasers at 1123 nm. Here, for what is believed to be the first time, a diode-pumped passively Q-switched 1123 nm Nd:YAG laser with InGaAs QWs as a saturable absorber is reported. With an incident pump power of 16 W, the compact laser cavity produces an average output power of 3.1 W at 1123 nm with a repetition rate of 100 kHz and a pulse width of 77 ns. The extremely low nonsaturable losses of the SESAM lead to the Q-switching efficiency to be up to 94%.

2. Device Fabrication and Experimental Setup

The SESAM structure was monolithically grown on an undoped GaAs substrate by metal-organic chemical-vapor deposition (MOCVD) to simultaneously serve as

The authors are with the Department of Electrophysics, National Chiao Tung University, Hsinchu, Taiwan. Y.-F. Chen's e-mail address is yfchen@cc.nctu.edu.tw.

Received 2 August 2006; accepted 1 September 2006; posted 14 September 2006 (Doc. ID 73730); published 21 December 2006.

0003-6935/07/020239-04\$15.00/0

© 2007 Optical Society of America

a saturable absorber and an output coupler in the passively Q -switched laser at 1123 nm. Note that the concept of combining the SESAM with an output coupler has been realized in passively Q -switched lasers.¹⁵ The Bragg mirror structure consists of 12 AlAs/GaAs quarter-wavelength layers, designed for a reflectivity of 96% at 1123 nm. The saturable absorber region was grown to comprise two 8 nm thick $\text{In}_{0.34}\text{Ga}_{0.66}\text{As}$ QWs separated by a 10 nm thick GaAs layer. Figure 1 shows the measured results for the low-intensity reflectivity and room-temperature photoluminescence (PL) spectrum of the InGaAs SESAM. It can be seen that the peak wavelength of the PL spectrum is in the vicinity of 1123 nm and the FWHM is approximately 40 nm. Furthermore, the dip in the reflectivity correlates with the maximum in the PL spectrum. The z -scan technique was used to find that the present SESAM device has a modulation depth of

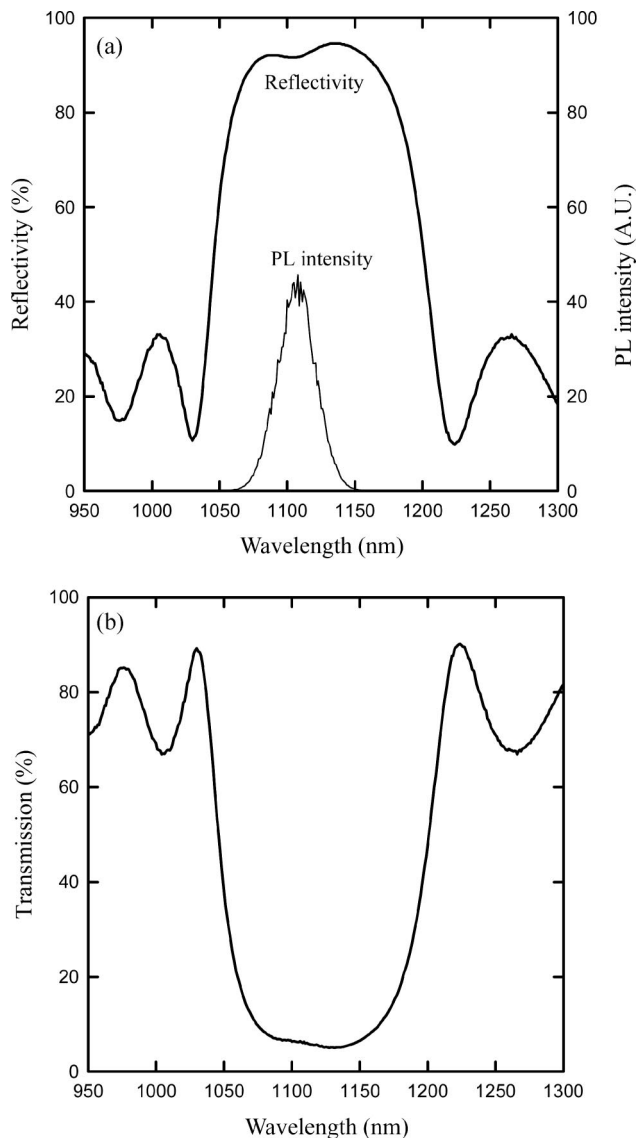


Fig. 1. (a) Measured results for the low-intensity reflectivity and room-temperature PL spectrum of the InGaAs QWS SESAM. (b) Measured results for the low-intensity transmission spectrum.

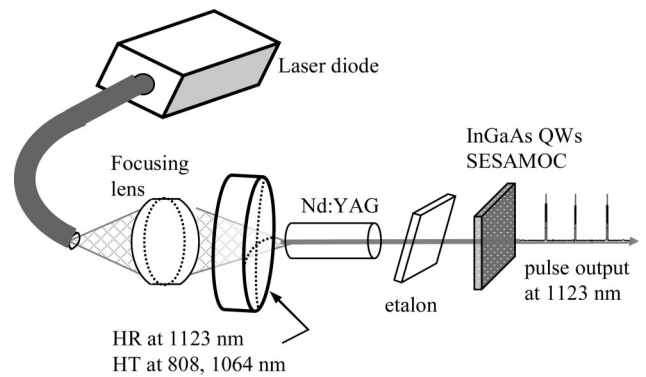


Fig. 2. Schematic of a diode-pumped passively Q -switched Nd:YAG laser at 1123 nm. HR, high reflection; HT, high transmission.

2.8%, nonsaturable losses of 0.4%, and a saturation fluence of $30 \mu\text{J cm}^{-2}$.

Figure 2 shows the experimental configuration for the passively Q -switched 1123 nm Nd:YAG laser with InGaAs QWs used as a saturable absorber and a semiconductor saturable-mirror output coupler (SESAMOC). The active medium was a 1.0 at. % Nd:YAG crystal with a length of 10 mm. Both sides of the laser crystal were coated for anti-reflection at 1123 nm ($R < 0.2\%$). The laser crystal was wrapped with indium foil and mounted on a water-cooled copper block. The pump source was a 20 W 808 nm fiber-coupled laser diode with a core diameter of 800 μm and a numerical aperture of 0.16. A focusing lens with a 12.5 mm focal length and a 90% coupling efficiency was used to reimage the pump beam into the laser crystal. The pump spot radius was approximately 250 μm . The input mirror was a 200 mm radius-of-curvature concave mirror with an antireflection coating at the pump wavelength of 808 nm on the entrance face ($R < 0.2\%$), a high-reflection coating at 1123 nm ($R > 99.8\%$), a high-transmission coating at 808 nm ($T > 90\%$), and 1064 nm ($T > 70\%$) on the other surface. The cavity length was approximately 35 mm. A 0.2 mm thick glass without a coating was used as an etalon to suppress the lasing channels at 1112 and 1116 nm. Without the etalon, simultaneous emission among three wavelengths of 1112, 1116, and 1123 nm was intermittently found at the pump power higher than 12 W. The spectral information of the laser was monitored by an optical spectrum analyzer (Advantest Q8381A). The spectrum analyzer employing a diffraction lattice monochromator can be used for the high-speed measurement of pulse light with the resolution of 0.1 nm. The pulse temporal behavior was recorded by a LeCroy digital oscilloscope (Wavepro 7100, 10 Gs/s, 1 GHz bandwidth) with a fast p-i-n photodiode.

3. Experimental Results

The cw performance of the Nd:YAG laser at 1123 nm was studied first. For this investigation, an output coupler with partial reflection at 1123 nm was used

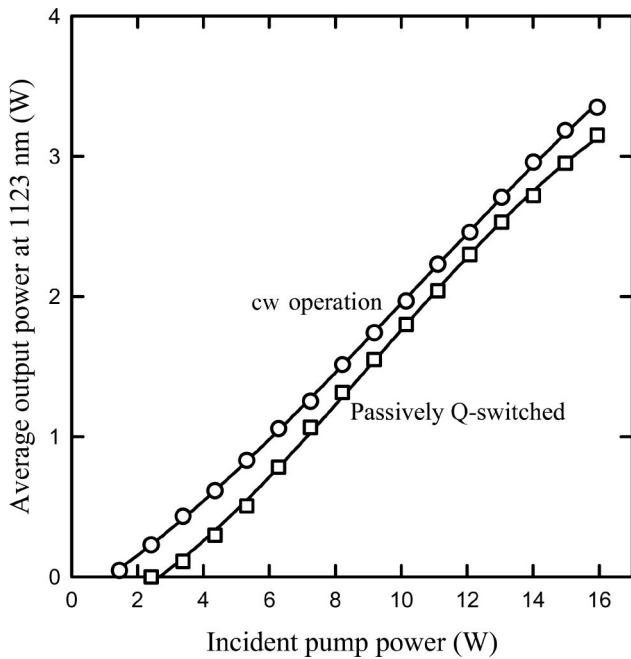


Fig. 3. Average output powers at 1123 nm with respect to the incident pump power in cw and passively *Q*-switching operations.

instead of the above-mentioned InGaAs SESAM. The optimum reflectivity of the output coupler was found to be approximately 96%. The optimum cw performance at 1123 nm provides the baseline for evaluating the passively *Q*-switched efficiency. Figure 3 shows the average output powers at 1123 nm with respect to the incident pump power in cw and passively *Q*-switching operations. In the cw regime, the laser had a slope efficiency of 22.8%; the output power reached 3.3 W at an incident pump power of 16 W. In

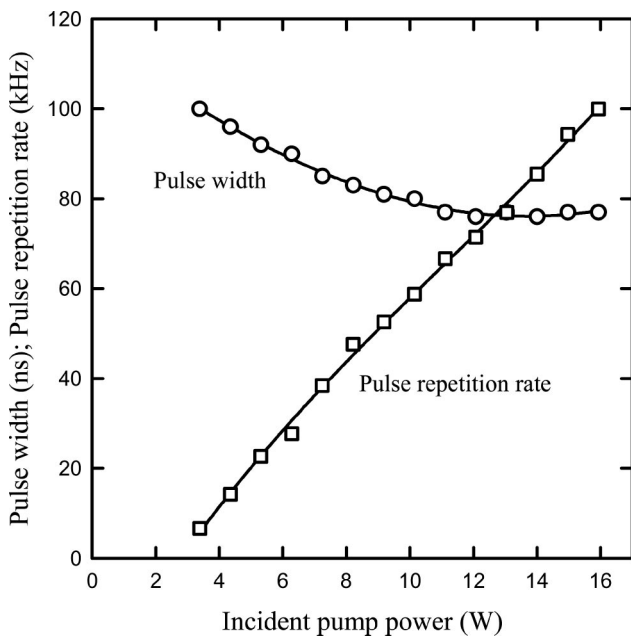


Fig. 4. Experimental results for the pulse repetition rate and the pulse width versus the incident pump power.

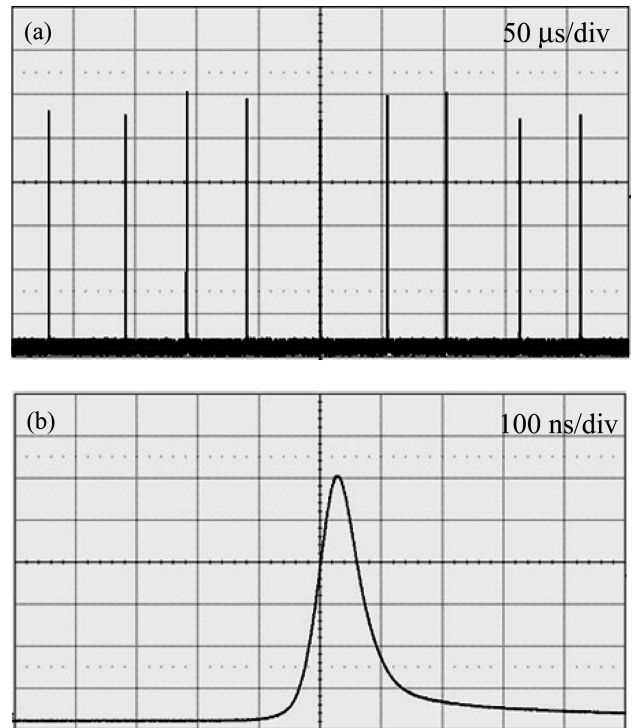


Fig. 5. (a) Typical oscilloscope trace of a train of output pulses and (b) expanded shape of a single pulse.

the passively *Q*-switching regime, an average output power of 3.1 W was obtained at an incident pump power of 16 W. The *Q*-switching efficiency (ratio of the *Q*-switched output power to the cw output power at the maximum pump power) was found to be up to 94%. The nearly perfect *Q*-switching efficiency indicates that the nonsaturable losses of the present InGaAs QWs' SESAM is significantly low.

Figure 4 shows the pulse repetition rate and the pulse width versus the incident pump power. The pulse repetition rate initially increases with pump power and is up to approximately 100 kHz at an incident pump power of 16 W. On the other hand, the pulse width decreases from 100 ns at the threshold to 77 ns at the maximum pump power. As a consequence, the peak power was found to be higher than 400 W. A typical oscilloscope trace of a train of output pulses and an expanded shape of a single pulse are shown in Fig. 5. Under the optimum alignment condition, the pulse-to-pulse amplitude fluctuation was found to be within $\pm 10\%$.

4. Conclusion

InGaAs QWs have been used to be a low-loss semiconductor saturable-absorber output coupler for passive *Q* switching of a diode-pumped Nd:YAG laser operating at 1123 nm. An average output power of 3.1 W with a *Q*-switching efficiency of 94% was obtained at an incident pump power of 16 W. Stable *Q*-switched pulses of 77 ns duration with a repetition rate of 100 kHz were generated. The present result indicates the possibility of using an InGaAs QW structure to mode lock a Nd:YAG laser at 1123 nm. Furthermore, the

low-loss SESAM may be employed to generate the high-peak-power yellow laser at 561 nm with intracavity second-harmonic generation.

The authors thank the National Science Council for their financial support of this research under contract NSC-95-2112-M-009-041.

References

1. W. Koechner, *Solid-State Laser Engineering*, Vol. 1 of Optical Sciences, 5th ed. (Springer, 1999).
2. Y. Kaneda, M. Oka, H. Masuda, and S. Kubota, "7.6 W of continuous-wave radiation in a TEM₀₀ mode from a laser-diode end-pumped Nd:YAG laser," *Opt. Lett.* **17**, 1003–1005 (1992).
3. T. Kellner, F. Heine, and G. Huber, "Efficient laser performance of Nd:YAG at 946 nm and intracavity frequency doubling with LiJO₃, β-BaB₂O₄, and LiB₃O₅," *Appl. Phys. B* **65**, 789–902 (1997).
4. N. Moore, W. A. Clarkson, D. C. Hanna, S. Lehmann, and J. Bösenberg, "Efficient operation of a diode-bar-pumped Nd:YAG laser on the low-gain 1123-nm line," *Appl. Opt.* **38**, 5761–5764 (1999).
5. X. Guo, M. Chen, G. Li, B. Zhang, J. Yang, Z. Zhang, and Y. Wang, "Diode-pumped 1123-nm Nd:YAG laser," *Chin. Opt. Lett.* **2**, 402–404 (2004).
6. Z. Cai, M. Chen, Z. Zhang, R. Zhou, W. Wen, X. Ding, and J. Yao, "Diode end-pumped 1123-nm Nd:YAG laser with 2.6-W output power," *Chin. Opt. Lett.* **3**, 281–282 (2005).
7. Y. F. Chen and Y. P. Lan, "Diode-pumped passively *Q*-switched Nd:YAG laser at 1123 nm," *Appl. Phys. B* **79**, 29–31 (2004).
8. Y. F. Chen, Y. P. Lan, and S. W. Tsai, "High-power diode-pumped actively *Q*-switched Nd:YAG laser at 1123 nm," *Opt. Commun.* **234**, 309–313 (2004).
9. R. Paschotta, N. Moore, W. A. Clarkson, A. C. Tropper, D. C. Hannd, and G. Mazé, "230 mW of blue light from a thulium doped upconversion fiber," *IEEE J. Sel. Top. Quantum Electron.* **3**, 1100–1102 (1997).
10. G. J. Spühler, R. Paschotta, R. Fluck, B. Braun, M. Moser, G. Zhang, E. Gini, and U. Keller, "Experimentally confirmed design guidelines for passively *Q*-switched microchip lasers using semiconductor saturable absorbers," *J. Opt. Soc. Am. B* **16**, 376–388 (1999).
11. R. Fluck, G. Zhang, U. Keller, K. J. Weingarten, and M. Moser, "Diode-pumped passively mode-locked 1.3-μm Nd:YVO₄ and Nd:YLF lasers," *Opt. Lett.* **21**, 1378–1380 (1996).
12. F. Bugge, G. Erbert, J. Fricke, S. Gramlich, R. Staske, H. Wenzel, U. Zeimer, and M. Weyers, "12 W continuous-wave diode lasers at 1120 nm with InGaAs quantum wells," *Appl. Phys. Lett.* **79**, 1965–1967 (2001).
13. S. Mogg, N. Chitica, R. Schatz, and M. Hammar, "Properties of highly strained InGaAs/GaAs quantum wells for 1.2-μm laser diodes," *Appl. Phys. Lett.* **81**, 2334–2336 (2002).
14. T. Kondo, D. Schlenker, T. Miyamoto, Z. Chen, M. Kawaguchi, E. Guardes, F. Koyama, and K. Iga, "Lasing characteristics of 1.2 μm highly strained GaInAs/GaAs quantum well lasers," *Jpn. J. Appl. Phys.* **40**, 467–471 (2001).
15. G. J. Spühler, S. Reffert, M. Haiml, M. Moser, and U. Keller, "Output-coupling semiconductor saturable absorber mirror," *Appl. Phys. Lett.* **78**, 2733–2735 (2001).

High power passively Q-switched ytterbium fiber laser with Cr⁴⁺:YAG as a saturable absorber

J. Y. Huang, H. C. Liang, K. W. Su, and Y. F. Chen

Department of Electrophysics, National Chiao Tung University, Hsinchu, Taiwan
yfchen@cc.nctu.edu.tw

Abstract: We report an efficient high-peak-power and high-average-power passively Q-switched ytterbium fiber laser with a Cr⁴⁺:YAG crystal as a saturable absorber in an external-resonator configuration. At an incident pump power of 17.5 W, the passively Q-switched fiber laser produces an average power greater than 6.2 W with a pulse repetition rate of 48 kHz. The output pulses noticeably display a mode-locking phenomenon that leads to the maximum peak power to be higher than 20 kW.

©2007 Optical Society of America

OCIS codes: (140.3510) Lasers, fiber; (140.3480) Lasers, diode-pumped; (140.3540) Lasers, Q-switched.

References and links

1. L. Zenteno, "High-power double-clad fiber lasers," *J. Lightwave Technol.* **11**, 1435-1446 (1993).
2. M. J. F. Digonnet, *Rare-Earth-Doped Fiber Lasers and Amplifiers*, 2nd ed. (Marcel Dekker, 2001).
3. Z. J. Chen, A. B. Grudinin, J. Porta and J. D. Minelly, "Enhanced Q switching in double-clad fiber lasers," *Opt. Lett.* **23**, 454-456 (1998).
4. J. A. Alvarez-Chavez, H. L. Offerhaus, J. Nilson, P. W. Turner, W. A. Clarkson, and D. J. Richardson, "High-energy high-power ytterbium-doped Q-switched fiber laser," *Opt. Lett.*, **25**, 37-39 (2000).
5. Y. X. Fan, F. Y. Lu, S. L. Hu, K. C. Lu, H. J. Wang, X. Y. Dong, J. L. He, and H. T. Wang, "Tunable high-peak-power, high-energy hybrid Q-switched double-clad fiber laser," *Opt. Lett.* **29**, 724-726 (2004).
6. Y. Wang and C. Q. Xu, "Modeling and optimization of Q-switched double-clad fiber lasers," *Appl. Opt.* **45**, 2058-2071 (2006).
7. T. Tordella, H. Djellout, B. Dussardier, A. Saissy, and G. Monnom, "High repetition rate passively Q-switched Nd³⁺:Cr⁴⁺ all-fibre laser," *Electron. Lett.* **39**, 1307-1308 (2003).
8. A. Fotiadi, A. Kurkov, and I. Razdobreev, "All-fiber passively Q-switched ytterbium laser," *CLEO/Europe-EQEC 2005, Technical Digest, CJ 2-3, Munich, Germany* (2005).
9. P. Adel, M. Auerbach, C. Fallnich, S. Unger, H.-R. Müller, and J. Kirchhof, "Passive Q-switching by Tm³⁺ co-doping of a Yb³⁺-fiber laser," *Opt. Express* **11**, 2730-2735 (2003).
10. M. Laroche, A. M. Chardon, J. Nilsson, D. P. Shepherd, W. A. Clarkson, S. Girard, and R. Moncorgé, "Compact diode-pumped passively Q-switched tunable Er-Yb double-clad fiber laser," *Opt. Lett.* **27**, 1980-1982 (2002).
11. V. N. Philippov, A. V. Kiryanov, and S. Unger, "Advanced configuration of erbium fiber passively Q-switched laser with Co²⁺:ZnSe crystal as saturable absorber," *IEEE Photon. Technol. Lett.* **16**, 57-59 (2004).
12. F. Z. Qamar and T. A. King, "Passive Q-switching of the Tm-silica fiber laser near 2 μm by Cr²⁺:ZnSe saturable absorber crystal," *Opt. Commun.* **248**, 501-505 (2005).
13. R. Paschotta, R. Häring, E. Gini, H. Melchior, U. Keller, H. L. Offerhaus, and D. J. Richardson, "Passively Q-switched 0.1 mJ fiber laser system at 1.53 μm," *Opt. Lett.* **24**, 388-390 (1999).
14. M. Laroche, H. Gilles, S. Girard, N. Passilly, and K. Ait-Ameur, "Nanosecond pulse generation in a passively Q-switched Yb-doped fiber laser by Cr⁴⁺:YAG saturable absorber," *IEEE Photon. Technol. Lett.* **18**, 764-766 (2006).
15. J. Dong, P. Deng, Y. Liu, Y. Zhang, J. Xu, W. Chen, and X. Xie, "Passively Q-switched Yb:YAG laser with Cr⁴⁺:YAG as the saturable absorber," *Appl. Opt.* **40**, 4303-4307 (2001).
16. J. I. Mackenzie and D. P. Shepherd, "End-pump, passively Q-switched Yb:YAG double-clad waveguide laser," *Opt. Lett.* **27**, 2161-2163 (2002).
17. H. Wu, P. Yan, M. Gong, and Q. Liu, "A passively Q-switched diode pumped Yb:YAG microchip laser," *Chin. Opt. Lett.* **1**, 697-698 (2003).

18. V. E. Kisel, A. E. Troshin, N. A. Tolstik, V. G. Shcherbitsky, N. V. Kuleshov, V. N. Matrosov, T. A. Matrosova, and M. I. Kupchenko, "Q-switched Yb³⁺:YVO₄ laser with Raman self-conversion," *Appl. Phys. B* **80**, 471-473 (2005).
19. X. Zhang, A. Brenier, Q. Wang, Z. Wang, J. Chang, P. Li, S. Zhang, S. Ding, and S. Li, "Passive Q-switching characteristics of Yb³⁺:Gd₃Ga₅O₁₂ crystal," *Opt. Express* **13**, 7708-7719 (2005).
20. Y. Kalisky, O. Kalisky, U. Rachum, G. Boulon, and A. Brenier, "Comparative performance of passively Q-switched diode-pumped Yb:GGG, Yb:YAG and Yb-doped tungstates lasers using Cr⁴⁺-doped garnets," *Proc. SPIE Vol. 6100*, 61001K (2006).
21. Y. F. Chen, Y. P. Lan, and H. L. Chang, "Analytical model for design criteria of passively Q-switched lasers," *IEEE J. Quantum Electron.* **37**, 462-468 (2001).
22. X. Zhang, S. Zhao, Q. Wang, Q. Zhang, L. Sun, and S. Zhang, "Optimization of Cr⁴⁺-doped saturable absorber Q-switched lasers," *IEEE J. Quantum Electron.* **33**, 2286-2294 (1997).
23. K. Lu and N. K. Dutta, "Spectroscopic properties of Yb-doped silica glass," *J. Appl. Phys.* **91**, 576-581 (2002).
24. Y. Shimony, Z. Burshtein, and Y. Kalisky, "Cr⁴⁺: YAG as passive Q-switch and Brewster plate in a pulsed Nd:YAG laser," *IEEE J. Quantum Electron.* **31**, 1738-1741 (1995).
25. L. A. Zenteno, H. Po, and N. M. Cho, "All-solid-state passively Q-switched mode-locked Nd-doped fiber laser," *Opt. Lett.* **15**, 115-117 (1990).
26. Y. F. Chen and S. W. Tsai, "Simultaneous Q-switching and mode-locking in a diode-pumped Nd: YVO₄-Cr⁴⁺:YAG laser," *IEEE J. Quantum Electron.* **37**, 580-586 (2001).

1. Introduction

High-power diode-pumped rare-earth-doped double-clad fiber lasers have been promised as efficient and compact light sources with excellent beam quality, high efficiency, and a broad tuning range [1, 2]. Compared to cw fiber lasers, high-peak-power Q-switched fiber lasers are practically useful in numerous applications, such as range finding, remote sensing, industrial processing, and medicine [3-6]. Active Q-switching is typically achieved by inserting an acoustic-optic or an electro-optic modulator into the cavity. On the other hand, passive Q-switching by means of saturable absorbers is a convenient technique to simplify the cavity design and eliminate the need for external Q-switching electronics. So far, Cr⁴⁺-doped [7], Sm-doped [8], and Tm³⁺-Yb³⁺ co-doped [9] fibers have been developed as fiber saturable absorbers in fiber laser systems in the range of 1.0-1.1 μm. Another effective approach for passive Q-switching of fiber lasers is to use crystals [10-12] or semiconductor materials [13] as saturable absorbers. Recently, giant pulses with a duration of 2.7 ns and a peak power of 9 kW have been achieved in a Yb-doped fiber by a Cr⁴⁺:YAG saturable absorber [14]. However, the average power and the conversion efficiency have been limited by 0.3 W and 17.6%, respectively. In view of that, it is of practical interest and value to develop high-average-power and high-peak-power fiber laser sources.

Here we report on an efficient high-peak-power and high-average-power passively Q-switched Yb-doped fiber laser with a Cr⁴⁺:YAG saturable absorber. The high conversion efficiency is achieved by using a highly doped doubly clad fiber which combines a large core with excellent beam quality and high cladding absorption. With an incident pump power of 17.5 W, the fiber laser, operating at 48 kHz, produces an average output power up to 6.2 W with a pulse energy of 110~130 μJ. The mode-locking phenomenon leads to the maximum peak power to be higher than 20 kW.

2. Experimental setup

Figure 1 displays the schematic of the experimental setup for the passively Q-switched Yb-doped fiber laser that consists of a 3-m Yb-doped fiber and an external feedback cavity including a saturable absorber. The fiber has an absorption coefficient of 10.8 dB/m at 976 nm and a double-clad structure with a diameter of 350 μm octagonal outer cladding, diameter of 250 μm octagonal inner cladding with a numerical aperture (NA) of 0.46, and 25 μm circular core with a NA of 0.07. Note that the use of larger diameter cores is vital for storing higher pulse energies. Here the fiber possesses a low NA core to sustain the excellent beam quality. The end facets of the fiber were cut to be normal incident. Therefore, the lasing by end facets usually occurred for the free-running operation. The external cavity consists of a collimating

lens of 50-mm focal length, a focusing lens of 25-mm focal length to focus the fiber output into a Cr⁴⁺:YAG saturable absorber, a re-imaging lens to re-image the beam on a highly reflective mirror for feedback. The Cr⁴⁺:YAG crystal has a thickness of 1.5 mm with 40% initial transmission at 1075 nm. Both sides of the Cr⁴⁺:YAG crystal were coated for antireflection at 1075 nm ($R < 0.2\%$). The focal lengths of the collimating and focusing lenses were chosen to have a beam waist of 12.5 μm inside the saturable absorber. The saturable absorber was wrapped with indium foil and mounted in a copper block without active cooling. A translation stage was used to adjust the longitudinal position of the Cr⁴⁺:YAG saturable absorber for minimizing the beam volume inside the crystal and achieving the lowest Q-switching threshold.

The pump source was a 20-W 976-nm fiber-coupled laser diode with a core diameter of 400 μm and a NA of 0.22. A focusing lens with 25 mm focal length and 92% coupling efficiency was used to re-image the pump beam into the fiber through a dichroic mirror with high transmission ($>90\%$) at 976 nm and high reflectivity ($>99.8\%$) at 1075 nm. The pump spot radius was approximately 200 μm . The pulse temporal behavior was recorded by a LeCroy digital oscilloscope (Wavepro 7100; 10G samples/sec; 1 GHz bandwidth) with a fast InGaAs photodiode.

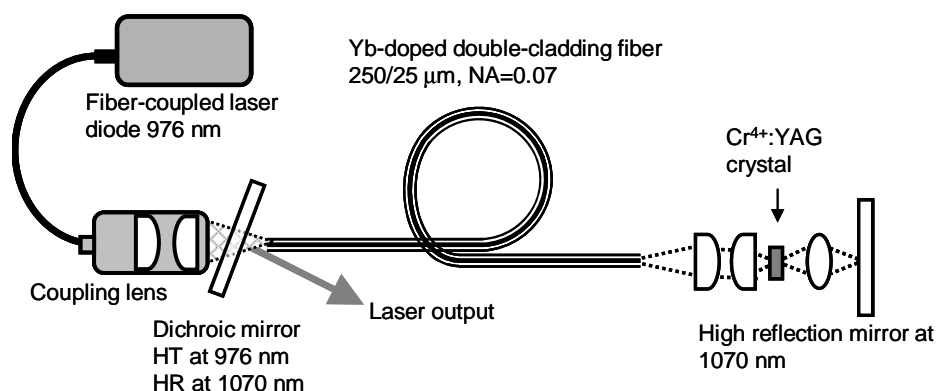


Fig. 1. Schematic of a diode-pumped passively Q-switched Yb-doped double-clad fiber laser. HR, high reflection; HT, high transmission.

3. Results and discussions

The cw performance of the present fiber laser was studied first. For this investigation, the external cavity only comprised a focusing lens and a high reflector ($R > 99.8\%$ at 1075 nm). The cw performance provides the baseline for evaluating the passively Q-switched efficiency. Figure 2 shows the average output powers with respect to the incident pump power in cw and passively Q-switching operations. In the cw regime the laser had a slope efficiency of 61.6%; the output power reached 10.1 W at an incident pump power of 17.5 W. In the passively Q-switching regime an average output power of 6.2 W was obtained at an incident pump power of 17.5 W. The Q-switching efficiency (ratio of the Q-switched output power to the CW one at the maximum pump power) was found to be up to 61.3%. This Q-switching efficiency is generally superior to those of Yb-doped crystal lasers with Cr⁴⁺:YAG crystals as saturable absorbers [15-20]. The M^2 beam-quality factor was measured to be < 1.5 over the complete output power range. On the other hand, no damage to the fiber was observed over several hours of operation, and the laser performance was reproducible on a day-to-day basis.

Figure 3 shows the pulse repetition rate and the pulse energy versus the incident pump power. The pulse repetition rate initially increases with pump power, and is approximately up

to 50 kHz at an incident pump power of 17.5 W. Like typically passively Q-switched lasers, the pulse energies weakly depend on the pump power and their values are found to be in the range of 110~130 μJ .

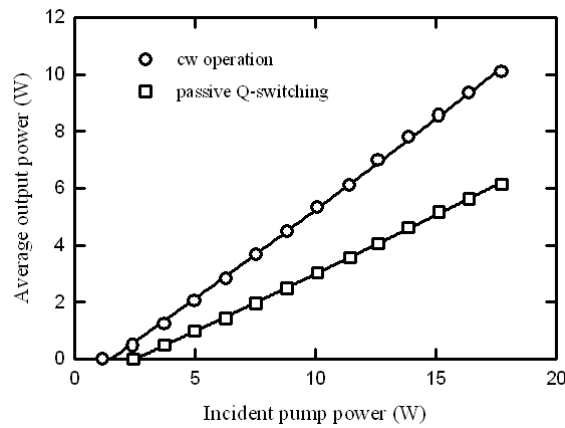


Fig. 2. Dependence of the average output power on the incident pump power for the cw and passive Q-switching operations.

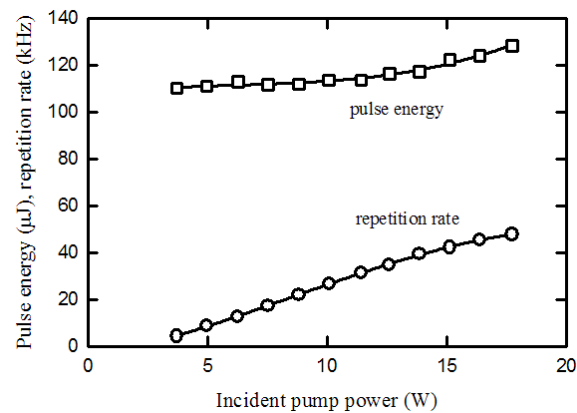


Fig. 3. Pulse repetition rate and the pulse energy versus the incident pump power

With the model of the coupled rate equations, the expression for the pulse energy of the passively Q-switched has been derived to be given by [21, 22]

$$E = \frac{h\nu A}{2\sigma\gamma} \ln(1/R)x \quad (1)$$

where $h\nu$ is the laser photon energy, A is the mode area in the gain medium, σ is the stimulated emission cross section of the gain medium, $\gamma=2$ is the inversion reduction factor, R is the reflectivity of the output mirror, and the parameter x represents the extraction efficiency of the energy stored in the gain medium through the lasing process. The equation for the parameter x is given by

$$1 - e^{-x} - \frac{(1 - \beta)\ln(1/T_o^2)}{\ln(1/T_o^2) + \ln(1/R) + L} - \frac{1 - e^{-\alpha x}}{\alpha} - \frac{\beta\ln(1/T_o^2) + \ln(1/R) + L}{\ln(1/T_o^2) + \ln(1/R) + L} x = 0, \quad (2)$$

where

$$\alpha = \frac{1}{\gamma} \frac{\sigma_{gs}}{\sigma} \frac{A}{A_s}, \quad \beta = \frac{\sigma_{es}}{\sigma_{gs}}, \quad (3)$$

L is the intracavity round-trip dissipative optical loss, T_o is the initial transmission of the saturable absorber, A_s is the effective mode area in the saturable absorber, σ_{gs} and σ_{es} are the ground-state and excited-state absorption cross sections of the saturable absorber, respectively. With Eqs. (1)-(3) and the values of the parameters: $\sigma = 3 \times 10^{-21} \text{ cm}^2$ [23], $\sigma_{gs} = 8.7 \times 10^{-19} \text{ cm}^2$ [24], $\sigma_{es} = 2.2 \times 10^{-19} \text{ cm}^2$ [24], $T_o = 0.4$, $R = 0.04$, $L = 0.04$, $A = 4.9 \times 10^{-6} \text{ cm}^2$, and $A_s = 6.3 \times 10^{-6} \text{ cm}^2$, the calculated result of the parameter x was found to be approximately 0.65. With this calculated value and Eq. (1), the pulse energy could be found to be 155 μJ . This value agrees very well with the experimental result. Furthermore, the present pulse energy is comparable with the maximum energy storage capacity of the laser given by the saturation energy $E_{sat} = h\nu A / \sigma = 303 \mu\text{J}$. To confirm the theoretical analysis, we changed the mode area in the absorber by moving the absorber away from the focal plane. It was found that the output pulse energy decreased from 130 μJ to 90 μJ as the mode area A_s was changed to be $1.1 \times 10^{-5} \text{ cm}^2$. This experimental result is close to the theoretical value of 97 μJ . The good agreement validates the present analysis.

A typical oscilloscope trace of Q-switched pulse train is shown in Fig. 4(a). With the optimum alignment, the pulse-to-pulse stability was found to be approximately $\pm 15\%$. The pulse-to-pulse stability may be improved by the angle-cleaved end facets of the fiber. The stable self-mode-locking pulse output could be usually observed as the pump power is higher than 10 W. Figure 4 (b) shows the temporal shape of a single Q-switched pulse envelope, which was recorded at the maximum pump power. It can be seen that the self-mode-locking effect [25, 26] leads to the formation of the mode-locked pulses inside the Q-switched pulse envelope. The separation of the mode-locked pulses was found to be 33 ns, which matched exactly with the cavity roundtrip time and corresponded to a repetition rate of 30 MHz. The estimated energy of the highest pulse inside envelope was found to be close to 50 μJ . As shown in Fig. 4(c), the expanded oscilloscope traces reveal that the mode-locked pulse width is approximately 2.1 ns. As a consequence, the peak power can be found to be more than 20 kW. This is to our knowledge by far the highest mode-locked peak power reported for diode-pumped Yb-doped fiber lasers with simultaneous Q-switching. The present result indicates that the output peak power can be significantly enhanced by using a fiber with a larger core size and a saturable absorber with a lower initial transmission.

The spectral information was measured by an optical spectrum analyzer (Advantest Q8381A) that utilizes a grating monochromator for the high speed measurement of pulse light with the resolution of 0.1 nm. Figure 5 shows the output spectrum of the passively Q-switched fiber laser at an average output power of 5 W. The experimental FWHM line width was approximately 0.2 nm. Note that the mode-locked pulse width of 2.1 ns is consistent with the measured bandwidth of 0.2 nm and the pulses are near transform-limited.

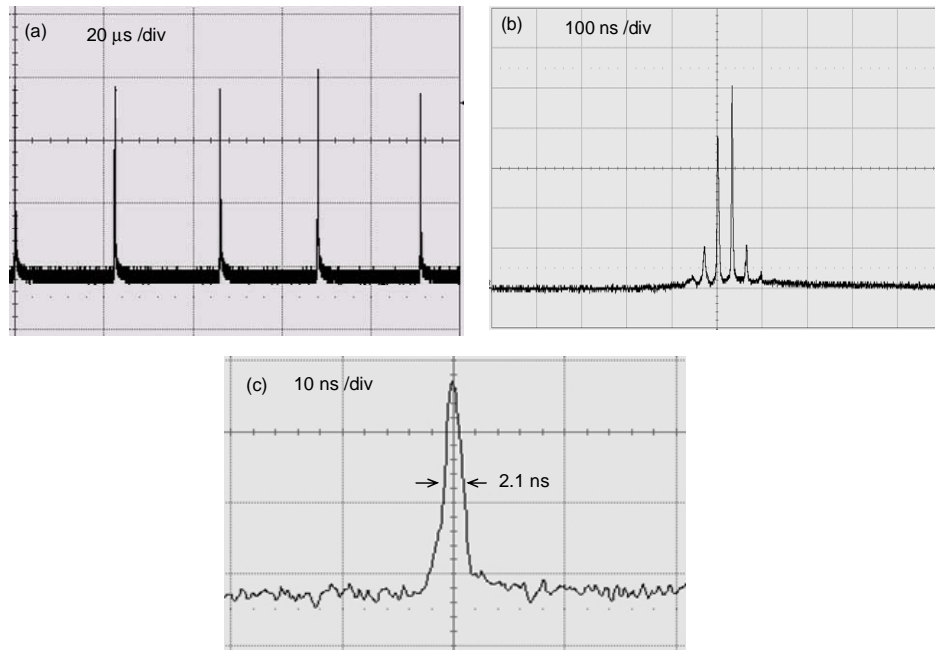


Fig. 4. (a) Oscilloscope traces of a train of Q-switched pulses, (b) Oscilloscope traces of a typical Q-switched envelope, (c) Oscilloscope traces of a mode-locked pulse inside the Q-switched envelope.

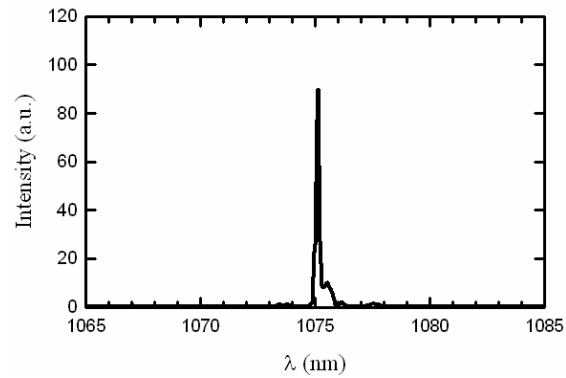


Fig. 5. Output spectrum of the Q-switched laser at an output power of 5 W.

4. Conclusion

In conclusion, we have demonstrated an efficient high-peak-power and high-average-power passively Q-switched Yb-doped fiber laser with a Cr⁴⁺:YAG crystal as a saturable absorber in an external-resonator configuration. Greater than 6.2 W of an average output power at a repetition rate of 48 kHz was generated with a 17.5-W diode pump power. Moreover, the mode-locking phenomenon enhances the peak power higher than 20 kW. It is believed that this efficient Q-switched fiber laser should be a useful light source for technical applications because of its high average power as well as high peak power.

Acknowledgments

The author thanks the National Science Council for their financial support of this research under Contract No. NSC-95-2112-M-009-041-MY2.

AQ: A **Passively Q-switched Yb³⁺:YCa₄O(BO₃)₃ laser with InGaAs quantum wells as saturable absorbers**

H. C. Liang, J. Y. Huang, K. W. Su, H. C. Lai, Y. F. Chen, K. F. Huang, H. J. Zhang, J. Y. Wang, and M. H. Jiang

A diode-pumped Yb:YCOB laser at 1086 nm is passively Q switched by using InGaAs quantum wells as saturable absorbers and utilizing the Bragg mirror structure as an output coupler. With an absorbed pump power of 9.2 W the laser produces pulses of 100 ms duration with average pulse energy of as much as 165 μ J at a pulse repetition rate of 7 kHz. © 2007 Optical Society of America
OCIS codes: 140.0140, 140.3540, 140.3580.

1. Introduction

In the past few years, ytterbium (Yb³⁺)-doped lasers have attracted a great deal of interest because of their practical applications in diode-pumped solid-state lasers.^{1–10} Despite the quasi-three-level nature, the Yb³⁺-doped gain media have numerous advantages in comparison with their Nd³⁺ counterparts. The main advantages of the Yb ion include the availability of high doping levels without concentration quenching, very small quantum defects, and a simple electronic structure that prevents undesired effects such as up-conversion and excited-state absorption. Another important advantage of Yb³⁺-doped gain media is their long upper-laser-level lifetimes that enhance the energy-storage capabilities for the Q-switching operation.

Passively Q-switched all-solid-state lasers are of great interest because of their potential applications in remote sensing, ranging, micromachining, and nonlinear wavelength conversion. Most of the work on passively Q-switched Yb³⁺-doped lasers has been performed with Cr⁴⁺:YAG crystals as saturable absorbers.^{11–16} In addition to Cr⁴⁺:YAG crystals, the

semiconductor saturable absorber mirror (SESAM) has been successfully used in a passively Q-switched Yb:YAG laser to generate pulses with 1.1 μ J energy, 1.9 kW peak power, and a repetition rate of 12 kHz.¹⁷ Even so, to the best of our knowledge, SESAMs have never been applied to other Yb³⁺-doped lasers. Among Yb-doped hosts, Yb-doped calcium oxyborate crystals, Yb³⁺:Ca₄YO(BO₃)₃ (Yb:YCOB) and Yb³⁺:Ca₄GdO(BO₃)₃ (Yb:GCOB), possess longer upper-level lifetimes.⁵ The upper-level lifetimes of Yb:YCOB and Yb:GCOB crystals have been found to be more than twice that of Yb:YAG crystal. In this work we present a passively Q-switched operation using InGaAs quantum wells (QWs) as the saturable absorbers in a diode-pumped Yb:YCOB laser. With an absorbed pump power of 9.2 W, the compact laser cavity produces an average output power of 1.15 W at 1086 nm with a repetition rate of 7 kHz and a pulse width of 100 ns. The corresponding pulse energy and peak power are up to 165 μ J and 1.65 kW, respectively.

2. Experimental Setup

Figure 1 shows the experimental configuration for the passively Q-switched 1086 nm Yb:YCOB laser with InGaAs QWs used as saturable absorbers and an output coupler (SESAMOC). The concept of combining the SESAM with an output coupler has been realized in passively Q-switched lasers.¹⁸ The present SESAM structure was monolithically grown on an undoped GaAs substrate by metalorganic chemical vapor deposition (MOCVD) to simultaneously serve as a saturable absorber and an output coupler in the passively Q-switched laser at 1086 nm. The Bragg mirror structure consists of 12 AlAs/GaAs quarter-wavelength layers, designed for a reflectivity of 97.5%

H. C. Liang, J. Y. Huang, K. W. Su, H. C. Lai, Y. F. Chen (yfchen@cc.nctu.edu.tw), and K. F. Huang are with the Department of Electrophysics, National Chiao Tung University, Hsinchu, Taiwan. H. J. Zhang, J. Y. Wang, and M. H. Jiang are with the National Laboratory of Crystal Materials and the Institute of Crystal Materials, Shandong University, China.

Received 4 October 2006; revised 3 December 2006; accepted 7 December 2006; posted 11 December 2006 (Doc. ID 75785); published 00 Month 2007.

0003-6935/07/120001-05\$15.00/0

© 2007 Optical Society of America

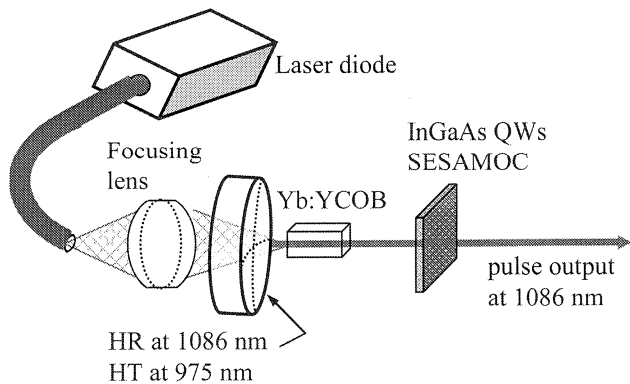


Fig. 1. Schematic of a diode-pumped passively Q-switched Yb:YCOB laser at 1086 nm: HR, high reflection; HT, high transmission.

at 1086 nm. The saturable absorber region was grown to comprise two 8 nm thick $\text{In}_{0.34}\text{Ga}_{0.66}\text{As}$ QWs separated by a 10 nm thick GaAs layer. It was experimentally found that the SESAM device has a modulation depth of 1.5% and a saturation fluence of $20 \mu\text{J}/\text{cm}^{-2}$. The saturation measurements were performed using nanosecond Q-switched laser pulses to coincide with the present Q-switched experiment. The thickness of the GaAs substrate was 350 μm . The back side of the GaAs substrate was coated for antireflection at 1086 nm ($R < 2\%$). The SESAM device was surface mounted in a water-cooled copper block without any transparent heat spreader on the surface.

The active medium was 20 at. % Yb:YCOB crystal with a length of 4 mm. Both sides of the laser crystal were coated for antireflection at 1086 nm ($R < 0.2\%$). The laser crystal was wrapped with indium foil and mounted in a water-cooled copper block. The pump source was a 15 W 975 nm fiber-coupled laser diode with a core diameter of 400 μm and a NA of 0.20. A focusing lens with a 12.5 mm focal length and 90% coupling efficiency was used to reimage the pump beam into the laser crystal. The pump spot radius was approximately 150 μm . The input mirror was a 500 mm radius-of-curvature concave mirror with antireflection coating at the pump wavelength of 975 nm on the entrance face ($R < 0.2\%$) and high-reflection coating at 1086 nm ($R > 99.8\%$) and high-transmission coating at 975 nm ($T > 85\%$) on the other surface. The cavity length was approximately 20 mm. The spectral information of the laser was monitored by an optical spectrum analyzer (Advantest Q8381A, ■). The spectrum analyzer employing diffraction lattice monochromator can be used for high-speed measurement of pulse light with a resolution of 0.1 nm. The pulse temporal behavior was recorded by a LeCroy digital oscilloscope (Wavepro 7100, 10 Gs/s, 1 GHz bandwidth) with a fast p.i.n. photodiode.

3. Experimental Results

The cw performance of the Yb:YCOB laser at 1086 nm was studied first. For this investigation an output

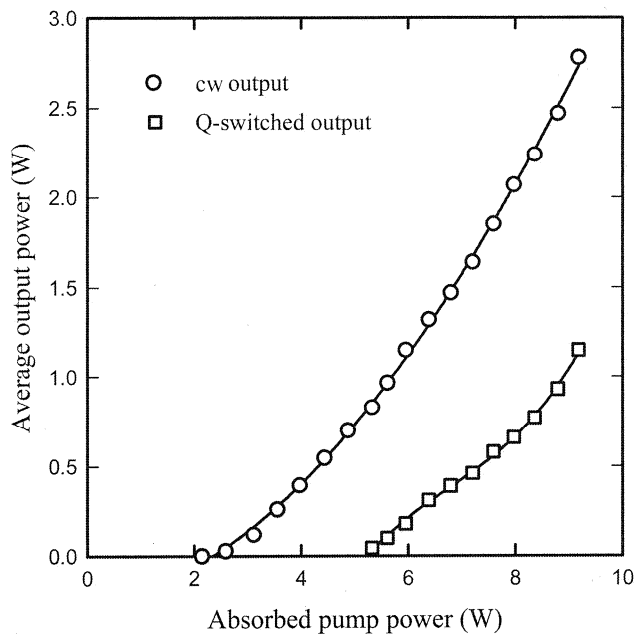


Fig. 2. Average output powers at 1086 nm with respect to the absorbed pump power in cw and passively Q-switching operations.

coupler with partial reflection at 1086 nm was used instead of the above-mentioned InGaAs SESAM. The optimum reflectivity of the output coupler was found to be approximately 98%. The optimum cw performance at 1086 nm provides the baseline for evaluating the passively Q-switched efficiency. Figure 2 shows the average output powers at 1086 nm with respect to the absorbed pump power in cw and passively Q-switching operations. In the cw regime the laser had a slope efficiency of 40%; the output power reached 2.8 W at an absorbed pump power of 9.2 W. The beam-quality factor M^2 was found to be less than 1.5 for all pump powers. In the passively Q-switching regime an average output power of 1.15 W was obtained at an absorbed pump power of 9.2 W. The Q-switching efficiency (the ratio of the Q-switched output power to the cw one at the maximum pump power) was found to be up to 41%. This Q-switching efficiency is comparable to those of Yb-doped lasers with Cr^{4+} :YAG crystals as saturable absorbers.¹¹⁻¹⁶ Here the output power is limited by the available absorbed pump power not by the cracking of the laser crystal. Figures 3(a) and 3(b) depict, respectively, the experimental results for the lasing spectra in the cw and passive Q-switching operations at an absorbed pump power of 9.2 W. It can be seen that the spectral bandwidth of the Q-switching mode is nearly similar to that of the cw mode. In other words, the present SESAM device does not limit the lasing bandwidth, and it should be a practical saturable absorber to mode lock Yb-doped lasers.

Figure 4 shows the pulse repetition rate and the pulse energy versus the absorbed pump power. The pulse repetition rate initially increases with pump power, and it is approximately up to 7 kHz at an absorbed pump power of 9.2 W. Like typically pas-

AQ: B

AQ: C

F2

F3

F4

rich2/zod-osa/zod-osa/zod01207/zod3927-07z xppws S=1 1/25/07 Art: LP-75785

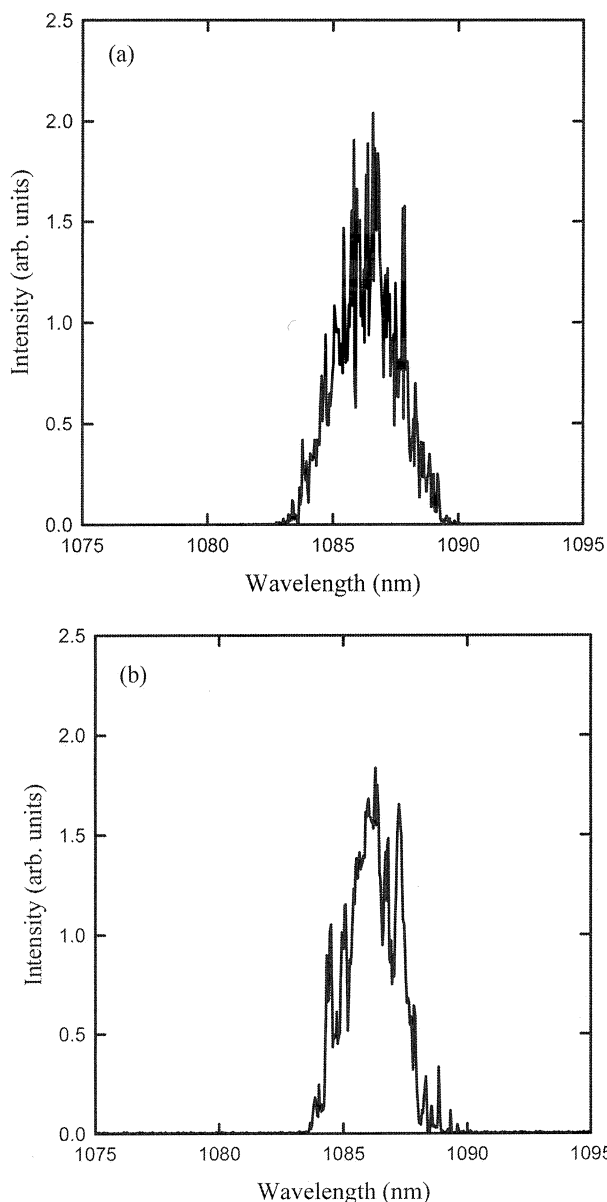


Fig. 3. Experimental results for the lasing spectra at an absorbed pump power of 9.2 W. (a) cw operation, (b) passive Q-switching operation.

sively Q-switched lasers, the pulse energy is almost unrelated to the pump power, and its value is 165 μJ on average. On the whole, the pulse width remains approximately constant at 100 ns. With the measured pulse energy and pulse width, the peak power can be found to be higher than 1.6 kW. A typical oscilloscope trace of a train of output pulses and an expanded shape of a single pulse are shown in Fig. 5. Under the optimum alignment condition, the pulse-to-pulse amplitude fluctuation was found to be within $\pm 10\%$.

4. Analysis

The coupled rate equations have been used to model a passively Q-switched laser in many investigations.^{19,20} Here we analyze the experimental result

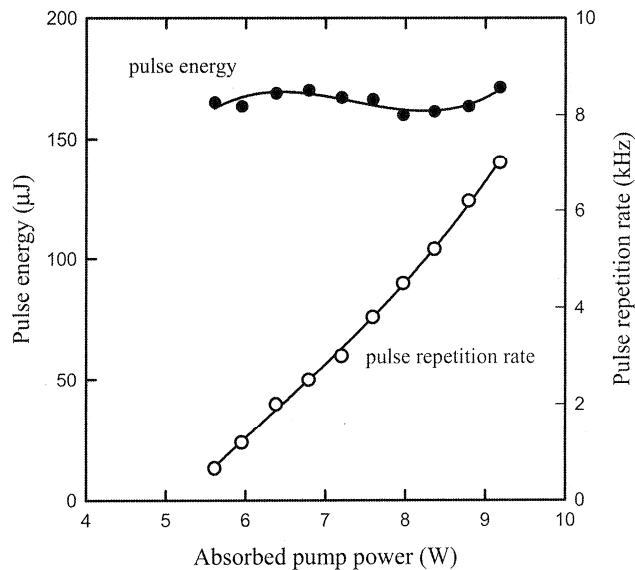


Fig. 4. Experimental results for pulse repetition rate and pulse energy versus absorbed pump power.

with the following coupled rate equations:

$$\frac{d\phi}{dt} = \frac{\phi}{t_r} [2\sigma n l - 2\sigma_s n_s l_s - \ln(1/R_c) - L], \quad (1)$$

$$\frac{dn}{dt} = r_p - \gamma c \sigma \phi n - \frac{n}{t_f}, \quad (2)$$

$$\frac{dn_s}{dt} = -\frac{A}{A_s} c \sigma_s \phi n_s + \frac{(n_{s0} - n_s)}{t_s}, \quad (3)$$

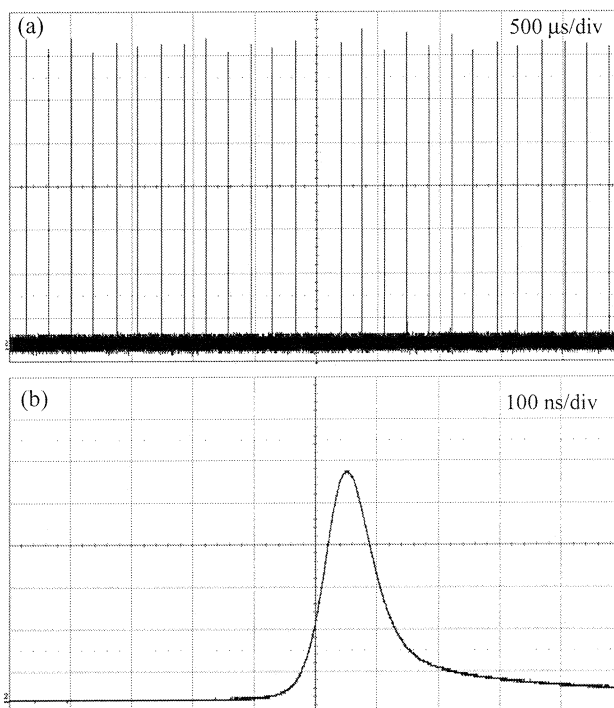


Fig. 5. (a) Typical oscilloscope trace of a train of output pulses and (b) expanded shape of a single pulse.

where ϕ is the intracavity photon density with respect to the effective cross-sectional area of the laser beam in the gain medium, n is the population density of the gain medium, n_s is the ground-state population density of the saturable absorber, n_{s0} is the initial ground-state population density in the saturable absorber, σ is the stimulated emission cross section of the gain medium, σ_s is the absorption cross section in the saturable absorber, l is the length of the gain medium, l_s is the length of the saturable absorber, A/A_s is the ratio of the effective beam area in the gain medium to the beam area in the saturable absorber, γ is the inversion reduction factor, r_p is the rate of the

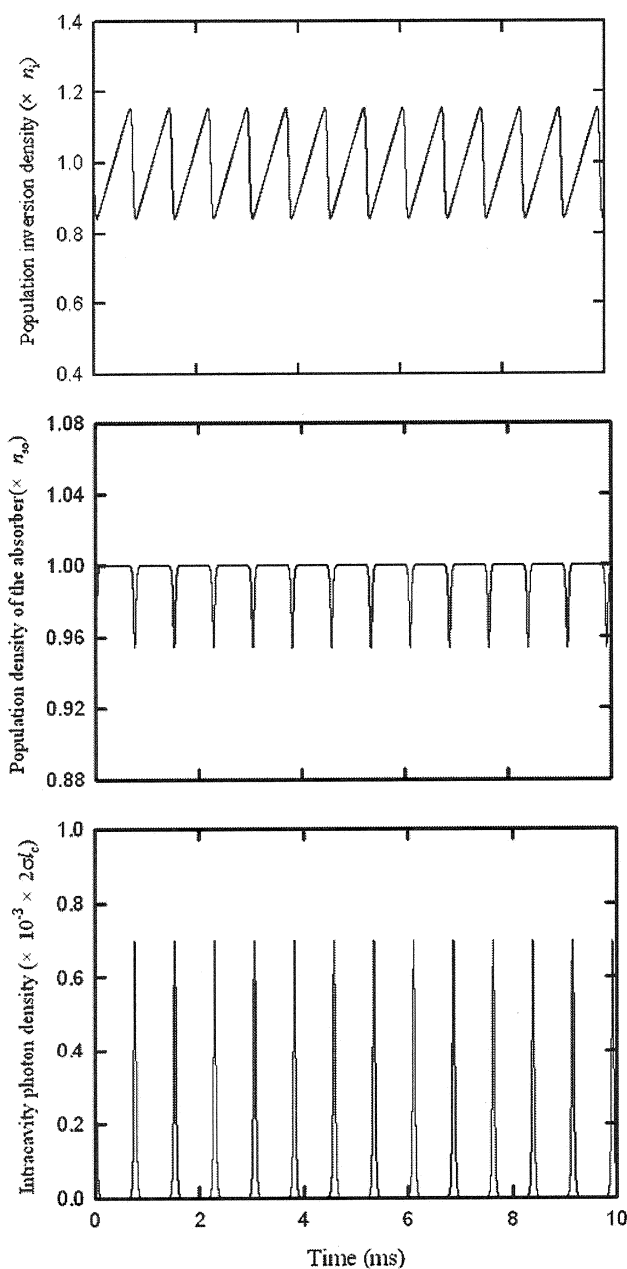


Fig. 6. Numerical results for the population density of the gain medium, the ground-state population density of the saturable absorber, and the intracavity photon density. The results correspond to the absorbed pump power of 6 W.

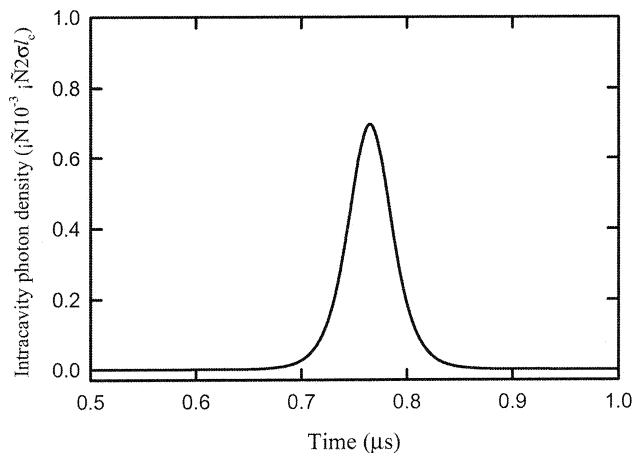


Fig. 7. Numerical result for the single Q-switched pulse shape.

pump density, t_r is the round-trip transit time of light in the cavity, c is the speed of light, t_f is the lifetime of the upper-level state of the gain medium, t_s is the lifetime of the excited state of the saturable absorber, R_c is the reflectivity of the output mirror, and L is the nonsaturable intracavity round-trip dissipative optical loss.

The values of the parameters used in the calculation are as follows: $\sigma = 3.3 \times 10^{-21} \text{ cm}^2$ (Ref. 5), $t_f = 2.28 \text{ ms}$,⁵ $\sigma_s = 4.6 \times 10^{-19} \text{ cm}^2$, $t_s = 0.1 \text{ ns}$, $T_o = 0.985$, $R_c = 0.975$, $L = 0.03$, $t_r = 0.2 \text{ ns}$, $l = 0.4 \text{ cm}$, $r_p = 7000 \text{ cm}^{-3}/\text{s}$, and $\gamma = 2$. Figure 6 depicts the numerical results for the population density of the gain medium, the ground-state population density of the saturable absorber, and the intracavity photon density. The condition of the numerical analysis corresponds to the absorbed pump power of 6 W. It can be seen that the repetition rate agrees very well with the experimental results. Furthermore as shown in Fig. 7, the theoretical pulse shape is in good agreement with the experimental data. With the numerical integration, the theoretical output pulse energy is found to 170 μJ , which is also close to the experimental result. The general agreement indicates that the simple model of the coupled rate equations is adequate for a first-order prediction of the low-gain laser characteristics.

5. Conclusions

A diode-pumped Yb:YCOB laser operating at 1086 nm was passively Q switched by using InGaAs QWs as semiconductor saturable-absorber output couplers. An average output power of 1.15 W with a Q-switching efficiency of 41% was obtained at an absorbed pump power of 9.2 W. Stable Q-switched pulses of 100 ns duration with a repetition rate of 7 kHz were generated. The present result indicates the possibility of using the InGaAs QW structure to mode lock a Yb:YCOB laser at 1086 nm.

The laser experiments of this work were supported by the MOE-ATU project and the National Science Council of Taiwan (contract NSC-95-2112-M-009-041-MY2). This work was also supported by a grant from

F6

F7

AQ: D

rich2/zod-osa/zod-osa/zod01207/zod3927-07z	xppws	S=1	1/25/07	Art: LP-75785
--	-------	-----	---------	---------------

the State Key Programs of China (2004CB619002) and the National Natural Science Foundation of China (grants 50672050, 50590401).

References

1. T. Taira, J. Saikawa, T. Kobayashi, and R. L. Byer, "Diode-pumped tunable Yb:YAG miniature lasers at room temperature: modeling and experiment," *IEEE J. Sel. Top. Quantum Electron.* **3**, 100–104 (1997).
2. D. A. Hammons, J. M. Eichenholz, Q. Ye, B. H. T. Chai, L. Shah, R. E. Peale, M. Richardson, and H. Qiu, "Laser action in Yb³⁺:YCOB (Yb³⁺:YCa₄O(BO₃)₃)," *Opt. Commun.* **156**, 327–330 (1998).
3. H. Zhang, X. Meng, P. Wang, L. Zhu, X. Liu, R. Cheng, J. Dawes, P. Dekker, S. Zhang, and L. Sun, "Slope efficiency of up to 73% for Yb:Ca₄YO(BO₃)₃ crystal laser pumped by a laser diode," *Appl. Phys. B* **68**, 1147–1149 (1999).
4. F. Augé, F. Balembois, P. Georges, A. Brun, F. Mougel, G. Aka, A. Kahn-Harari, and D. Vivien, "Efficient and tunable continuous-wave diode-pumped Yb³⁺:Ca₄GdO(BO₃)₃ laser," *Appl. Opt.* **38**, 976–979 (1999).
5. S. Chénais, F. Druon, F. Balembois, G. Lucas-Leclin, P. Georges, A. Brun, M. Zavelani-Rossi, F. Augé, J. P. Chambaret, G. Aka, and D. Vivien, "Multiwatt, tunable, diode-pumped CW Yb:GdCOB laser," *Appl. Phys. B* **72**, 389–393 (2001).
6. A. Lucca, M. Jacquemet, F. Druon, F. Balembois, P. Georges, P. Camy, J. L. Doualan, and R. Moncorgé, "High-power tunable diode-pumped Yb³⁺:CaF₂ laser," *Opt. Lett.* **29**, 1879–1881 (2004).
7. M. Jacquemet, C. Jacquemet, N. Janel, F. Druon, F. Balembois, P. Georges, J. Petit, B. Viana, D. Vivien, and B. Ferrand, "Efficient laser action of Yb:LSO and Yb:YSO oxyorthosilicates crystals under high-power diode-pumping," *Appl. Phys. B* **80**, 171–176 (2005).
8. V. E. Kisel, A. E. Troshin, N. A. Tolstik, V. G. Shcherbitsky, N. V. Kuleshov, V. N. Matrosov, T. A. Matrosova, and M. I. Kupchenko, "Spectroscopy and continuous-wave diode-pumped laser action of Yb³⁺:YVO₄," *Opt. Lett.* **29**, 2491–2493 (2004).
9. J. Liu, X. Mateos, H. Zhang, J. Wang, M. Jiang, U. Griebner, and V. Petrov, "Continuous-wave laser operation of Yb:LuVO₄," *Opt. Lett.* **30**, 3162–3164 (2005).
10. J. Liu, X. Mateos, H. Zhang, J. Wang, M. Jiang, U. Griebner, and V. Petrov, "Characteristics of a continuous-wave Yb:GdVO₄ laser end pumped by a high-power diode," *Opt. Lett.* **31**, 2580–2582 (2006).
11. J. Dong, P. Deng, Y. Liu, Y. Zhang, J. Xu, W. Chen, and X. Xie, "Passively Q-switched Yb:YAG laser with Cr⁴⁺:YAG as the saturable absorber," *Appl. Opt.* **40**, 4303–4307 (2001).
12. J. I. Mackenzie and D. P. Shepherd, "End-pump, passively Q-switched Yb:YAG double-clad waveguide laser," *Opt. Lett.* **27**, 2161–2163 (2002).
13. H. Wu, P. Yan, M. Gong, and Q. Liu, "A passively Q-switched diode-pumped Yb:YAG microchip laser," *Chin. Opt. Lett.* **1**, 697–698 (2003).
14. V. E. Kisel, A. E. Troshin, N. A. Tolstik, V. G. Shcherbitsky, N. V. Kuleshov, V. N. Matrosov, T. A. Matrosova, and M. I. Kupchenko, "Q-switched Yb³⁺:YVO₄ laser with Raman self-conversion," *Appl. Phys. B* **80**, 471–473 (2005).
15. X. Zhang, A. Brenier, Q. Wang, Z. Wang, J. Chang, P. Li, S. Zhang, S. Ding, and S. Li, "Passive Q-switching characteristics of Yb³⁺:Gd₃Ga₅O₁₂ crystal," *Opt. Express* **13**, 7708–7719 (2005).
16. Y. Kalisky, O. Kalisky, U. Rachum, G. Boulon, and A. Brenier, "Comparative performance of passively Q-switched diode-pumped Yb:GGG, Yb:YAG and Yb-doped tungstates lasers using Cr⁴⁺-doped garnets," in *Proc. SPIE* **6100**, 61001K (2006).
17. G. J. Spühler, R. Paschotta, M. P. Kullberg, M. Graf, M. Moser, E. Mix, G. Huber, C. Harder, and U. Keller, "A passively Q-switched Yb:YAG microchip laser," *Appl. Phys. B* **72**, 285–287 (2001).
18. G. J. Spühler, S. Reffert, M. Haiml, M. Moser, and U. Keller, "Output-coupling semiconductor saturable absorber mirror," *Appl. Phys. Lett.* **78**, 2733–2735 (2001).
19. J. J. Degnan, "Optimization of passively Q-switched lasers," *IEEE J. Quantum Electron.* **31**, 1890–1901 (1995).
20. X. Zhang, S. Zhao, Q. Wang, Q. Zhang, L. Sun, and S. Zhang, "Optimization of Cr⁴⁺-doped saturable-absorber Q-switched lasers," *IEEE J. Quantum Electron.* **33**, 2286–2294 (1997).

Compact efficient eye-safe intracavity optical parametric oscillator with a shared cavity configuration

Y. F. Chen, K. W. Su, Y. T. Chang, and W. C. Yen

We present a compact efficient eye-safe intracavity optical parametric oscillator pumped by a passively *Q*-switched Nd:YAG laser in a shared cavity configuration. A signal pulse of 3.3 mJ energy at a 1573 nm wavelength with a peak power of 150 kW was achieved. The effective conversion efficiency with respect to the optimized 1064 nm *Q*-switched pulse energy was as high as 51%. © 2007 Optical Society of America

OCIS codes: 140.3580, 140.5560.

1. Introduction

Compact nanosecond pulsed lasers operating with emission at the eye-safe wavelength region (1.5–1.6 μm) are of great interest for many applications such as laser radar, active imaging, and remote sensing.^{1,2} The methods for generating eye-safe lasers include the solid-state lasers with Er^{3+} -doped or Cr^{4+} -doped media^{3–6} and the Raman lasers pumped by Nd-doped lasers.^{7–10} Another promising approach for high-peak-power eye-safe laser sources is based on intracavity optical parametric oscillators (OPO).^{11–16} The advent of high damage threshold nonlinear crystals and diode-pumped Nd-doped lasers leads to a renaissance of interest in intracavity OPOs. Recently we demonstrated a compact efficient eye-safe OPO pumped by a diode-pumped passively *Q*-switched Nd:GVO₄ laser to produce peak powers at 1573 nm higher than 10 kW.¹⁷ However, the applications for long-distance laser rangefinders require pulse energies in the millijoule range and peak powers greater than 100 kW.²

The conventional configurations for intracavity OPO pumped by *Q*-switched Nd-doped lasers^{11–17} are based on the coupled cavity configuration in which there are separate resonators for the signal and fun-

damental optical fields. However, the amplitude stability of the signal outputs for the coupled cavity configuration is severely dependent on the cavity alignment because the resonator lengths and the longitudinal-mode spacing are different for the pump and signal beams. Recently it was confirmed¹⁸ that the shared cavity configuration in which the pump and signal beams share the same resonator provides a substantially superior amplitude stability in comparison with the coupled cavity configuration. Therefore it is of practical interest to develop the eye-safe intracavity OPO in the millijoule range with the shared cavity configuration.

In this work we use a shared resonator configuration to construct a compact intracavity OPO in the millijoule range. A lens duct is designed to be an efficient coupling lens for the diode-pumped passively *Q*-switched Nd:YAG/Cr⁴⁺:YAG laser. With the passively *Q*-switched laser to pump the intracavity OPO, 3.3 mJ pulses with 150 kW peak power at 1573 nm are generated. The effective conversion efficiency with respect to the optimized pulse energy form the passively *Q*-switched 1064 nm laser is up to 51%.

2. Experimental Setup of Intracavity Optical Parametric Oscillator

The pump source is a quasi-cw high-power diode stack (Coherent G-stack package, ■) that consists of six 10 mm long diode bars generating 80 W per bar, for a total of 480 W at the central wavelength of 808 nm. The diode stack is designed with 0.4 mm spacing between the diode bars so the overall area of emission is approximately 10 mm (slow axis) \times 2.4 mm (fast axis). The full divergence angles in the fast and slow axes are approximately 35° and 10°,

Y. F. Chen (yfchen@cc.nctu.edu.tw), K. W. Su, and Y. T. Chang are with the Department of Electrophysics, National Chiao Tung University, Hsinchu, Taiwan. W. C. Yen is with Chung-Shan Institute of Science and Technology, Lung-Tan, Tao-Yuan, Taiwan.

Received 12 October 2006; revised 3 December 2006; accepted 7 December 2006; posted 11 December 2006 (Doc. ID 76051); published 00 Month 2007.

0003-6935/07/120001-05\$15.00/0

© 2007 Optical Society of America

rich2/zod-osa/zod-osa/zod01207/zod3929-07z xppws S=1 1/25/07 Art: LP-76051

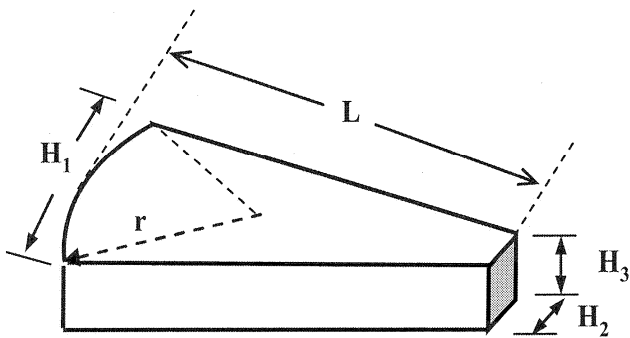


Fig. 1. Schematic of a lens duct in which r is the radius of the input surface, L is the length of the duct, H_1 is the width of the input surface, H_2 is the width of the output surface, and H_3 is the thickness of the duct.

respectively. A lens duct was designed to efficiently couple the pump radiation from the diode stack into the laser crystal. As shown in Fig. 1, there are five geometric parameters, r , L , H_1 , H_2 , and H_3 , for a lens duct, where r is the radius of the input surface, L is the length of the duct, H_1 is the width of the input surface, H_2 is the width of the output surface, and H_3 is the thickness of the duct.^{19,20} With the ray-tracing analysis,²⁰ the coupling efficiency was found to be up to 87% for a lens duct with the parameters of $r = 10$ mm, $L = 32$ mm, $H_1 = 12$ mm, $H_2 = 2.7$ mm, and $H_3 = 3$ mm. Based on the theoretical result, a lens duct was manufactured and used in the experiment.

Figure 2(a) shows the experimental setup of the intracavity OPO pumped by a diode-pumped pas-

sively Q -switched Nd:YAG/Cr⁴⁺:YAG laser in a shared cavity configuration. The fundamental laser cavity was formed by a coated Nd:YAG crystal and an output coupler. The OPO cavity entirely overlapped with the fundamental laser cavity. The Nd:YAG crystal had a 1.0 at. % Nd³⁺ doping concentration, a diameter of 5 mm, and a length of 10 mm. To set up the shared cavity, the incident side of the laser crystal was coated to be highly reflective at 1064 and 1573 nm ($R > 99.8\%$) and highly transmitted at the pump wavelength of 808 nm ($T > 90\%$). The other side of the laser crystal was coated to be antireflective at 1064 and 1573 nm ($R < 0.2\%$). A KTP crystal was used to be the nonlinear crystal of the OPO. The KTP crystal, 4 mm × 4 mm × 20 mm, was employed in a type II noncritical phase-matching configuration along the x axis ($\theta = 90^\circ$, and $\phi = 0^\circ$) to have both a maximum effective nonlinear coefficient and no walk off between the pump, signal, and idler beams. On the other hand, a Cr⁴⁺:YAG crystal was used to serve as a saturable absorber for passive Q -switching. The Cr⁴⁺:YAG crystal had a thickness of 3 mm with 60% initial transmission at 1064 nm. Both sides of the KTP and Cr⁴⁺:YAG crystals were coated for antireflection at 1573 and 1064 nm. The output coupler had a dichroic coating that was highly reflective at 1064 nm ($R > 99.8\%$) and partially reflective at 1573 nm ($R = 60\%$). All crystals were wrapped with indium foil and mounted in conductively cooled copper blocks. The total cavity length was approximately 50 mm.

For comparison, the conventional coupled cavity configuration is depicted in Fig. 2(b). It can be seen that the OPO cavity in the coupled resonator confi-

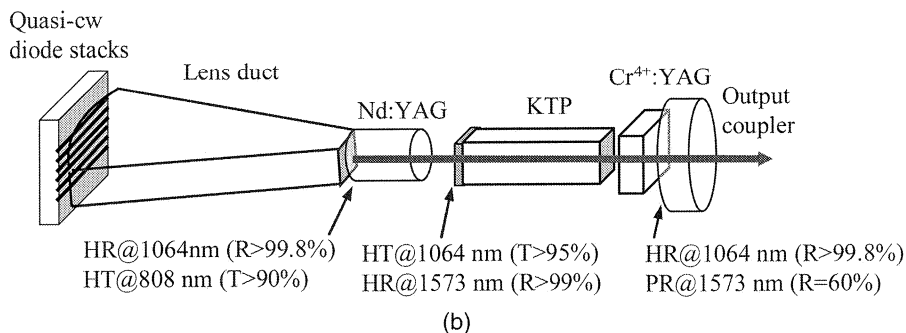
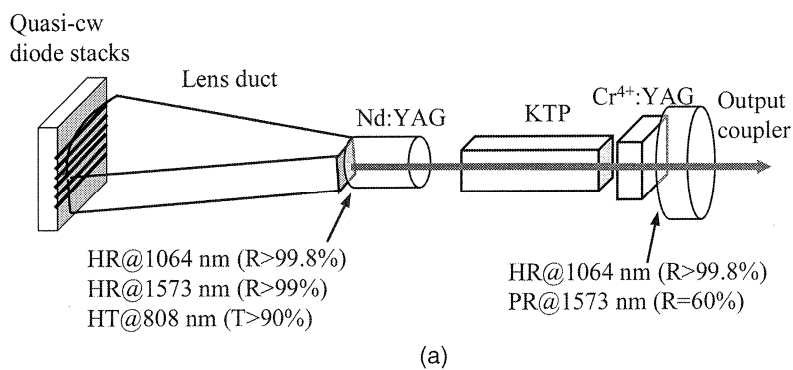


Fig. 2. Schematic of the intracavity OPO pumped by a diode-pumped passively Q -switched Nd:YAG/Cr⁴⁺:YAG laser. (a) Shared cavity, (b) coupled cavity.

rich2/zod-osa/zod-osa/zod01207/zod3929-07z xppws S=1 1/25/07 Art: LP-76051

uration was formed by a coated KTP crystal and an output coupler and the OPO cavity length was approximately 25 mm. One side of the KTP crystal was coated to have high reflection at the signal wavelength of 1573 nm ($R > 99.8\%$) and high transmission at the pump wavelength of 10643 nm ($T > 95\%$). The other side of the KTP crystal was coated for antireflection at 1573 and 1063 nm.

The pulse temporal behavior at 1063 and 1571 nm was recorded by a LeCroy digital oscilloscope (Wavepro 7100; 10 G samples/s, 1 GHz bandwidth) with a fast InGaAs photodiode. The spectral information of the laser was monitored by an optical spectrum analyzer (Advantest Q8381A, ■). The spectrum analyzer employing diffraction grating monochromator can be used for high-speed measurement of pulse light with the resolution of 0.1 nm.

AQ: B

3. Experimental Results

First, the quasi-cw free-running operation without KTP and Cr^{4+} :YAG crystals was performed to confirm the pumping efficiency of the lens duct and the quality of the laser crystal. For this investigation the diode stack was derived to emit optical pulses 200 μs long, at a repetition rate of 100 Hz with a maximum duty cycle of 2%. Furthermore an output coupler with 96% reflectivity at 1064 nm was used instead of the above-mentioned OPO output coupler. Figure 3 plots the experimental results of the free-running operation for the output average power as a function of the diode pump power. It can be seen that the output power of 160 W was achieved at an incident pump power of 360 W. The overall slope efficiency was found to be as high as 45%. The fairly good efficiency affirms the pump scheme to be practical.

F3

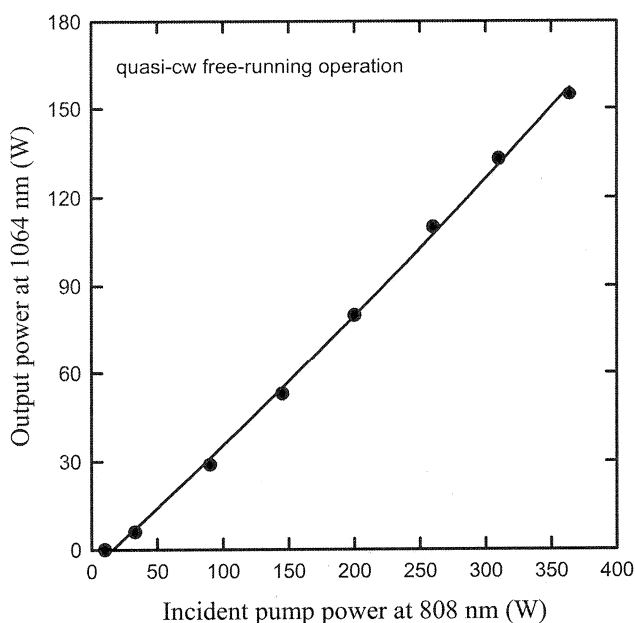


Fig. 3. Output power at 1064 nm with respect to the incident pump power at 808 nm for quasi-cw free-running operation.

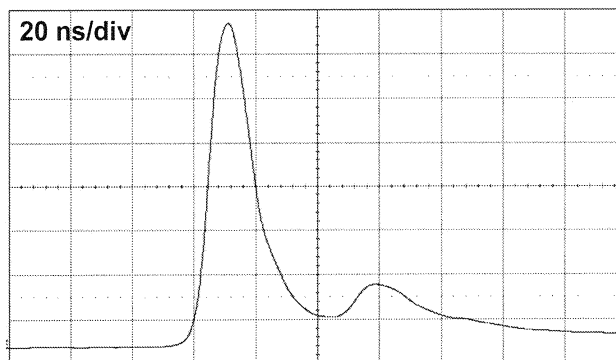


Fig. 4. Temporal shape for the passively Q -switched Nd:YAG/ Cr^{4+} :YAG laser at 1064 nm.

We estimated the performance of the passively Q -switched Nd:YAG/ Cr^{4+} :YAG laser before the intracavity OPO experiment. For this investigation an output coupler with partial reflection at 1064 nm was used, and the diode stack was derived to emit optical pulses 250 μs long at a repetition rate of 10 Hz. The optimum Q -switched performance at 1064 nm provides the baseline for evaluating the conversion efficiency of the intracavity OPO. The optimum reflectivity of the output coupler was found to be approximately 60%. The threshold of the Q -switched laser operation was found to be approximately 102 mJ, and the output pulse energy at 1064 nm was measured to be 6.5 mJ. As shown in Fig. 4, the effective pulse width was found to be approximately 19 ns; consequently, the peak power was up to 330 kW.

F4

With an OPO output coupler, the intracavity OPO experiment was performed. The threshold of the intracavity OPO was found to be nearly the same as that of the passively Q -switched laser. The output pulse energy of the signal wave at 1573 nm was measured to be 3.3 mJ. The effective conversion efficiency with respect to the optimized pulse energy from the passively Q -switched laser is up to 51%. For the coupled cavity,¹² the conversion efficiency was found to be approximately 26%. In other words, the conversion

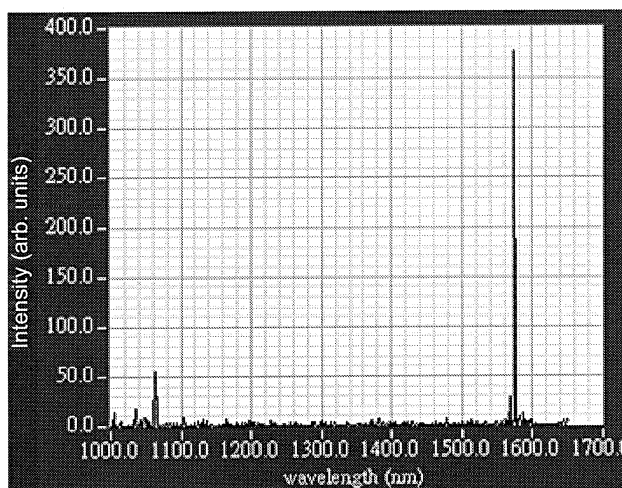


Fig. 5. Optical spectrum measurement for the intracavity OPO.

rich2/zod-osa/zod-osa/zod01207/zod3929-07z xppws S=1 1/25/07 Art: LP-76051

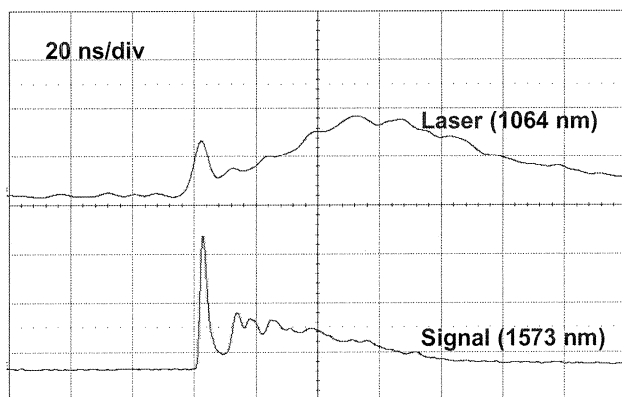


Fig. 6. Typical temporal shapes for the laser and signal pulses.

efficiency of the shared cavity configuration is significantly superior to that of the coupled cavity configuration. The OPO performance of the shared cavity basically depends on the total laser power of all longitudinal modes not on the explicit distribution of the laser power among the longitudinal modes. The small perturbations in the stable resonators usually lead to considerable variations in the power distribution among the longitudinal modes and do not significantly affect the total laser power. On the other hand, in the coupled cavity configuration the OPO and laser resonators have different longitudinal mode spacings;

mostly only one longitudinal laser mode is utilized to pump the OPO, and only one signal longitudinal mode builds up. Therefore the overall conversion efficiency of the shared cavity configuration is substantially superior to that of the coupled cavity configuration.

The typical result for the optical spectrum measurement is depicted in Fig. 5. Figure 6 shows the temporal shapes of the laser and signal pulses. It can be seen that the signal output consisted of a short intensive leading peak accompanied by a long weak ripple. The long weak ripple may come from the interaction between different longitudinal modes; thus far, the mechanism of its appearance is still unknown and needs further investigation. With the numerical integration, the signal peak power was calculated and found to be approximately 150 kW. The signal peak power is expected to be enhanced by the use of an output coupler with a lower reflectivity at the signal wavelength. The spatial distribution of the signal output was recorded with an infrared CCD and displayed in Fig. 7. The beam quality M^2 factor was estimated to be approximately 1.5.

F5-6

F7

4. Conclusions

We have employed a diode-pumped passively Q-switched Nd:YAG laser to pump an intracavity OPO in a shared cavity configuration. A lens duct has been designed to efficiently couple the pump radiation from the diode stack into the laser crystal. A slope efficiency of 45% has been obtained for the quasi-cw free-running operation in the fundamental mode lasing. For the Q-switching operation at 1064 nm, the cavity produced 6.5 mJ pulses with 330 kW peak power. With the Q-switched laser to pump the OPO at 1573 nm, 3.3 mJ pulses with 150 kW peak power have been achieved, corresponding to an effective conversion efficiency of 51% with respect to the optimized pulse energy at 1064 nm.

References

1. E. Gregor, D. E. Nieuwsma, and R. D. Stultz, "20 Hz eye-safe laser rangefinder for air defense," in Proc. SPIE **1207**, 124–134 (1990).
2. J. E. Nettleton, B. W. Schilling, D. N. Barr, and J. S. Lei, "Monoblock laser for a low-cost, eyesafe, microlaser range finder," Appl. Opt. **39**, 2428–2432 (2000).
3. S. Kück, K. Petermann, U. Pohlmann, U. Schönhoff, and G. Huber, "Tunable room-temperature laser action of Cr^{4+} -doped $\text{Y}_3\text{Sc}_x\text{Al}_{5-x}\text{O}_{12}$," Appl. Phys. B **58**, 153–156 (1994).
4. N. V. Kuleshov, A. A. Lagatsky, A. V. Podlipensky, V. P. Mikhailov, A. A. Kornienko, E. B. Dunina, S. Hartung, and G. Huber, "Fluorescence dynamics, excited-state absorption and stimulated emission of Er^{3+} in $\text{KY}(\text{WO}_4)_2$," J. Opt. Soc. Am. B **15**, 1205–1212 (1998).
5. I. Sokólska, E. Heumann S. Kück, and T. Łukasiewicz, "Laser oscillation of $\text{Er}^{3+}:\text{YVO}_4$ and $\text{Er}^{3+}, \text{Yb}^{3+}:\text{YVO}_4$ crystals in the spectral range around 1.6 μm ," Appl. Phys. B **71**, 893–896 (2000).
6. A. Sennaroglu, "Broadly tunable Cr^{4+} -doped solid-state lasers in the near infrared and visible," Prog. Quantum Electron. **26**, 287–352 (2002).
7. P. Černý, H. Jelínková, P. Zverev, and T. T. Basiev, "Solid-state lasers with Raman frequency conversion," Prog. Quantum Electron. **28**, 113–143 (2004).

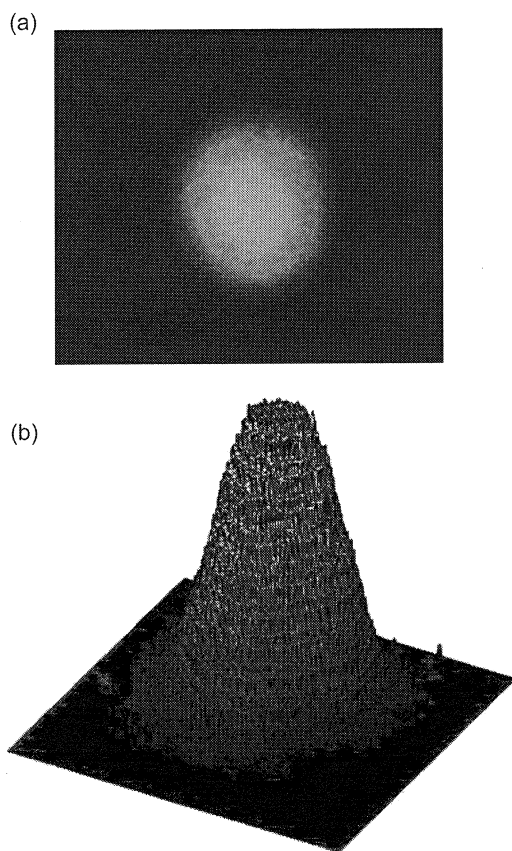


Fig. 7. Experimental far-field pattern of the signal output pulse. (a) 2D image, (b) 3D representation.

rich2/zod-osa/zod-osa/zod01207/zod3929-07z	xppws	S=1	1/25/07	Art: LP-76051
--	-------	-----	---------	---------------

8. Y. F. Chen, "Compact efficient all-solid-state eye-safe laser with self-frequency Raman conversion in a Nd:YVO₄ crystal," *Opt. Lett.* **29**, 2172–2174 (2004).
9. Y. F. Chen, "Efficient 1521 nm Nd:GdVO₄ Raman laser," *Opt. Lett.* **29**, 2632–2634 (2004).
10. J. T. Murray, R. C. Powell, D. Smith, W. Austin, and R. A. Stolzenberger, "Generation of 1.5 μ m radiation through intracavity solid-state Raman shifting in Ba(NO₃)₂ nonlinear crystals," *Opt. Lett.* **20**, 1017–1019 (1995).
11. Y. Yashkir and H. M. van Driel, "Passively Q-switched 1.57 μ m intracavity optical parametric oscillator," *Appl. Opt.* **38**, 2554–2559 (1999).
12. A. Agnesi, S. Dell'Acqua, and G. Reali, "Diode-pumped quasi-cw intracavity optical parametric oscillator at 1.57 μ m with efficient pulse shortening," *Appl. Phys. B* **70**, 751–753 (2000).
13. R. Dabu, C. Fenic, and A. Stratan, "Intracavity pumped nanosecond optical parametric oscillator emitting in the eye-safe range," *Appl. Opt.* **40**, 4334–4340 (2001).
14. W. Zendzian, J. K. Jabczyński, and J. Kwiatkowski, "Intracavity optical parametric oscillator at 1572 nm wavelength pumped by passively Q-switched diode-pumped Nd:YAG laser," *Appl. Phys. B* **76**, 355–358 (2003).
15. Y. F. Chen, S. W. Chen, Y. C. Chen, Y. P. Lan, and S. W. Tsai, "Compact efficient intracavity optical parametric oscillator with a passively Q-switched Nd:YVO₄/Cr⁴⁺:YAG laser in a hemispherical cavity," *Appl. Phys. B* **77**, 493–495 (2003).
16. B. W. Schilling, S. R. Chinn, A. D. Hays, L. Goldberg, and C. W. Trussell, "End-pumped 1.5 μ m monoblock laser for broad temperature operation," *Appl. Opt.* **45**, 6607–6615 (2006).
17. Y. F. Chen, S. W. Chen, L. Y. Tsai, Y. C. Chen, and C. H. Chien, "Efficient subnanosecond intracavity optical parametric oscillator pumped with a passively Q-switched Nd:GdVO₄ laser," *Appl. Phys. B* **79**, 823–825 (2004).
18. Y. F. Chen and L. Y. Tsai, "Comparison between shared and coupled resonators for passively Q-switched Nd:GdVO₄ intracavity optical parametric oscillators," *Appl. Phys. B* **82**, 403–406 (2006).
19. R. J. Beach, "Theory and optimization of lens ducts," *Appl. Opt.* **35**, 2005–2015 (1996).
20. R. Fu, G. Wang, Z. Wang, E. Ba, G. Mu, and X. Hu, "Design of efficient lens ducts," *Appl. Opt.* **37**, 4000–4003 (1998).

